FEDERAL UNIVERSITY OF SÃO CARLOS
CENTER OF EXACT SCIENCE AND TECHNOLOGY
GRADUATE PROGRAM IN MATERIALS SCIENCE AND ENGINEERING

MECHANICAL PROPERTIES AND METALLURGICAL CHARACTERIZATION OF AA6082-T6 ALLOY WELDED BY REFILL FRICTION STIR SPOT WELDING

Bruno Hessel Silva

São Carlos

2019

FEDERAL UNIVERSITY OF SÃO CARLOS
CENTER OF EXACT SCIENCE AND TECHNOLOGY
GRADUATE PROGRAM IN MATERIALS SCIENCE AND ENGINEERING

MECHANICAL PROPERTIES AND METALLURGICAL CHARACTERIZATION OF AA6082-T6 ALLOY WELDED BY REFILL FRICTION STIR SPOT WELDING

Bruno Hessel Silva

Dissertation presented to the Graduate Program in Materials Science and Engineering to obtention of the MASTER DEGREE IN MATERIALS SCIENCE AND ENGINEERING.

Supervisor: Prof. Dr. Claudemiro Bolfarini

Co-supervisor: Prof. Dr. Guilherme Zepon

Funding agency: CNPq – Process number: 139293/2018-3

São Carlos

2019

DEDICATION

To my parents, José and Rosana, my brother Felipe, my sister Francine and my fiancée Nicole, with love and tenderness.

CANDIDATE VITAE

Materials Engineering degree at Federal University of São Carlos (2018).

UNIVERSIDADE FEDERAL DE SÃO CARLOS

Centro de Ciências Exatas e de Tecnologia
Programa de Pós-Graduação em Ciência e Engenharia de Materiais

Folha de Aprovação

Assinaturas dos membros da comissão examinadora que avaliou e aprovou a Defesa de Dissertação de Mestrado do candidato Bruno Hessel Silva, realizada em 30/07/2019:

Prof. Dr. Claudemiro Bolfarini
UFSCar

Prof. Dr. Piter Gargarella
UFSCar

Prof. Dr. Marcelo Falcão de Oliveira
USP

ACKNOWLEDGEMENTS

I thank God for my life, health, and all the blessings that have occurred until this day in my family.

I thank my family for the principles taught, the financial support, the emotional support and all the education provided during my life.

My fiancée Nicole Teodoro who with her attention, patience, love and affection gave me all the emotional support needed to complete this stage of my life.

To the Professors Claudemiro Bolfarini and Guilherme Zepon for the many opportunities offered, for the discussions, corrections, suggestions, collaborations that have optimized this work and for the countless contributions and advice that allowed me to develop my academic career.

To my supervisors at HZG, Jorge dos Santos and Uceu Suhuddin for the opportunity to work with this welding technique and for all the contributions made to this research during the time the project was carried out in Germany.

To my colleagues from PPGCEM and HZG who have helped me in several situations regarding academic and personal matters.

To DEMa, PPGCEM and HZG for the excellent infrastructure and technical members that collaborated to the experiments related to this dissertation.

To the Conselho Nacional de Desenvolvimento Científico e Tecnológico-CNPq (Project number: 139293 / 2018-3). This study was financed in part by the Coordenação de Aperfeiçoamento de Pessoal de Nível Superior - Brasil (CAPES) - Finance Code 001.

RESUMO

PROPRIEDADES MECÂNICAS E CARACTERIZAÇÃO METALÚRGICA DA LIGA AA6082-T6 SOLDADA POR SOLDA A PONTO POR FRICÇÃO

Esforços para produção de automóveis com intenso uso de ligas de alumínio têm aumentado e ligas da série 6XXX são importantes neste cenário. Entretanto, técnicas de união aplicadas nessas ligas apresentam limitações na uniformidade das soldas, eficiência energética e custos de produção. A solda a ponto por fricção (RFSSW) é uma técnica de união no estado sólido com potencial para superar tais limitações. Para validar RFSSW em aplicações industriais é necessário avaliar fatores como propriedades mecânicas exigidas em norma; efeito dos parâmetros de processo nas características da solda; produtividade, custo e outros. Este trabalho apresenta um estudo da aplicação de RFSSW na liga AA6082-T6 para a indústria automotiva focando em: (i) efeito dos parâmetros de processo nas propriedades mecânicas e estrutura da solda; (ii) comportamento em fratura; (iii) influência do tratamento *Bake Hardening* nas propriedades mecânicas e características estruturais. Um conjunto de parâmetros com tempo de solda viável industrialmente foi obtido maximizando propriedades mecânicas usando análises estatísticas. Caracterizações macro/microestruturais demonstraram que o parâmetro de profundidade de penetração apresenta maior influência na resistência mecânica e no comportamento em fratura da solda devido influência na formação do defeito *hook*. Caracterizações térmicas e de dureza demonstraram o efeito do B*ake Hardening* na reprecipitação e superenvelhecimento nas regiões da solda e, consequentemente, nas propriedades mecânicas e comportamento em fratura. Através da estatística de Weibull, curvas de fadiga L-N demonstraram que independente do formato do *hook*, o comportamento em fadiga é similar (12% da máxima carga de cisalhamento). Caracterizações da superfície de fratura demonstraram que o formato do *hook* tem efeito relevante no modo de fratura apenas para condições de fadiga de baixo ciclo.

Palavras-chave: AA6082-T6; Solda a ponto por fricção; Bake Hardening; Propriedades mecânicas; Fadiga; Fratura.

ABSTRACT

The efforts to produce automobiles with intense use of aluminum alloys is growing and the 6XXX series of aluminum alloys are important for this scenario. However, the current joining technologies applied in these alloys present limitations regarding weld uniformity, energy input and production costs. Refill Friction Stir Spot Welding (RFSSW) is a solid-state welding technique with potential to surpass these limitations. In order to validate this technique in automotive applications, issues must be addressed such as obtaining mechanical properties standards; determining the effect of process parameters on weld structure and properties; optimizing cost-efficiency factors and others. In this work the application of RFSSW in the AA6082-T6 alloy was studied focusing on: (i) the effect of process parameters on weld structure and mechanical properties; (ii) understanding of fracture behavior of the welds under static and cyclic load; and (iii) the influence of Bake Hardening treatment on the weld structure and properties. Optimized process parameters set with suitable welding time for industry applications were obtained using statistical analysis maximizing static mechanical properties. Macro/microstructural analysis were carried out and demonstrated that the Plunge Depth parameter has the most relevant influence on weld strength and fracture behavior due to its effect in hook shape formation, which is an intrinsic feature in RFSSW welds. Hardness and thermal characterization helped to understand the effect of Bake Hardening on reprecipitation and overaging process in different weld regions and, consequently, on the mechanical properties and fracture behavior of the welds. Using Weibull Statistical analysis, L-N fatigue curves were obtained and demonstrated that, regardless the hook shape, the curves presented similar trend and fatigue limit close to 12% of the maximum Shear Load. Finally, based on fatigue fracture surface characterization, it was found that the hook shape configuration has a relevant effect on fracture behavior only for low-cycle load conditions.

Keywords: AA6082-T6; Refill Friction Stir Spot Welding; Bake Hardening; Mechanical properties; Fatigue; Fracture.

TABLE OF CONTENTS

Pag.

APPROVAL PAGE.....i
ACKNOWLEDGEMENTS iii
RESUMO.....v
ABSTRACT..... vii
TABLE OF CONTENTS.....ix
LIST OF TABLES..... xiii
LIST OF FIGURES xv
LIST OF SYMBOLS AND ABREVIATIONS xxi
1 INTRODUCTION.....1
2 OBJECTIVES.....5
3 LITERATURE REVIEW.....7
3.1 Refill Friction Stir Spot Welding (RFSSW).....7
3.2 Macro and microstructure of RFSSW welds.....10
3.3 Influence of RFSSW parameters on weld structure and strength 14
3.3.1 Heat input 14
3.3.2 Plunge Depth.....16
3.3.3 Rotational Speed 18
3.3.4 Feeding Rate/Welding time.....19
3.4 Aluminum alloys of 6XXX series and AA6082-T6 alloy.....20
3.5 Precipitation and coarsening in solid state welding techniques.....25
3.6 Bake hardening effect 29
3.7 Fatigue properties in RFSSW.....31
3.7.1 Fatigue Fracture behavior in RFSSW.....33
4 MATERIALS AND METHODS.....37

4.1 Materials 37
4.2 Welding machine and tool 37
4.3 Process Parameters Optimization 38
4.3.1 Preliminary Study 38
4.3.2 Design of Experiments 39
4.3.3 Statistical Analysis for Parameters Optimization 40
4.3.4 Optimized set confirmation and individual effect analysis 41
4.3.5 Mechanical tests 41
4.4 Influence of Process Parameters in Macro/Microstructure Features 42
4.4.1 Macro/Microstructure Characterization 42
4.4.2 Stop action procedure 43
4.5 Interrupted mechanical tests 44
4.6 Bake Hardening effect on RFSSW welds 44
4.6.1 Bake Hardening Treatment 45
4.6.2 Temperature measurements 45
4.6.3 Thermal analysis (DSC) 46
4.6.4 Hardness evaluation 46
4.6.5 Mechanical behavior 46
4.7 Fatigue properties evaluation 47
4.7.1 Fatigue tests 47
4.7.2 L-N curves determination and Weibull statistical analysis 47
4.7.3 Fracture surface analysis 49
5 RESULTS AND DISCUSSIONS 51
5.1 Process Parameters Optimization 51
5.1.1 Shear strength optimization 51
5.1.2 ANOVA from shear model 53

5.1.3 Peel Strength optimization 54
5.1.4 ANOVA from Peel model 56
5.1.5 One Factor at a Time (OFAT) 58
5.2 Influence of Process Parameters on Macro/Microstructure Features....62
5.2.1 Macro/Microstructure Characterization....62
5.2.2 Hook tip shape formation 65
5.3 Fracture analysis of static mechanical tests 68
5.3.1 Fracture modes....68
5.3.2 Failure Mode Transition 69
5.3.3 Interrupted mechanical tests 72
5.4 Bake Hardening effect on weld structure and properties 75
5.4.1 Temperature measurements....75
5.4.2 Thermal Analysis (DSC)....77
5.4.3 Hardness evaluation 79
5.4.4 Mechanical Behavior....80
5.5 Fatigue results 82
5.5.1 Fatigue properties evaluation and Weibull Statistical analysis....82
5.5.2 Fracture analysis....88
6 CONCLUSIONS 99
7 SUGGESTIONS FOR FUTURE WORKS 101
8 REFERENCES....103
SUPPLEMENTARY DATA....111

LIST OF TABLES

Pag.

Table 3.1 - Process Parameters and Shear Load results obtained by recent works of RFSSW in AA6082-T6 with 2 mm thickness sheet [6,29]. 10
Table 3.2 - Mechanical properties of AA6082 alloy in different heat treatment conditions [56].....25
Table 4.1 - Chemical composition of AA6082-T6 aluminum alloy in weight percentage (wt.%).....37
Table 4.2 - Preliminary study of weld surface defects from high and low heat input set of process parameters.....38
Table 4.3 - Experimental sets of process parameters using Box Behnken Design for mechanical tests evaluation. 40
Table 5.1 - Analysis of Variance (ANOVA) for shear model. 53
Table 5.2 - Box Behnken Design of experiment for Peel Strength optimization. 54
Table 5.3 - Analysis of Variance (ANOVA) for peel model. 57
Table 5.4 - Weibull parameters and Mean Time to Fracture from flat hook condition. 84
Table 5.5 - Weibull parameters and Mean Time to Fracture from hook pointing down condition.....84
Table 5.6 - Weibull parameters and Mean Time to Fracture from hook pointing up condition. 85

Table A – Shear optimization data from Box Behnken design experiments....111
Table B - Shear optimization data from complementary experiments expanding window of parameters values studied. 111
Table C - Peel optimization data from Box Behnken design experiments.....112
Table D - Shear data optimization from OFAT experiments. 113
Table E - Peel data optimization from OFAT experiments.....114
Table F - Fatigue data from flat hook condition. 114
Table G - Fatigue data from hook pointing down condition.....115
Table H - Fatigue data from hook pointing up condition. 115

LIST OF FIGURES

Pag.

Figure 3.1 - Illustration of the welding tool elements a) clamping ring b) sleeve c) pin and d) attachment configuration of the tool.....7
Figure 3.2 - RFSSW Variants showing welding stages; a) b) c) and d) stages from Sleeve Plunge variant; a) e) f) and d) stages from Pin Plunge variant.....8
Figure 3.3 - Materials combinations successfully welded by RFSSW. Sheet thickness of each combination is presented at the top of each graph bar (horizontal lines represent minimum shear strength required by AWS D17.2 for each sheet thickness) [6]. 9
Figure 3.4 - Maximum and average Shear Load results of riveting and FSSW techiniques for AA6082 2 mm aluminum sheets [28].....10
Figure 3.5 - Cross section macrostructure of AA6082-T6 weld produced by RFSSW indicating SZ, TMAZ, HAZ, hook defect, Bonding Ligament and Drop region.....11
Figure 3.6 - Microstructure of a) SZ b) TMAZ c) HAZ in an AA6082-T6 weld produced by RFSSW. 12
Figure 3.7 - Hardness profile in different regions of a AA2219-T851 RFSSW weld in different natural aging times [33]. 12
Figure 3.8 - a) Hook defect in a AA6061-T6 RFSSW weld b) Bonding Ligament in a AA2198 RFSSW weld [9,25]. 13
Figure 3.9 - Schematic illustration of Drop region formation during RFSSW [31]. 14
Figure 3.10 - Drop region in a RFSSW weld [17,31].....14
Figure 3.11 - Effect of energy input in mechanical performance of welds of Al5754 and AM60 produced by FSSW [39].....16
Figure 3.12 - Hook tip position in AA6061 RFSSW for different plunge depth values a) 1.9 mm b) 2.1 mm and c) 2.3 mm [9]. 17
Figure 3.13 - Linear relation between Tensile Shear Strength and Hook Height for AA6061 welds produced by RFSSW [9].....17

Figure 3.14 - Effect of Rotational Speed on Shear Strength of AA6022-T4/AA7075-T6 RFSSW weld for a) standard tool profile b) modified tool with grooves on the tip of the sleeve [40]. 19
Figure 3.15: Parameters influence in weld strength determined by statistical analysis from RFSSW welds of a) AA2198 b) AA2198-T8 c) AA2198-T8 [24,25,42]. 20
Figure 3.16 - 3D-atom probe analysis of size and shape from GP zones in a Al-0.65Mg-0.70Si sample after pre-ageing treatment of 70 ^{o}C for 16 hours [48]. . 22
Figure 3.17 - Precipitates size and morphology in AA6061 alloy solutioned and aged for a) 175 ^{o}C during 30 minutes b) 175 ^{o}C during 4 hours c) 175 ^{o}C during 72 hours d) 200 ^{o}C during 20 hours [51]. 23
Figure 3.18 - DSC curve of AA6082 disc samples with solution treatment, obtained by heating at 10 ^{o}C min^{-1} [45]. 24
Figure 3.19 - Schematic representation of temperature and strain distribution in the microstructural zones of a friction stir weld (FSW) [73]. 26
Figure 3.20 - Natural aging effect on microhardness of AA6005-T6 alloy welded by FSW [72]. 27
Figure 3.21 - Variations of precipitates during FSW a) volume fractions and b) geometrical sizes at 300 mm/min; c) volume fractions and d) geometrical sizes at 30 mm/min [68]. 28
Figure 3.22 - Stress-Strain curves from as received, Friction Stir Welded and Post Welded Heat Treated (PWHTed) AA6061 aluminum alloy [67]. 29
Figure 3.23 - Effect of natural aging on bake hardening response in a solid solutioned Al-Mg-Si-Cu alloy [7]. 30
Figure 3.24 - Effect of bake hardening treatment in microstructural changes of an Al-Mg-Si-Cu alloy; a) supersaturated solid solutioned condition b) bake hardened condition [7]. 31
Figure 3.25 - S-N curves with different failure probability levels obtained by Weibull statistical analysis for RFSSW welds of a) Al-Mg-Sc [17] b) AA5754/Ti6Al4V [81] c) AA7050-T76 [80] and d) AA2024-T3 [35]. 32
Figure 3.26 - Eyebrow fracture behavior observed in fatigue test samples of Al-Mg-Sc welded by RFSSW [17]. 33

Figure 3.27 - Sheet thickness fatigue crack propagation by the base material and between SZ/TMAZ interface [17].....33
Figure 3.28 - Fatigue fracture surfaces of specimens tested in low-cycle conditions for RFSSW welds of a) AA5754/Ti6Al4V [81] b) AA2024-T3 [35] c) AA7050-T76 [80] and d) ZEK 100 magnesium alloy [79].....35
Figure 4.1 - a) tools elements b) tool concentric attachment configuration. 38
Figure 4.2 - Points representing the experimental runs of a three factor Box Behnken Design [82].....39
Figure 4.3 - a) Lap Shear test configuration b) Coach Peel test configuration. 42
Figure 4.4 - Load versus Displacement curve demonstrating the interruption criteria for fracture analysis. 44
Figure 4.5 - Thermocouples approach applied in Lap Shear configuration to measure temperature profile in SZ and HAZ regions during welding process. .45
Figure 4.6 - Weld Cross section illustration indicating hardness lines position. 46
Figure 5.1 - Response surfaces and contour plots obtained by Box Behnken Design experiments changing process parameters a) PDxRS c) FRxPD e) FRxRS and g) contour plots. Response surfaces and contour plots obtained after complementary experiments b) PDxRS d) FRxPD f) FRxRS h) contour plots. .53
Figure 5.2 - Peel Strength Response surfaces and contour plots obtained by Box Behnken Design experiments changing process parameters a) PDxRS c) FRxPD e) FRxRS and g) contour plots.....56
Figure 5.3 - Shear strength OFAT results for a) Feeding Rate b) Plunge Depth c) Rotational Speed. 59
Figure 5.4 - Peel strength OFAT results for a) Feeding Rate b) Plunge Depth c) Rotational Speed. 60
Figure 5.5 - Macrostructure of the samples produced with PD=2.1mm, RS=2900rpm and feeding of a) FR=3.3mm/s b) FR=3.9mm/s and c) FR=4.5mm/s. 62
Figure 5.6 - Macrostructure of the samples produced with PD=2.1mm, FR=3.9mm/s and Rotational Speed of a) RS=2500rpm b) RS=2900rpm and c) RS=3100rpm. 63

Figure 5.7 - Macrostructure of the samples produced with FR=3.9mm/s, RS=2900rpm and Plunge Depth of a) PD=1.9mm b) PD=2.1mm and c) PD=2.3mm. 64
Figure 5.8 - Hook tip shapes of the welds produced with the same RS=2900 rpm, FR=3.9 mm/s and different Plunge Depth values. a) flat hook (PD=1.9mm), b) hook tip pointing down (PD=2.1mm) and c) hook tip pointing up (PD=2.3mm). 65
Figure 5.9 - Flat hook formation - Microstructures of hook tip region from stop action samples a) PD=1.9 mm during plunging stage, b) PD=1 mm during retracting stage, and c) final stage. 66
Figure 5.10 - Hook tip shape pointing down formation - Microstructures of hook tip region from stop action samples a) PD=2.1 mm during plunging stage, b) PD=1.1 mm during retracting stage and c) final stage. 66
Figure 5.11 - Hook tip shape pointing up formation - Microstructures of hook tip region from stop action samples a) PD=2.3 mm during plunging stage b) PD=1.6 mm during retracting stage c) final stage. 67
Figure 5.12 - Fracture modes observed during Static Mechanical tests. a) Through weld fracture (TW) b) Pull-Out fracture (PO). 68
Figure 5.13 - Force vs Displacement curve tests from samples with a) TW fracture b) PO fracture. 69
Figure 5.14 - Correlations between shear strength, fracture mode and processes parameters a) Feeding Rate b) Rotational Speed and c) Plunge Depth. 70
Figure 5.15 - Correlations between peel strength, fracture mode and processes parameters a) Feeding Rate b) Rotational Speed and c) Plunge Depth. 71
Figure 5.16 - Macrostructure of an interrupted shear test sample with flat hook tip shape produced using low value of Plunge Depth (PD:1.9mm). 72
Figure 5.17 - Microstructure of the crack tip region from interrupted shear test sample with flat hook tip shape produced with low value of Plunge Depth (PD:1.9mm). 72
Figure 5.18 - Macrostructure of an interrupted shear test sample with hook tip pointing up, produced using high value of Plunge Depth (PD:2.3mm). 73

Figure 5.19 - Microstructure of the crack region from interrupted shear test sample, with hook tip shape pointing up produced by high value of Plunge Depth (PD:2.3mm). 73
Figure 5.20 - Macrostructure of an interrupted shear test sample with hook tip pointing down produced using intermediate value of Plunge Depth (PD:2.1mm). 74
Figure 5.21 - Microstructures of the cracks regions from interrupted shear test sample with hook tip pointing down produced with intermediate value of Plunge Depth (PD:2.1mm). a) crack following TMAZ/HAZ region b) cracks foolowing hook tip region and base material. 74
Figure 5.22 - Temperature measurements in the SZ and HAZ regions during RFSSW welding. (process parameters applied - PD: 2.1 mm, FR: 3.9 mm/s and RS: 2700 rpm) 76
Figure 5.23 - DSC curves of BM, HAZ and SZ samples. 78
Figure 5.24 - Hardness maps produced for RFSSW welds of AA6082-T6 with and without bake hardening treatment. 79
Figure 5.25 - Bake Hardening effect on the shear strength for the three hook tip shape configuration (flat, pointing down and pointing up). 81
Figure 5.26 - Bake hardening effect in fracture mode on the three hook tip shape configurations (flat, pointing down and pointing up). 81
Figure 5.27 - Weibull plots of the data from a) flat hook condition b) hook pointing down condition and c) hook pointing up condition. 84
Figure 5.28 - L-N curves obtained by Weibull Statistical analysis for the three hook conditions. 86
Figure 5.29 - L-N curves with different reliability levels for a) flat hook condition b) hook pointing down condition and c) hook pointing up condition. 88
Figure 5.30 - Fracture modes identified during fatigue tests a) Through the Weld (TW) b) Pull-Out the nugget from both plates (PO1) c) Pull-Out the nugget from only one plate (PO2) d) Eyebrow fracture (EB). 89
Figure 5.31 - Failure mode transition in fatigue solicitation for the three hook conditions. 90

Figure 5.32 - Macrograph of the Eyebrow fatigue fracture surface indicating cracks nucleation site (red arrows) and crack propagation directions (blue arrows). 90
Figure 5.33 - Fatigue fracture characteristics and crack propagation in Eyebrow fracture indicating a) Multiple crack nucleation b) crack propagation in thickness direction (TMAZ/SZ interface) of the upper sheet c),d),e),f) presence of steps and fatigue striation along the transition from nugget region to base material g) and h) failure mechanism transition from fatigue striation to shear lips. (blue arrows indicate propagation direction) 92
Figure 5.34 - Fatigue fracture surface of flat hook specimen obtained in low-cycle load conditions. 93
Figure 5.35 - Fracture characteristics from flat hook specimen exhibiting a),b) cleavage c) dimples and d) cleavage. 93
Figure 5.36 - a) Fatigue fracture surface of hook pointing up specimen obtained in low-cycle load conditions b),c) and d) fracture characteristics indicating the presence of cleavage and dimples in the fractured surface. 94
Figure 5.37 - Fatigue fracture surface from hook pointing down condition tested in low-cycle load condition. 95
Figure 5.38 - Fracture characteristics from hook pointing down specimen exhibiting a),b) fatigue striation c) cleavage and d) dimples. 96

LIST OF SYMBOLS AND ABREVIATIONS

ANOVA	Analysis of Variance
AWS	American Welding Society
BBD	Box Behnken Design
BH	Bake Hardening
BIW	Body-in-white
BM	Base material
DSC	Differential Scanning Calorimetry
EB	Eyebrow fracture mode
FR	Feeding Rate
FSP	Friction Stir Processing
FSSW	Friction Stir Spot Welding
FSW	Friction Stir Welding
HAZ	Heat Affected Zone
HRTEM	High Resolution Transmission electron microscopy
HZG	Helmholtz Zentrum Geesthacht
NA	Natural Aging
OFAT	One Factor at a Time
PD	Plunge Depth
PFZ	Precipitate free zone
PO	Pull-Out the nugget fracture mode
PO1	Pull-Out the nugget from both plates fracture mode
PO2	Pull-Out the nugget from one plate fracture mode

PT	Plunge Time
RFSSW	Refill Friction Stir Spot Welding
RS	Rotational Speed
RSM	Response Surface Methodology
RSW	Resistance Spot Welding
SAED	Selected Area Electron Diffraction
SEM	Scanning Electron Microscope
STEM	Scanning Transmission electron microscopy
SPR	Self-Pierce Riveting
SZ	Stir Zone
t	welding time
TEM	Transmission electron microscopy
TMAZ	Thermal-Mechanically Affected Zone
TW	Through the Weld fracture mode
wt.%	weight percentage
σ_y	Yield Strength
σ_{max}	Tensile Strength

1 INTRODUCTION

The application of aluminum alloys in automotive industry has been increasing over the years in components as heat exchangers, wheels, bumpers, hoods and others. According to the Drucker worldwide Europe reports, the usage of aluminum per vehicles increased from 120 kg to 180 kg in the period 2005-2015. The same reports foresaw that in 2025 the usage of Al alloys may reach up to 225 kg per vehicle due to possible applications in doors and body-in-white (BIW) structure [1,2]. BIW applications offer the greatest scope for weight reduction using aluminum alloys. Examples of commercial vehicles with intense use of aluminum alloys can already be found, such as the Audi A8 and Ford AIV. However, the current production of such cars are limited due to the high manufacturing costs and the aluminum cost stability [1–4].

Regarding manufacturing costs, aluminum alloys present properties that make welding process non-uniform. For example, the high electrical conductivity, high thermal conductivity, low melting point, high hydrogen solubility in molten state and high thermal expansion coefficient make aluminum alloys difficulty to be welded by conventional fusion welding process. Defects as distortions, hot tears, cracks, porosity and others are difficult to avoid in fusion welding of Al alloys [1,3,5,6].

In the automobile produced with intense use of aluminum alloys, the key to replace ferrous alloys in BIW structure is on the precipitation strengthening and high formable aluminum alloys such as the 6XXX and 5XXX series, respectively [1–3,6–8]. The versatility of mechanical properties of 6XXX series alloys allows extensive industry application, including the automotive industry. This versatility is attributed to different precipitates evolution (distribution and size) reached by several heat treatment conditions. However, these alloys are very sensitive to thermal effects [2,3,6,7,9].

The two main current welding/joining techniques applied in aluminum alloys on automotive industry are the Resistance Spot Welding (RSW) and the Self-Pierce Riveting (SPR). Resistance Spot Welding is a fusion welding process that performs welds through the heat produced by the electrical resistance

between the interface of the joint materials from an electrical current generated by two electrodes. This technique has issues regarding the solidification defects mentioned before, present limitations in welding of precipitation strengthened aluminum alloys, due to the high heat-input applied, requires high energy input and demand frequent maintenance of the electrodes due to oxide formation. Self-Pierce Riveting is a mechanical joining technique and present none of the solidification problems mentioned before. However, it presents a high cost with consumables, that prevents the application in high production numbers [5,10,11].

As a consequence, technologies have been developed in order to solve these problems and fulfill this industry need. Refill Friction Stir Spot Welding (RFSSW) is a solid-state welding technique and a potential option to fill this gap. Differently from RSW and SPR, RFSSW does not need consumables or present solidification defects. Additionally, RFSSW is considered an environmental friendly solution since demands low levels of energy input during welding [5,6,12]. However, to establish a possible application of RFSSW in automotive industry, it is necessary to validate this welding technique by: i) obtaining standard mechanical properties for different alloys; ii) optimizing process parameters in order to minimize cost and maximize production efficiency; iii) evaluating the effect of post-welded treatments such as paint Bake Hardening treatments and others [5,7,13].

Some works of RFSSW technique in aluminum alloys have reported impressive mechanical performance, including for AA6082 alloy which is subject of this work [6,9,14]. Although good mechanical performance was reached in these works, welding times applied are not suitable to automotive applications [5].

In this context, this work provides information and discussion regarding RFSSW process parameters optimization and its effect on structural characteristics, mechanical properties and fracture behavior on welds of AA6082-T6 alloy. Moreover, the effect of a usual paint Bake Hardening treatment on the structure, mechanical properties and fracture behavior of these welds was evaluated. This work might contribute to the establishment of RFSSW in a future

application in automotive industry.

This research was a result of a scientific and technological partnership between the Federal University of São Carlos (UFSCar) and the German research center Helmholtz-Zentrum Geesthacht (HZG), which is a reference in RFSSW research.

2 OBJECTIVES

The main objectives of this work, regarding RFFSW of AA6082-T6, were:

- To obtain optimized processing parameters that maximize the static mechanical properties (shear and peel strength) using welding times suitable for automotive industry.
- To identify the correlation between the process parameters and macro/microstructural features of the welds.
- To identify the correlation between the process parameters and the fracture behavior of the welds in static mechanical solicitation.
- To analyze the effect of Bake Hardening on the structure and properties of optimized welds.
- To evaluate the fatigue properties and fracture behavior in cyclic load of optimized welds.

3 LITERATURE REVIEW

3.1 Refill Friction Stir Spot Welding (RFSSW)

RFSSW is a solid state welding technique developed by Jorge dos Santos in GKSS (Gesellschaft für Kernenergieverwertung in Schiffbau und Schiffahrt), currently HZG (Helmholtz Zentrum Geestacht) in Germany [15]. This process is able to perform welds without reaching the melting temperature of the base materials to be welded, thus preventing problems related to solidification process [16,17]. The welding principle of RFSSW is based on plasticizing and stirring materials by frictional heat and deformation produced between the material to be welded and the welding tool. The tool is composed of two rotating parts (a pin and a sleeve) and one no-rotating part (a clamping ring), as shown in Figure 3.1 (a), (b) and (c), respectively. The three elements of the tool are attached to each other coaxially as illustrated in Figure 3.1 (d) [15–17].

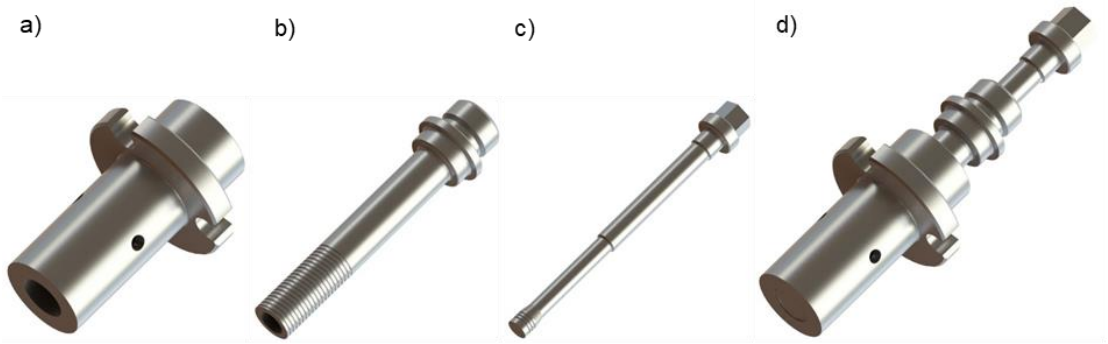

Figure 3.1 - Illustration of the welding tool elements a) clamping ring b) sleeve c) pin and d) attachment configuration of the tool.

To produce a weld, the tool performs four sequential steps as demonstrated in Figure 3.2. First the clamping ring holds tightly together the two aimed parts to be welded in order to avoid plasticized material to escape or rotate during the process. At the same time, the rotating pin and sleeve are placed on the surface of the material, generating frictional heat and deformation. Subsequently, base material is plasticized (Figure 3.2 (a)) allowing tool plunging. The second stage is the movement of the sleeve and the pin in opposite directions, providing two variants of this process (the sleeve plunge variant and

the pin plunge variant). In sleeve plunge variant, the pin retracts meanwhile the sleeve moves downward, therefore the softened material fill the cavity left by pin retraction (Figure 3.2 (b)). At the third stage, the tools elements reverse translational movement, which results in the refilling process, where the pin pushes back material to the hole left by sleeve retraction (Figure 3.2 (c)). In pin plunge variant, the pin moves downward while the sleeve retracts, consequently the cavity formed by sleeve retraction is filled by plasticized material (Figure 3.2 (e)) and, similarly to sleeve plunge variant, tools elements reverse translational movement at the third stage returning the plasticized material to the hole left by pin retraction (Figure 3.2 (f)). The last stage involves releasing of the welded materials by tool retraction, which is the same for both variants (Figure 3.2 (d)) [15–18].

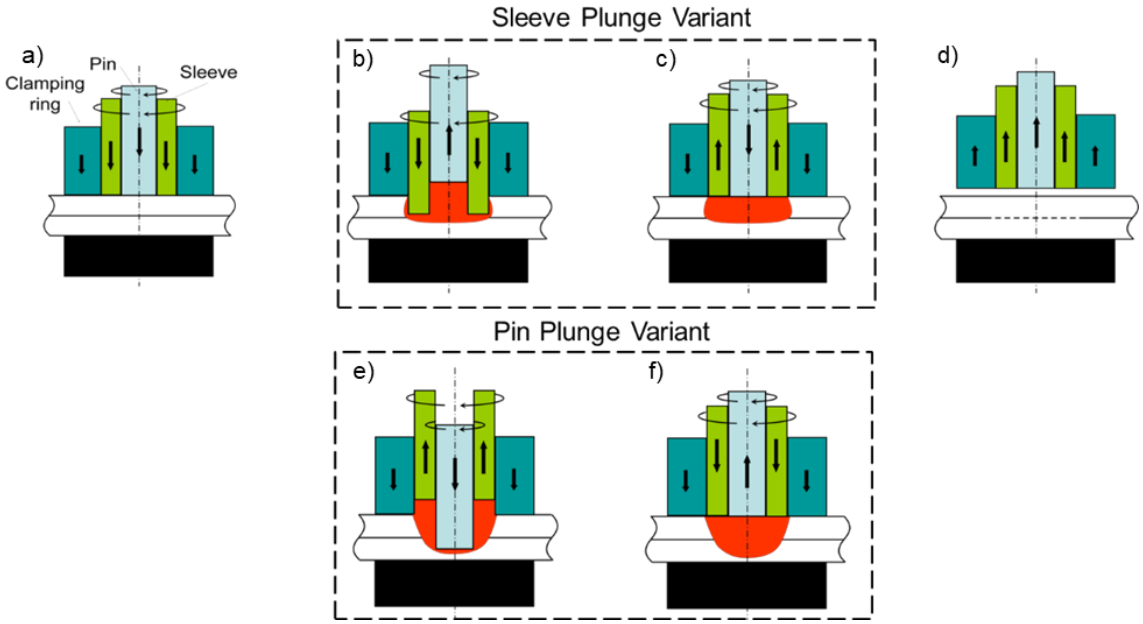

Figure 3.2 - RFSSW Variants showing welding stages; a) b) c) and d) stages from Sleeve Plunge variant; a) e) f) and d) stages from Pin Plunge variant.

Several works have applied Sleeve Plunge variant due to higher mechanical performance of the welds produced. This is often reported as a result from large bonded zone, which gives a higher effective shear area, thus improving mechanical behavior [19–21].

Some authors have reported impressive weld shear strength for similar aluminum and magnesium alloys produced with RFSSW (Figure 3.3) [6,9,16–18,22–26]. It is observed that similar combinations produced by RFSSW have fulfilled the minimum shear strength required by AWS D17.2 specification for Resistance Spot Welding for aerospace applications. In special AA6082, which is subject of this work, has presented twice the average load required for welds produced with 1 and 2 mm thickness [6,27].

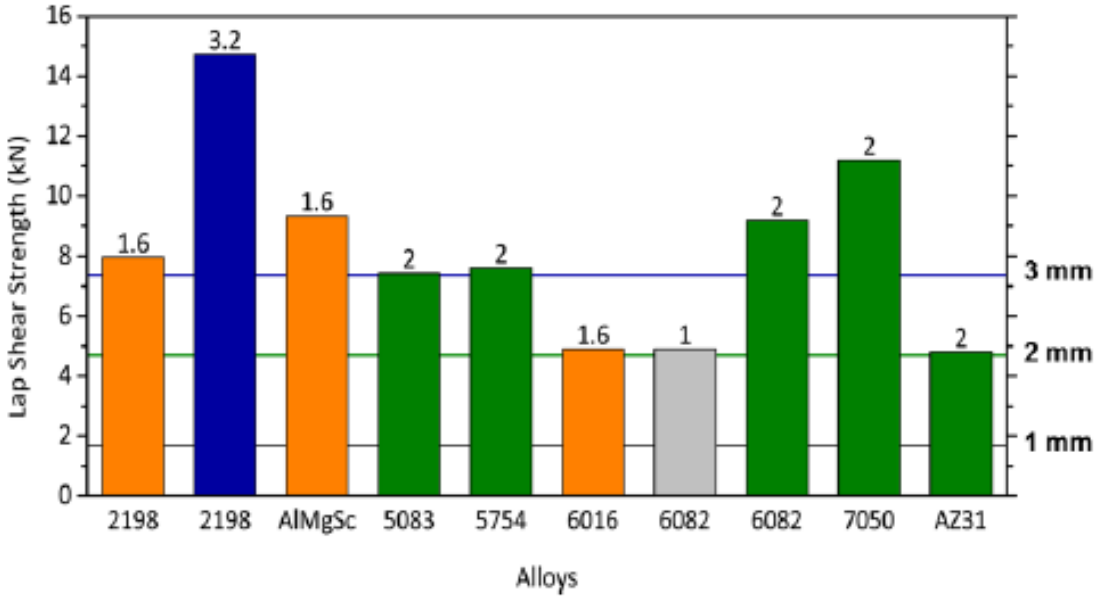

Figure 3.3 - Materials combinations successfully welded by RFSSW. Sheet thickness of each combination is presented at the top of each graph bar (horizontal lines represent minimum shear strength required by AWS D17.2 for each sheet thickness) [6].

As shown in Figure 3.3, previous works have evaluated weld mechanical performance of AA6082-T6 with 2 mm thickness sheet produced by RFSSW. Table 3.1 shows recent studies in shear strength of AA6082-T6 welds produced with different parameters process in 2 mm–thick sheets. Both authors obtained high levels of Shear Load (8.5 and 9 kN), considerably higher when compared to aerospace standard requirements (4.8 kN) [28]. These results are also higher than other techniques applied in automotive industry as FSSW (Friction Stir Spot Welding) and riveting techniques (see Figure 3.4) [29]. However, the process parameters applied in both works demanded welding times (1.8 and 7 s)

incompatibles with automotive industry efficiency needs, which require values around 1s for each weld [6,14].

Table 3.1 - Process Parameters and Shear Load results obtained by recent works of RFSSW in AA6082-T6 with 2 mm thickness sheet [6,14].

Author	PD (mm)	PT (s)	RS (rpm)	t (s)	Shear Load (kN)
Rodrigo Marschner [6]	2,1	0,9	2100	1,8	9
Xijing Wang [29]	2,7	3,5	2100	7	8,5

PD – Plunge Depth, **PT** – Plunge Time, **RS** – Rotational Speed, **t** – welding time

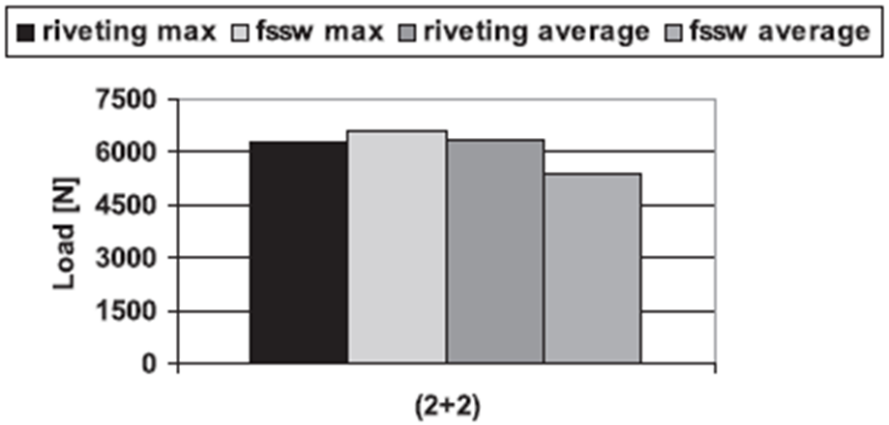

Figure 3.4 - Maximum and average Shear Load results of riveting and FSSW techiniques for AA6082 2 mm aluminum sheets [29].

3.2 Macro and microstructure of RFSSW welds

Aside from non-intrinsic features such as lack of filling, cracks and others, the RFSSW welds are characterized by the presence of a Stir Zone (SZ), a Thermal-Mechanically Affected Zone (TMAZ), and a Heat Affected Zone (HAZ). Other discontinuities such as hook, Bonding Ligament and the drop region [9,17,18,20,24,30,31] can be present. Figure 3.5 shows a macrostructure exhibiting each one of those features in a weld produced by RFSSW in AA6082-T6 alloy. All these features seem to have some effect on the strength of the weld,

therefore, a clear understanding of them is needed to understand their role in the weld strength and fracture behavior of RFSSW welds.

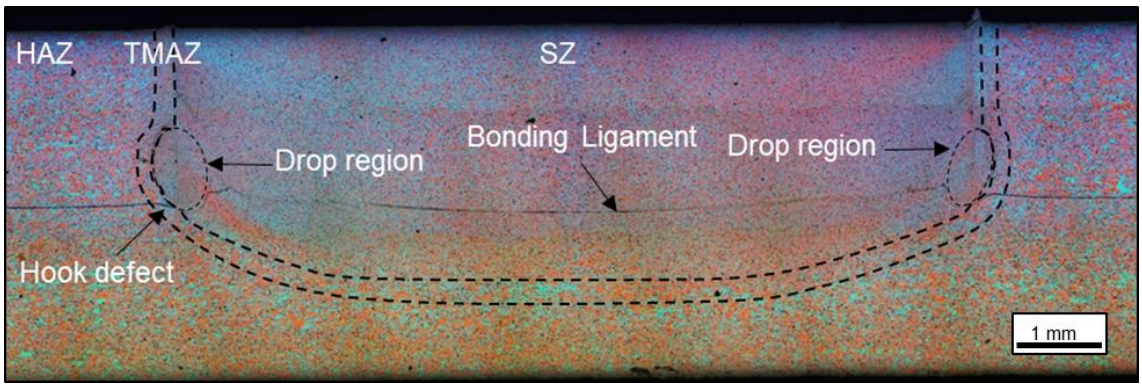

Figure 3.5 - Cross section macrostructure of AA6082-T6 weld produced by RFSSW indicating SZ, TMAZ, HAZ, hook defect, Bonding Ligament and Drop region.

Figure 3.6 (a) shows that the SZ microstructure consists of refined equiaxed grains. This microstructure results from high levels of deformation and temperature applied in this region, leading to dynamic recrystallization [16,17,26]. Figure 3.6 (b) shows the TMAZ microstructure with higher magnification. This region also undergoes to a high level of deformation and temperature. However, these levels are lower than the ones reached in SZ region, resulting in an incomplete or partial dynamic recrystallization mechanism. These conditions lead to an elongated grain structure with grains oriented along the direction of the tools rotational movement [16,17,26,32].

Figure 3.6 (c) shows a typical microstructure of the transition region between Heat Affected Zone (HAZ) and the Base Material (BM) in RFSSW. Differently from SZ and TMAZ, HAZ reaches a negligible or no level of deformation during the weld. Therefore, this region is only subjected to thermal effects. Since the welding process is completed in very short periods (1-10 s), no significantly grain size enlargement is reported in most works of RFSSW [16,17,26]. Regarding HAZ identification, several works have applied hardness test to determine size and shape of HAZ in RFSSW [9,16–18,24]. This method is typically reported for precipitation strengthened alloys such as 2XXX, 6XXX and 7XXX aluminum alloy series. For instance, Figure 3.7 shows hardness profiles in

different regions of a AA2219-T851 weld produced by RFSSW, which shows a steep drop in hardness from BM to HAZ region [16,17,26,32,33].

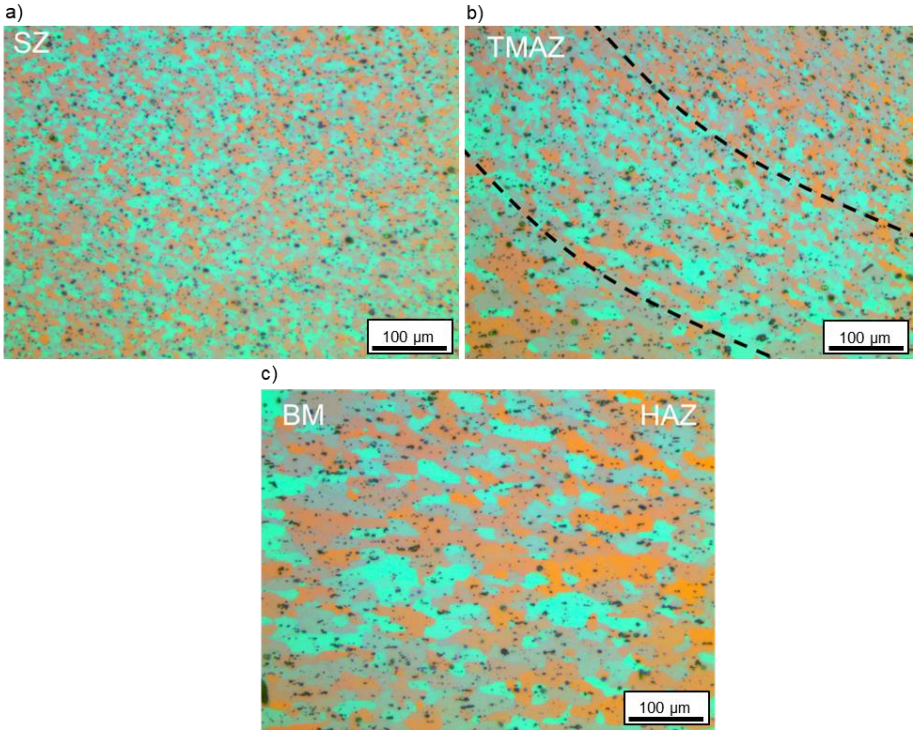

Figure 3.6 - Microstructure of a) SZ b) TMAZ c) HAZ in an AA6082-T6 weld produced by RFSSW.

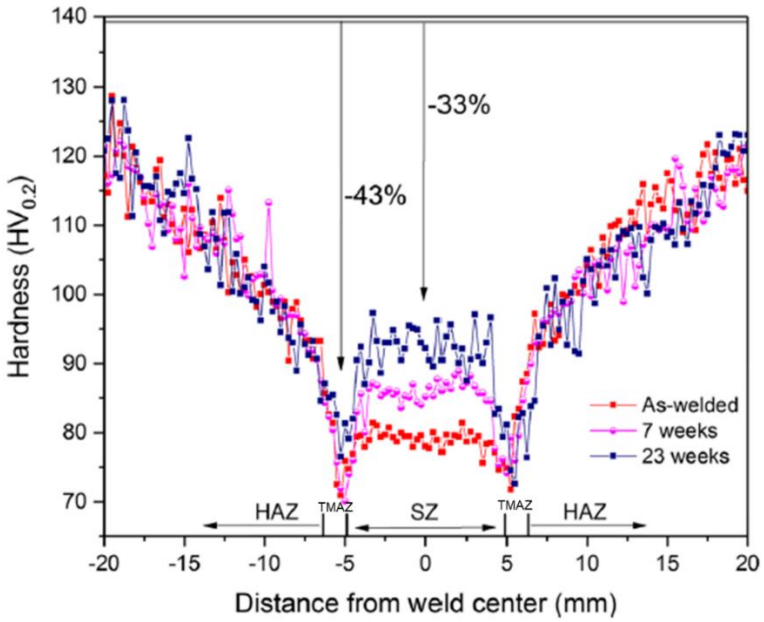

Figure 3.7 - Hardness profile in different regions of a AA2219-T851 RFSSW weld in different natural aging times [33].

Hook defect and Bonding Ligament are shown with higher magnification in Figure 3.8 (a) and (b), respectively. Hook is an intrinsic defect of RFSSW welds characterized as a transitional region between the bonded and unbonded regions of the weld. Therefore, it is characterized as a partially bonded region [6,9,23,34]. There have been several studies reporting hook formation in different shapes and sizes [6,9,18,23,34,35]. Bonding Ligament is an interface region that lies between the upper and lower sheets. This feature is related to the oxide film on the sheets surfaces that remains unmixed during welding process [17,20,23,24,31]. Usually, the Bonding Ligament does not impair the adhesion between the sheets, resulting in satisfactory resistance, even though the sheets tend to get separated by tearing mechanisms along the Bonding Ligament [17].

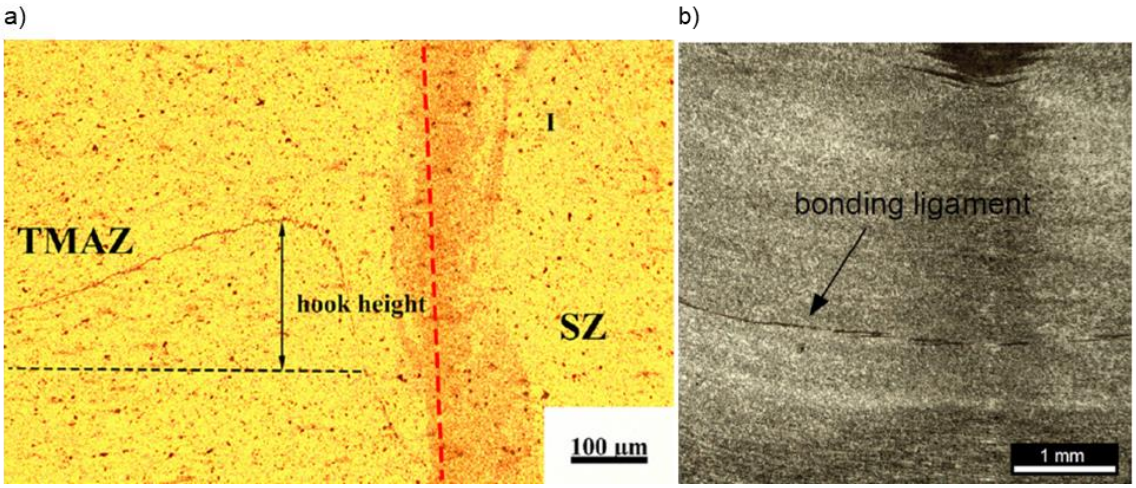

Figure 3.8 - a) Hook defect in a AA6061-T6 RFSSW weld b) Bonding Ligament in a AA2198 RFSSW weld [9,26].

Figure 3.9 shows a schematic illustration of a drop region formation presented by Shen et al [31]. Drop region is a feature formed during the refilling stage, when the material that is refilled in the cavity caused by sleeve retraction is compressed and sheared, leading to a circular material flow underneath the sleeve path. This region is characterized for having a droplet shape formation as it can be seen in Figure 3.10. This region has a small grain structure due to the high level of shear and compression applied during the refilling stage [18,31].

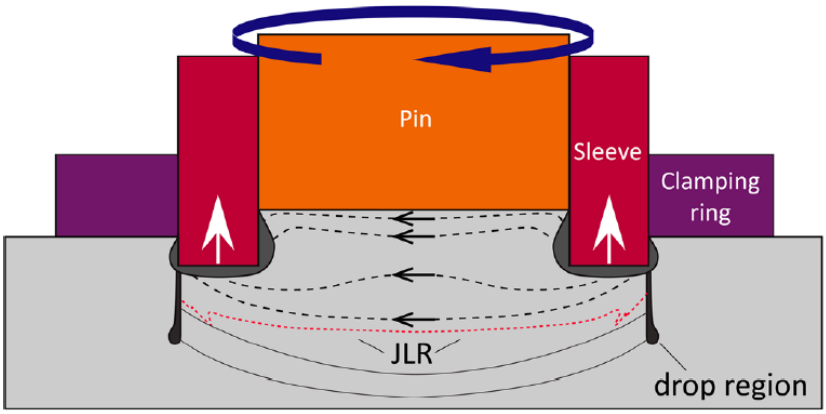

Figure 3.9 - Schematic illustration of Drop region formation during RFSSW [31].

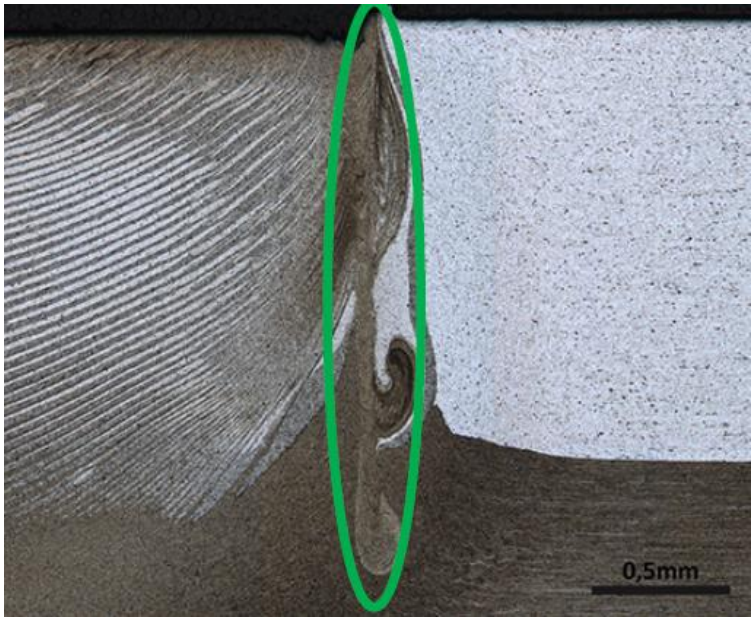

Figure 3.10 - Drop region in a RFSSW weld [18,31].

3.3 Influence of RFSSW parameters on weld structure and strength

3.3.1 Heat input

Differently from fusion welding techniques, in which most of the welding efficiency depend on heat input, friction welding depend on the mutual effect of heat input and strain energy, therefore, it is difficult to separate the individual effect of each factor on the weld properties [12,36–39]. However, several studies associate the heat (or energy) input during Friction Spot Welding process with

welding parameters, such as axial force, penetration depth, rotational speed, welding time and torque, according to Equation 3.1 [26,37–39].

$$Q = \sum_{n=1}^{n=N} Force(n)(x_n - x_{n-1}) + \sum_{n=1}^{n=N} Torque(n)\omega(n)\Delta t \qquad (3.1)$$

Where (x_n) is plunge depth in a sample incremental value (n), (ω) is tools angular speed (rad/s), (N) is the sample final increment and (Δt) is sample time. Analyzing Equation 3.1, it is noted the relation of the first term of the equation with the demanded force to execute the plunging process. Therefore, this term has contributions from the plunge depth parameter. The second term of Equation 3.1 takes into account the necessary torque to plasticize the material during the welding process, which has contributions from the rotational speed and feeding rate [26,37–39]. Given the influence of each parameter in the heat input, it can be concluded that the higher is the values of plunge depth (or Force) and rotational speed, and the lower is the feeding rate (increasing Δt), the higher is the heat input during the welding process.

Gerlich et al. [39] have reported the influence of energy input in Fracture Load of Al 5754 aluminum alloy and AM60 magnesium alloy using Friction Stir Spot Welding (FSSW). Better mechanical properties were reported for higher energy input values, as it can be seen in Figure 3.11. According to the authors, mechanical performance enhancement is related with high energy levels due to the larger bonded zone volume produced [39].

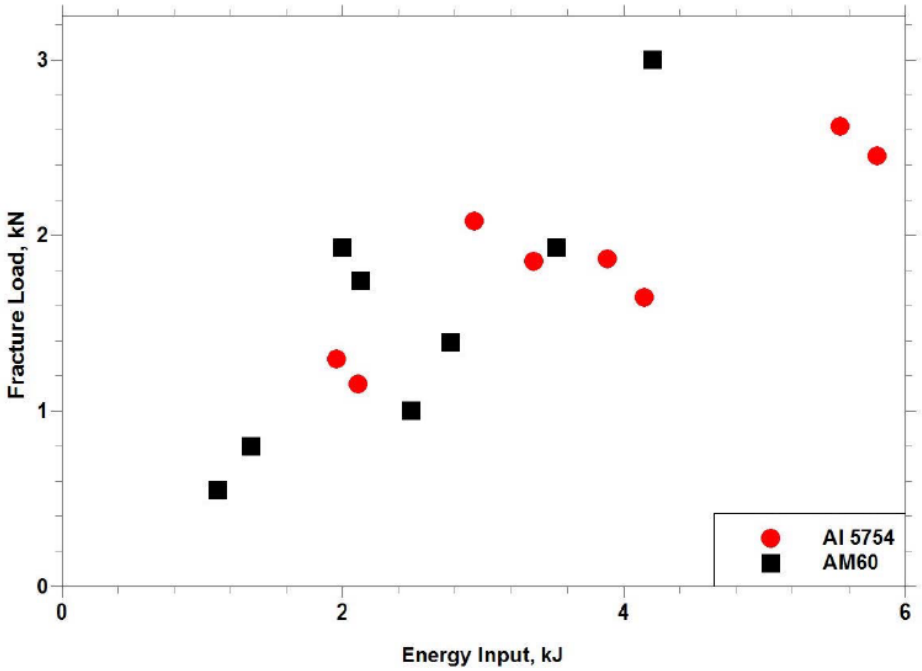

Figure 3.11 - Effect of energy input in mechanical performance of welds of Al5754 and AM60 produced by FSSW [39].

3.3.2 Plunge Depth

According to Cao et al. [9], the Plunge Depth parameter has a straightforward effect on the weld strength of AA6061-T6 alloy produced by RFSSW. The authors showed that the Plunge Depth determined the position and size of the hook defect, which determines the final mechanical properties of the weld. For low values of plunge depth (lower than the sheet thickness), the hook is formed in the SZ region. On the other hand, for high values of plunge depth (higher than the sheet thickness), the hook is formed in TMAZ region as shown in Figure 3.12. Besides that, it was determined a correlation between plunge depth and other processing parameters regarding the hook height (distance between the original interface of the sheets and the tip of the hook). Based on hook height measurements, a linear relation between Tensile Shear Strength and hook height (Figure 3.13) was reported [9]. From this trend it was assumed that better mechanical performance is obtained by reducing the hook height.

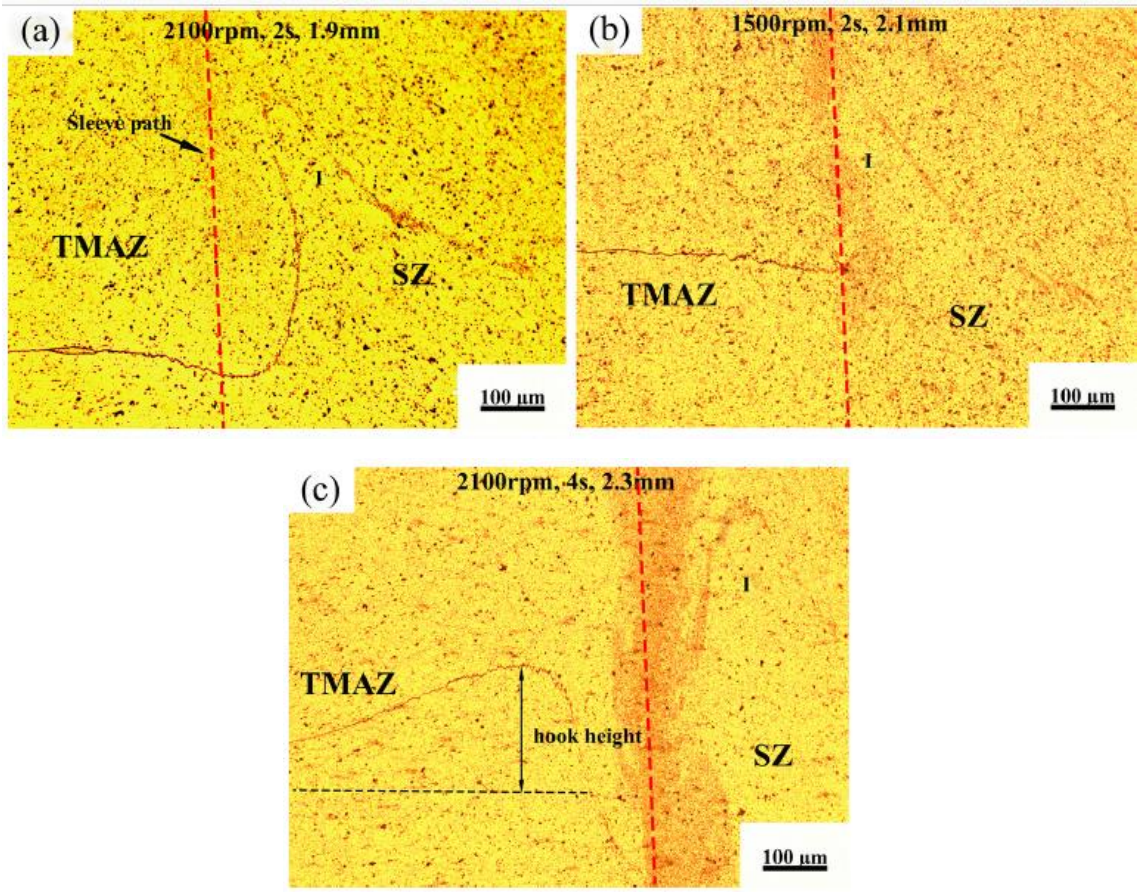

Figure 3.12 - Hook tip position in AA6061 RFSSW for different plunge depth values a) 1.9 mm b) 2.1 mm and c) 2.3 mm [9].

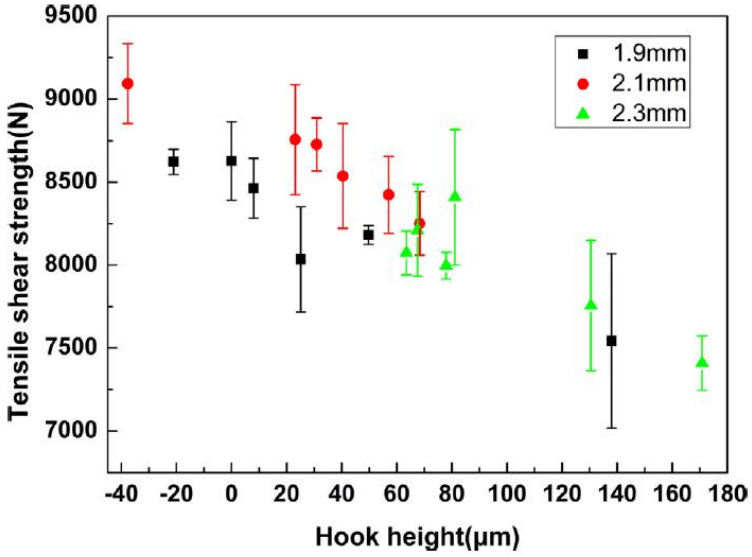

Figure 3.13 - Linear relation between Tensile Shear Strength and Hook Height for AA6061 welds produced by RFSSW [9].

Similar to Cao's observations, several works have linked tensile shear strength to plunge depth values and consequently to hook height values [6,18,24–26,30]. Plunge depth was also linked to fracture mode in different works. Most of the observations reported two types of fractures during shear tests, interfacial/through the weld (TW) fracture that occurs along the interface between the welded sheets, and circumferential/pulling out (PO) fracture that Pull-Out the welded nugget from one or both sheets. It is often observed that PO fracture occurs for high values of plunge depth and TW usually happens for low values of plunge depth [6,18,25,35].

3.3.3 Rotational Speed

Shen et al. [40] suggested that lap shear strength of RFSSW welds is enhanced with increasing of rotational speed when a standard tool profile is used. The same trend was observed for a tool with grooves on the tip of the sleeve but not as significantly as observed in the standard tool as shown in Figure 3.14 [40]. On the contrary, Cao et al. [9] showed that high rotational speed increased hook height values, diminishing the shear strength. Different trends of the effect of rotational speed on the weld strength is reported by different authors and no general agreement was found [16–18,20,23,25,26,41,42]. However, it is important to point out that in most of these works more than one parameter was changed at the same time, and there are few evaluations considering the effect of parameters interaction. Besides that, it is not clear if parameters as rotational speed and feeding rate have the same effect for different alloys.

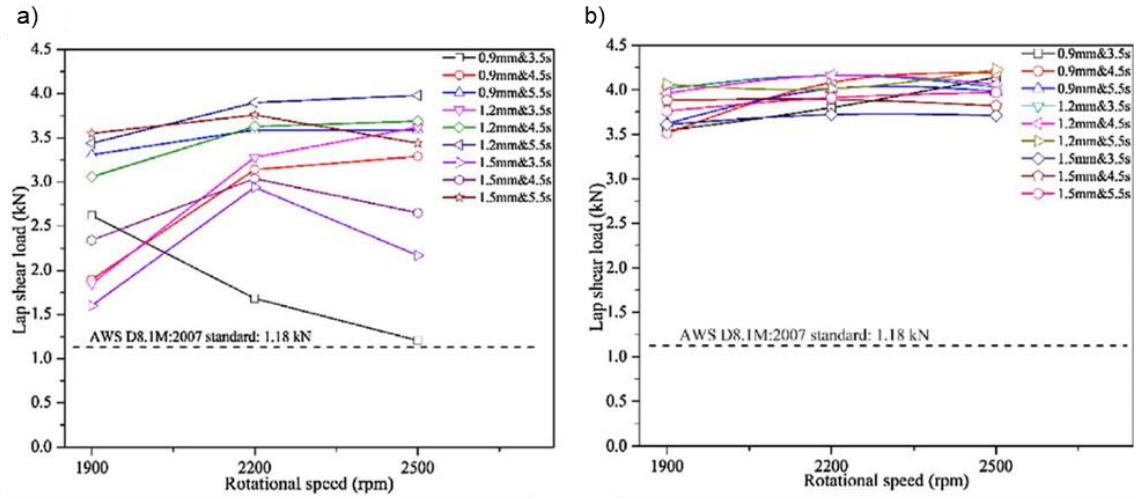

Figure 3.14 - Effect of Rotational Speed on Shear Strength of AA6022-T4/AA7075-T6 RFSSW weld for a) standard tool profile b) modified tool with grooves on the tip of the sleeve [40].

3.3.4 Feeding Rate/Welding time

Feeding Rate/Welding time have been reported as parameters that have effect on the weld strength in most works of parameters optimization for RFSSW. Again, there is some controversial trends, some works have related the effect in weld strength based on heat input and others in hook and/or other macro/microstructure features formation. Heat input associations have demonstrated that higher weld strength is obtained for high values of welding time (or low values of feeding rate) due to better bonding levels at the Bonding Ligament. On the other hand, macro/microstructure associations have shown the opposite trending due to high levels of welding time, which resulted in more pronounced hook heights and steeper curvature of this feature, thus diminishing weld strength. There is also evidences of defects formation in extreme conditions of these parameters because of changing in the stirring mechanisms and friction effectiveness. Therefore, no general trend between these parameters and the weld strength was found [2,3,4,6,11–13,27,30,31,32].

The individual effect of each process parameter in weld strength is often measured using statistical analysis of designed experiments [9,16,18,20,25,26,41–43]. Most of these works have shown higher relevance of

plunge depth instead of rotational speed or welding time/feeding rate. For example, Castro et al. [26,42] showed a lower influence of welding time on weld strength when compared to plunge depth and rotational speed in AA2198-T8 RFSSW welds. On the other hand, Barros et al. [25] have reported lower influence of rotational speed on the weld strength compared to plunge depth and welding time in RFSSW for the same alloy. These results are shown in Figure 3.15 and they highlight again the relevance of plunge depth over the other parameters.

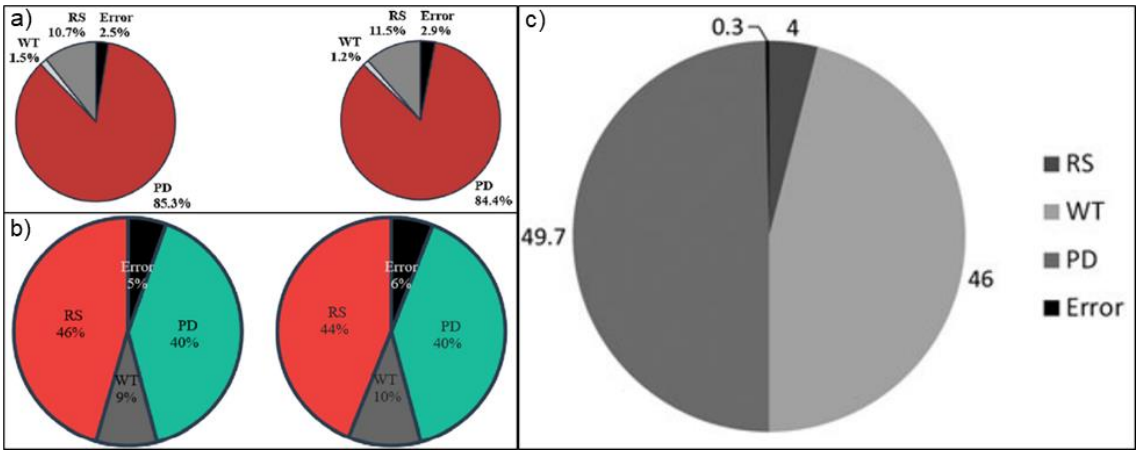

Figure 3.15: Parameters influence in weld strength determined by statistical analysis from RFSSW welds of a) AA2198 b) AA2198-T8 c) AA2198-T8 [25,26,42].

3.4 Aluminum alloys of 6XXX series and AA6082-T6 alloy

6XXX are a group of aluminum alloys based on the system Al-Mg-Si. This alloy group presents high specific strength combined with good weldability and good corrosion resistance. Therefore, these alloys are extensively applied in extruded and rolled components in automotive industry [2,3,6,7,9]. Mechanical properties of 6XXX alloys are mainly controlled by the distribution, size and shape of Mg_xSi_y precipitates (secondary phases), which are formed in α-aluminum matrix via solution, quenching and aging treatment [7]. Precipitation and dissolution mechanisms have been studied and reported along the years for these alloys using thermal analysis (Differential Scanning Calorimetry - DSC),

high Resolution microscopy techniques (Transmission Electron Microscopy, Scanning Transmission Electron Microscopy, High Resolution Transmission Electron Microscopy - TEM, STEM, HRTEM), and diffraction techniques in TEM (Selected Area Electron Diffraction - SAED) [7,8,44,45].

Based on several studies, it is reported a complex precipitation sequence for these alloys, which is usually simplified as (sss) → clustering → GP-Zone (Guinier Preston) formation → β" precipitation (Mg_5Si_6) → β' precipitation (Mg_9Si_5) → β precipitation (Mg_2Si), where sss is a supersaturated solid solution obtained from solution treatment and quenching process. Size, shape and distribution of precipitates are controlled by kinetic process, which depend on initial microstructural conditions, chemical composition and heat treatment parameters [7,8,44–46].

Crystal structure, morphology and chemical composition have been reported up to date for different phases in 6XXX series alloys in several heat treatment conditions [8,44,47–55]. Clusters, co-clusters of Mg and Si and GP-zones formation have been detected through resistivity measurements techniques, thermal analysis (DSC) and more recently with high resolution microscopy and tomography techniques such as HRTEM and 3DAP (3D-atom-probe). For instance, Figure 3.16 shows the size and shape of GP-Zones in Al-0.65Mg-0.70Si after a pre-aging treatment (70 ºC during 16 hours) measured by 3DAP. Numerous works characterized GP-Zones in Al-Mg-Si alloys in size scale around 1-3 nm, spherical shape, with complete coherency with aluminum matrix and chemical composition of Mg/Si close to 1 [47–51,55].

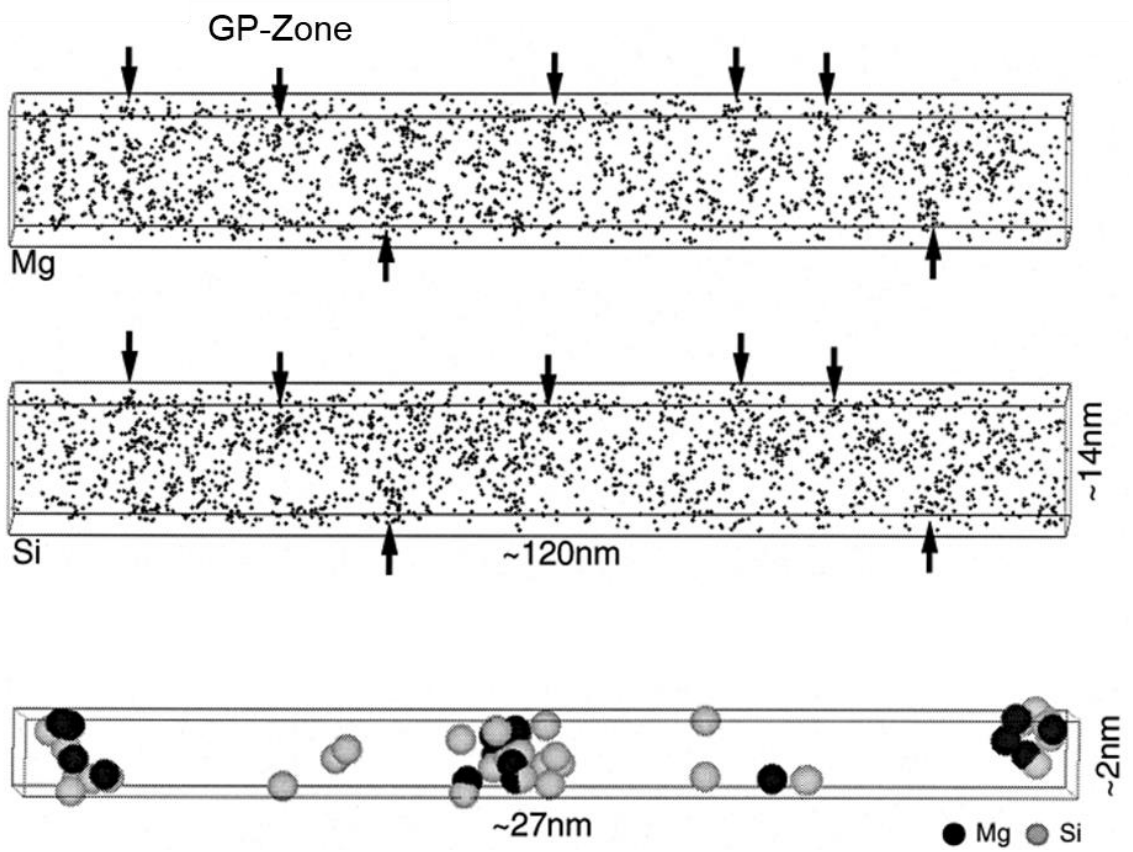

Figure 3.16 - 3D-atom probe analysis of size and shape from GP zones in a Al-0.65Mg-0.70Si sample after pre-ageing treatment of 70 ºC for 16 hours [48].

β'' (Mg_5Si_6) formation is associated to peak ageing conditions in 6XXX alloys, which is designated as T6 treatment and comprises heating temperatures around 180 ºC for 10-12 hours. β'' phase has monoclinic crystalline structure, needle shaped morphology aligned to $<100>_{Al}$ direction, presents high level of coherency along this axis direction and reaches dimension size of 4x4x50nm as shown in Figure 3.17 [47,49–51,54,55]. Figure 3.17 (d) also shows the β' phase (Mg_9Si_5), which is formed in overaged conditions. β' is characterized as thick needle shape or rod shaped phase, with hexagonal crystalline structure and reaches dimension size of 20x20x500 nm. Hardness reductions are detected in aluminum alloys with excessive formation of β' due to the low level of coherency of this phase with α-aluminum matrix [49,54].

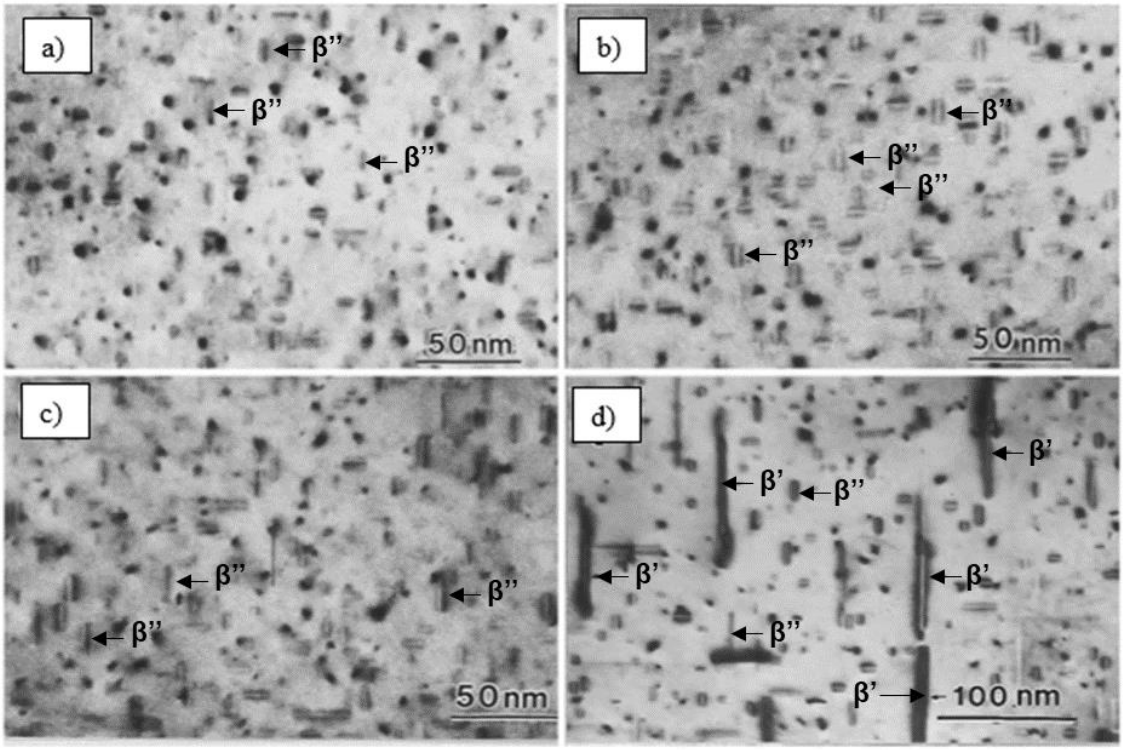

Figure 3.17 - Precipitates size and morphology in AA6061 alloy solutioned and aged for a) 175 ºC during 30 minutes b) 175 ºC during 4 hours c) 175 ºC during 72 hours d) 200 ºC during 20 hours [51].

β (Mg_2Si) phase has a cubic crystalline structure, presents rod shape or irregular shape morphology and reaches dimensions around (10-20µm). This phase is obtained after meta-stable phases (GP-zones, β'' and β') reaches the equilibrium state. β shows irrelevant or no level of coherency with the aluminum matrix. [44,49,54].

Birol, Y. [45] has identified 8 enthalpic effects from dissolution and precipitation process for AA6082 alloy using DSC analysis. Figure 3.18 shows the 8 signals reported by Birol based on the simplified precipitation sequence explained before. The first peak determined around 80-90 ºC (signal 1) is an exothermic process related to extensive clustering process, since the sample underwent to solution treatment and quenching, generating a super saturated solid solution (sss). A second weak signal detected around 160 ºC (signal 2) is described as an exothermic reaction caused by GP-Zone formation, which is followed by an endothermic reaction of dissolution process from a fraction of

clusters and GP-Zone (signal 3). An exothermic peak (signal 4), is related to β'' precipitation, and it is reported to occur around 240 ºC. In a slightly higher temperature, close to 300 ºC (signal 5), β' is precipitated from β''. Approximately in 450 ºC, an endothermic signal is reported as dissolution of β'' and β' (signal 6) which is followed by an intense exothermic peak from β precipitation (signal 7). Finally, dissolution process of all phases takes place in temperatures higher than 530 ºC (signal 8) [45].

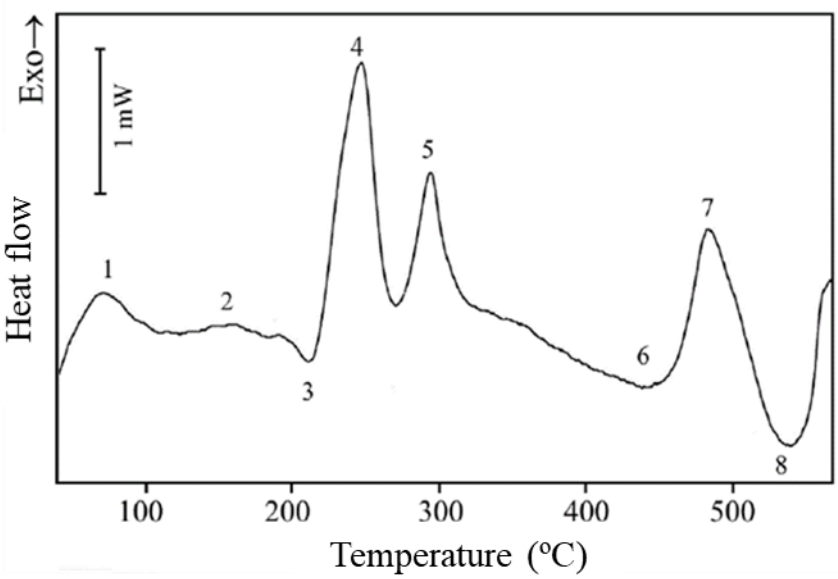

Figure 3.18 - DSC curve of AA6082 disc samples with solution treatment, obtained by heating at 10 ºC min^{-1} [45].

Mechanical properties of precipitation strengthened alloys (2XXX, 6XXX and 7XXX, for example) might suffer severe changes based on the heat treatment applied. For instance, the tensile strength of the AA2198 alloy can vary from 200 to 500 MPa, only by varying heat treatment. Similar changes are observed in Yield Strength and elongation [56–60].

Table 3.2 also shows the wide range of properties for the AA6082 alloy subjected to different heat treatments. Although the versatility have provided space for these alloy in several industrial applications, it also brought challenges regarding its welding and joining process since the AA6082 alloy is highly sensitive to thermal effects [56].

Table 3.2 - Mechanical properties of AA6082 alloy in different heat treatment conditions [56].

Specification	σ_y (MPa)	σ_{max} (MPa)	Tensile Strain (%)	Hardness (HV)
O	60	130	27	35
T4	170	260	19	75
T6	310	340	11	100

O - Annealed

T4 – Solutionized, quenched and naturally aged

T6 – Solutionized, quenched and artificially aged

3.5 Precipitation and coarsening in solid state welding techniques

Precipitation and coarsening effects on precipitation strengthened welded alloys using solid state techniques have been reported in several works [61–72]. Most of these works applied Friction Stir Welding or Friction Stir Processing (FSW/FSP) for their studies. These techniques are quite similar to RFSSW and provide useful information to explain precipitation and coarsening process in different weld regions.

Two important factors in solid state welding that determine precipitation and coarsening effects are the thermal and strain evolution during welding. Figure 3.19 shows a schematic representation of temperature and strain distribution in the microstructural zones of a Friction Stir Weld. It is noted a gaussian distribution for both temperature and strain, with the maximum values being reached in the SZ region, whereas in the HAZ both factors have considerably smaller contributions [61,64,73].

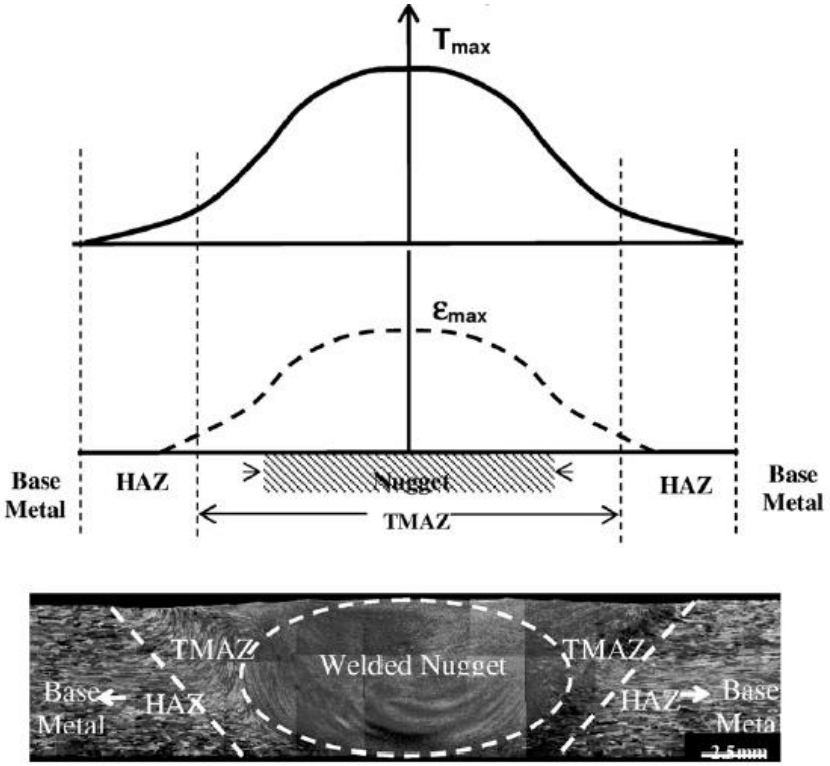

Figure 3.19 - Schematic representation of temperature and strain distribution in the microstructural zones of a Friction Stir Weld (FSW) [73].

During welding process, the stir zone region reaches temperatures around 400-550 ºC and high levels of strain. At such conditions, precipitates in aluminum alloys can grow, break or dissolve into aluminum matrix depending on alloy type. On the other hand, in the HAZ the strain levels are negligible and usually this region reaches temperatures above 250 ºC, which may cause coarsening process and increasement of Precipitate-Free Zones (PFZ). TMAZ is a transition region between SZ and HAZ, therefore dissolution and precipitation process depend on the thermal cycle and strain levels experienced by this region [61,64,73].

According to Dong et al. [72], the effect of natural aging on Friction Stir Welded 6005A-T6 has a significant impact on microstructure and microhardness changes. It was reported a softening behavior in SZ and TMAZ, which was related to the dissolution of β'' and re-precipitation, whereas a softening in HAZ region was related to overaging conditions, and formation of β'. Regarding post-welded natural aging, Figure 3.20 shows that SZ and TMAZ recovers a significant level

of hardness after 4 weeks of natural aging, which was associated to clustering and GP zone formation. The HAZ did not present changes because of low solute concentration.

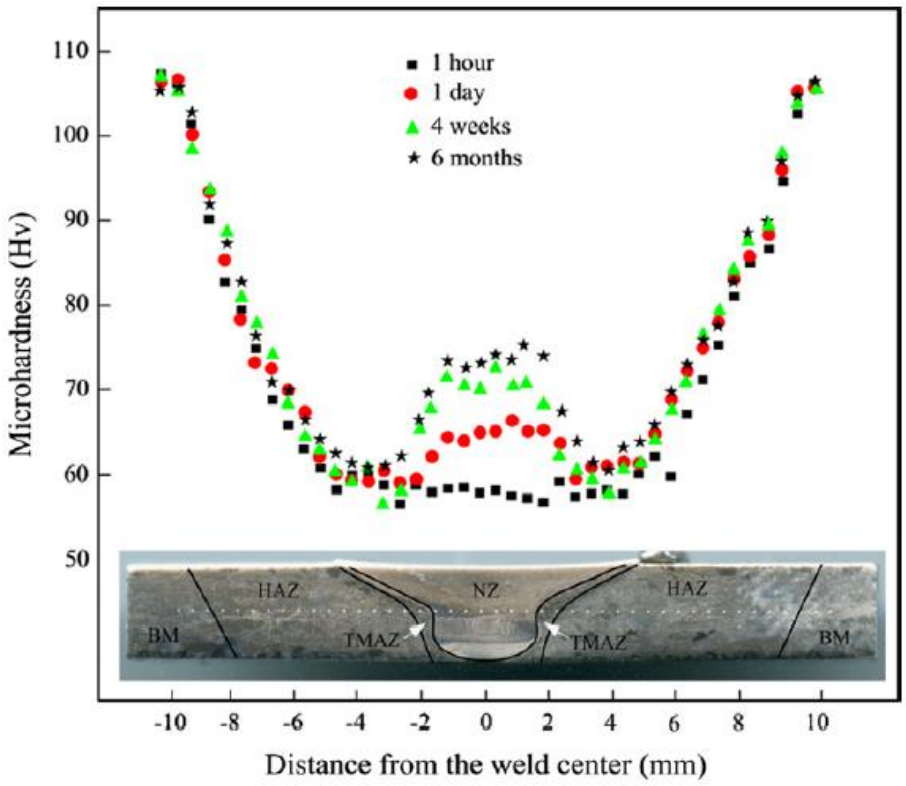

Figure 3.20 - Natural aging effect on microhardness of AA6005-T6 alloy welded by FSW [72].

Differently from Dong, Chen et al. [69] reported partially dissolution from Al_3Mg_2/Al_6FeMn precipitates and coarsening process for Mg_2Si precipitates in the stir zone of a 5A06 aluminum alloy. However, it must be emphasized that different alloys might have different dissolution behavior and it was applied lower heat-input process parameters in Chen's work. For instance, rotational speed values were 700 and 800 rpm in Chen's work, while Dong's applied 1200 rpm.

Regarding the association between precipitation evolution and process parameters (or heat input), Figure 3.21 shows the volume fraction and morphology changes of β'' and β in an AA6082-T6 during welding process for two transversal welding speed. It is observed that for 300 mm/min, the volume fraction of both precipitates are reduced to insignificantly levels and to very small sizes

(Figure 3.21 (a) and (b)), whereas for 30 mm/min, β phase remains in the stir zone during welding, its volume fraction increases after a certain time and β'' is completely dissolved in aluminum matrix or transformed into β (Figure 3.21 (c) and (d)) [68].

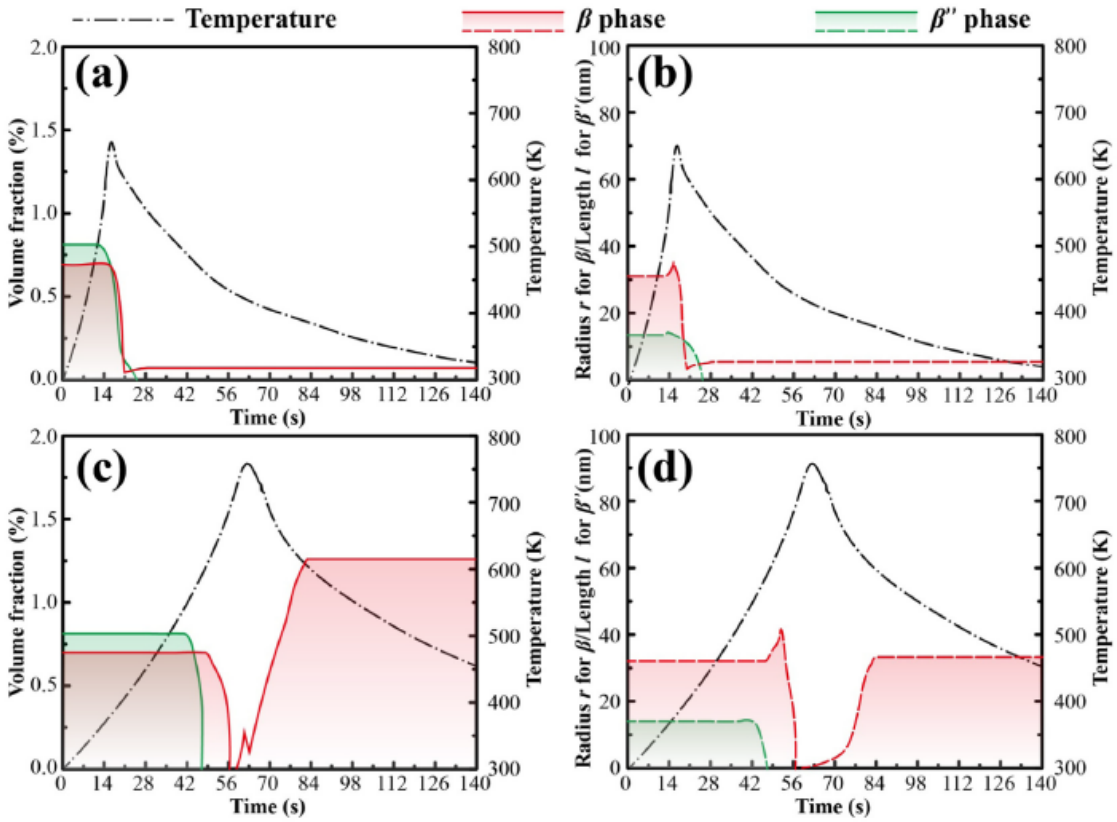

Figure 3.21 - Variations of precipitates during FSW a) volume fractions and b) geometrical sizes at 300 mm/min; c) volume fractions and d) geometrical sizes at 30 mm/min [68].

Baghdadi et al. [67] have investigated the effect of FSW process and T6 post weld heat treatment in mechanical properties from AA6061 alloy. Figure 3.22 compares Friction Stir Welded condition (FSWed), Post Welded Heat Treated (PWHTed) condition and the as-received material. It is observed that FSWed presented lower strength and ductility, which is related to solution process from the strengthening elements in SZ/TMAZ and coarsening effect in HAZ. It was also reported a serrated flow pattern, which was attributed to a nonuniform distribution of hard Mg_2Si particles. However, PWHTed have shown similar mechanical

performance to as-received material, demonstrating that initial properties might be recovered using heat treatments restoring precipitates conditions.

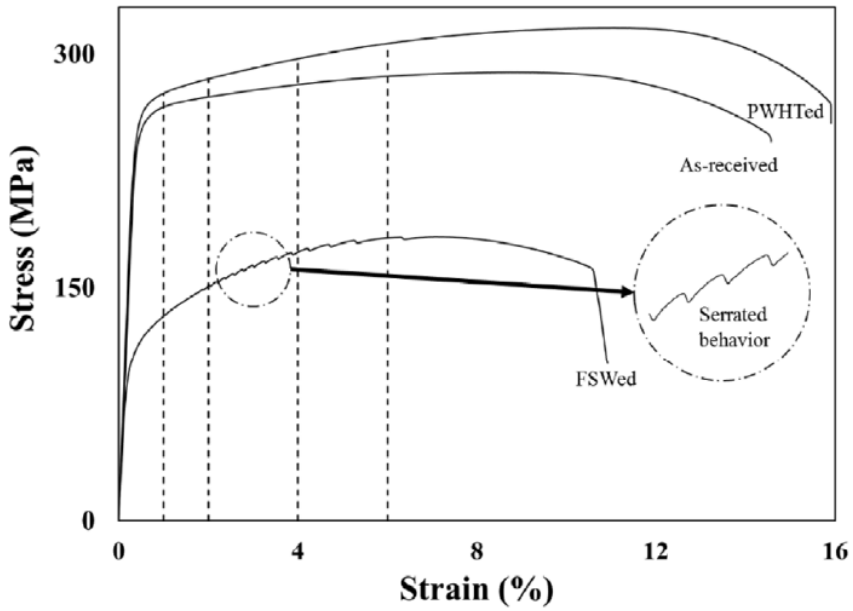

Figure 3.22 - Stress-Strain curves from as received, Friction Stir Welded and Post Welded Heat Treated (PWHTed) AA6061 aluminum alloy [67].

In this topic, the effect of solid state joining techniques in precipitation and dissolution process in heat treatable aluminum alloys was summarized. It was observed a trend of coarsening behavior in HAZ due to less intense heat input in comparison to SZ region. On the other hand, SZ/TMAZ may present either dissolution or coarsening/dissolution processes depending on the process parameters (heat input). Regarding these conditions, post welded heat treatments as artificial or natural aging might determine mechanical performance in automotive industry.

3.6 Bake hardening effect

Bake Hardening (BH) treatment is an important heat treatment widely used in automotive industry. It usually reaches temperatures around 180-200 ºC during 20-40 minutes, which for heat treatable aluminum alloys might cause relevant changes in the precipitation condition [7,74–78]. For example, Li et al. [7] showed

that the effect of Bake Hardening response in a solid solutioned Al-Mg-Si-Cu alloy depend on natural aging time previous to Bake Hardening treatment as shown in Figure 3.23. According to this work, a reduction of vacancy density and solid solubility occurs during Natural Aging (NA) and increases the critical nucleation size for the main strengthening β'' phase, which contributes to the decrease of BH response. Li pointed out that the effect of NA in conventional 6XXX series alloys is more pronounced. However, considering that the natural aging time after welding process in automotive industry is relatively short (less than 1 hour), Bake Hardening response is expected to have strong influence for these alloys.

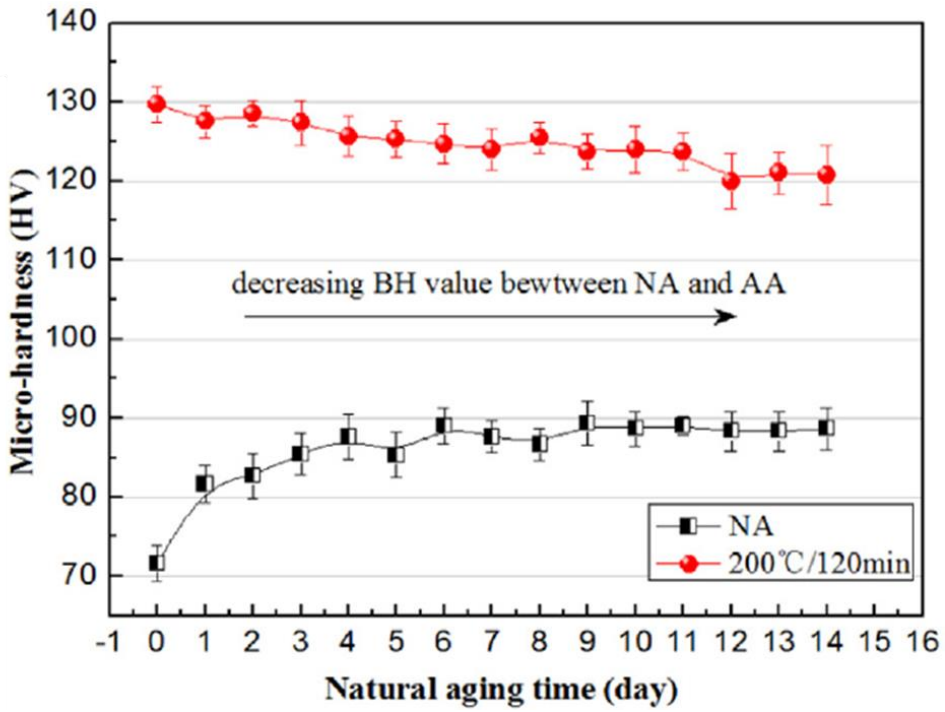

Figure 3.23 - Effect of natural aging on Bake Hardening response in a solid solutioned Al-Mg-Si-Cu alloy [7].

Li also demonstrated the effect of Bake Hardening treatment on the microstructure of an Al-Mg-Si-Cu alloy (Figure 3.24). By comparing the precipitation evolution of the solid solutioned alloy (Figure 3.24 (a)) with the bake hardened alloys, it was shown that Bake Hardening treatment causes intense β'' precipitation (Figure 3.24 (b)) [7].

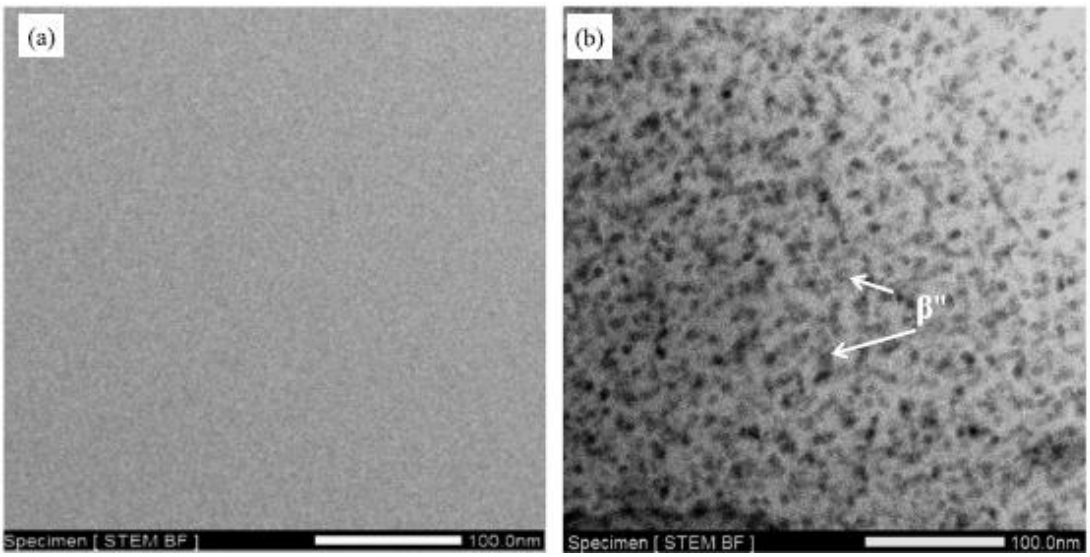

Figure 3.24 - Effect of Bake Hardening treatment in microstructural changes of an Al-Mg-Si-Cu alloy; a) supersaturated solid solution condition and b) bake hardened condition [7].

In addition to Li's works, other authors have discussed the effect of Bake Hardening in strength, fracture behavior, microstructural changes and the combined effect with alloying elements in precipitation kinetics [68–72]. These demonstrate the importance of the understanding of this treatment effect in aluminum alloys components for industry applications.

3.7 Fatigue properties in RFSSW

Cyclic loading in vehicle applications is a major performance concern, especially considering that RFSSW welds may contain a notch geometry which is rather susceptible to fatigue crack propagation [79]. In the literature it is reported few works on fatigue properties and fatigue fracture analysis of RFSSW welds [18,35,79–81].

Lage et al. [18] have evaluated fatigue behavior in Al-Mg-Sc and found a fatigue limit of approximately 9% of the ultimate lap shear strength. Effertz et al. [80] have determined similar fatigue limit in AA7075 welds produced by RFSSW (10% of the ultimate lap shear strength). Plaine et al. [81] have studied fatigue behavior in dissimilar welding of AA5754/Ti6Al4V and identified a superior fatigue

limit, around 15% of the ultimate lap shear strength. The same value were found by Brzostek et al. [35] in a fatigue study of AA2024-T3 RFSSW welds. Shen et al. [79] have characterized fatigue behavior for Mg/Mg similar and Mg/DP600 steel welds produced by RFSSW and determined fatigue limit values for both combination between 18-20% of the ultimate lap shear strength. These results demonstrated that RFSSW is not recommendable for applications with high load cyclic solicitation, especially for aluminum alloys [18,35,80]. It is worth mentioning that several works have applied Weibull statistical analysis [18,35,80,81], which allows the calculation of predicted fatigue life for different failure probability levels. Figure 3.25 shows some results applying this procedure and demonstrates a low scattering behavior, which means a high reliability in the fatigue life values measured.

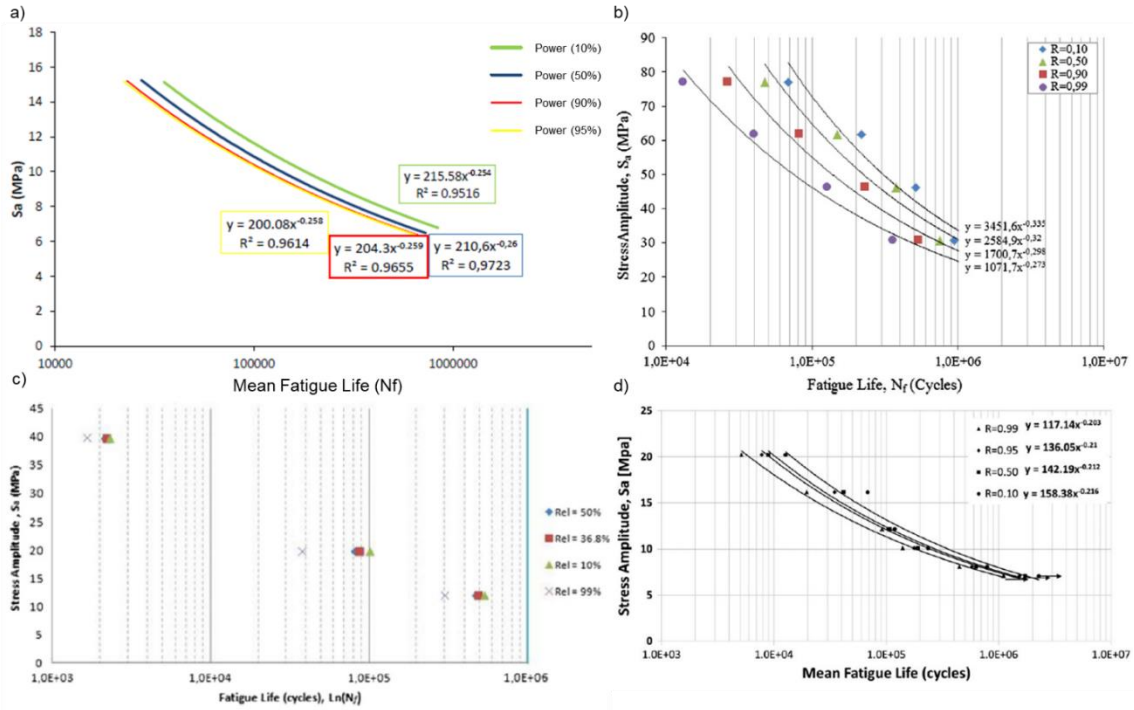

Figure 3.25 - S-N curves with different failure probability levels obtained by Weibull statistical analysis for RFSSW welds of a) Al-Mg-Sc [18], b) AA5754/Ti6Al4V [81], c) AA7050-T76 [80] and d) AA2024-T3 [35].

3.7.1 Fatigue Fracture behavior in RFSSW

Lage et al. [18] have observed the same fracture behavior in fatigue samples of Al-Mg-Sc for high and low cyclic solicitation. Multiple cracks initiation were identified in hook regions around the edge of the welded nugget, then the cracks initially propagated vertically by the sheet thickness followed by a propagation in the sheet width through the base material region, forming an Eyebrow (EB) shaped fracture as illustrated in Figure 3.26. It was also reported that for a few samples in high cyclic solicitation loads, the crack sheet thickness propagation occurred through the base material of the lower sheet, whereas in most samples for high and low cyclic solicitation, the crack sheet thickness propagation occurred between TMAZ/SZ region of the upper sheet. According to Lage et al. [18], this behavior is associated to the combined effect of stress concentration from the hook region and the metallurgical soft region produced between TMAZ and SZ, which favors fatigue crack propagation in this region as illustrated in Figure 3.27.

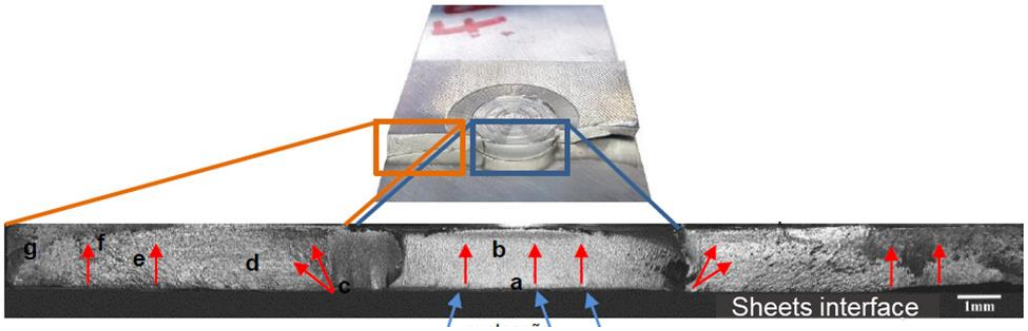

Figure 3.26 - Eyebrow fracture behavior observed in fatigue test samples of Al-Mg-Sc welded by RFSSW [18].

Figure 3.27 - Sheet thickness fatigue crack propagation by the base material and between SZ/TMAZ interface [18].

Analyzing fracture surface using Scanning Electron Microscope (SEM) technique, it was identified fatigue striation formation in almost the whole cross section fractured indicating that the crack propagation mechanisms remained the same independently from the microstructural region and that the crack propagation presented a stable behavior [18].

Plaine et al. [81] observed a similar fatigue failure behavior in high-cycle loading conditions in Al/Ti welds produced by RFSSW. However, for low-cycle loading conditions (loads higher than 30% of the ultimate lap shear strength) a through the weld fracture was identified, where apparently the primary crack emanate from the notch in the welded interface and propagated at the interface of the plates. According to Plaine et al. [81], as soon as the crack propagation reached a critical stage, where the shear stresses acting in the remaining cross section area could no longer sustain the shear overload, the interface failed. Plaine reported that even in this fracture behavior, cracks through the thickness following EB fracture mode were observed, but the interface failures occurred previously to the fully fracture evolution along the width direction as a result of the high loading conditions. Moreover, it was reported that through-thickness crack also contributed to the reduction of the joint area and thus to the interfacial failure.

A similar transition of fatigue fracture mode was evidenced by Shen et al. [79] for RFSSW of similar Mg/Mg joints. However, besides EB fracture for high-cyclic load conditions and TW fracture to low-cyclic load conditions, a third fracture mode called, nugget Pull-Out (PO) was observed in low-cyclic load conditions. But Shen et al. [79] have not recognized striation patterns in low-cyclic load fractured specimens. The authors found dimples at the fracture surface center, where shear fracture took place at the final crack propagation stage.

Effertz et al. [80] reported two fatigue fracture modes in AA7050-T76, again an EB fracture, similar to the one described in Lage's work, was observed for high-cycle load conditions, but a PO fracture was identified for low-cycle load conditions. Signs of damage from sliding, fatigue striations and smooth grain

surfaces were observed and the possibility of change in the failure mechanism due to a change in the stress state was discussed but not clearly described.

Brzostek et al. [35] observed three fracture modes in AA2024-T3 RFSSW joints in fatigue experiments. Similar to Lage's and Effertz's observations, Brzostek et al. [35] determined EB fracture in the upper and lower sheet for high-cycle conditions, whereas for low-cycle conditions PO fracture was reported. According to Brzostek, in PO fracture, the primary crack was initiated at the hook tip and propagated through the lower plate thickness. Subsequently, the crack propagated along the width, like high-cycle fatigue fracture. When the resistance area was too small, the joint could not sustain the overstress and the spot-weld catastrophic failed.

Some of the fatigue fracture surfaces of specimens in low-cycle load conditions mentioned in these previous works [35,79–81] are presented in Figure 3.28, making clear the complexity of fracture behavior analysis.

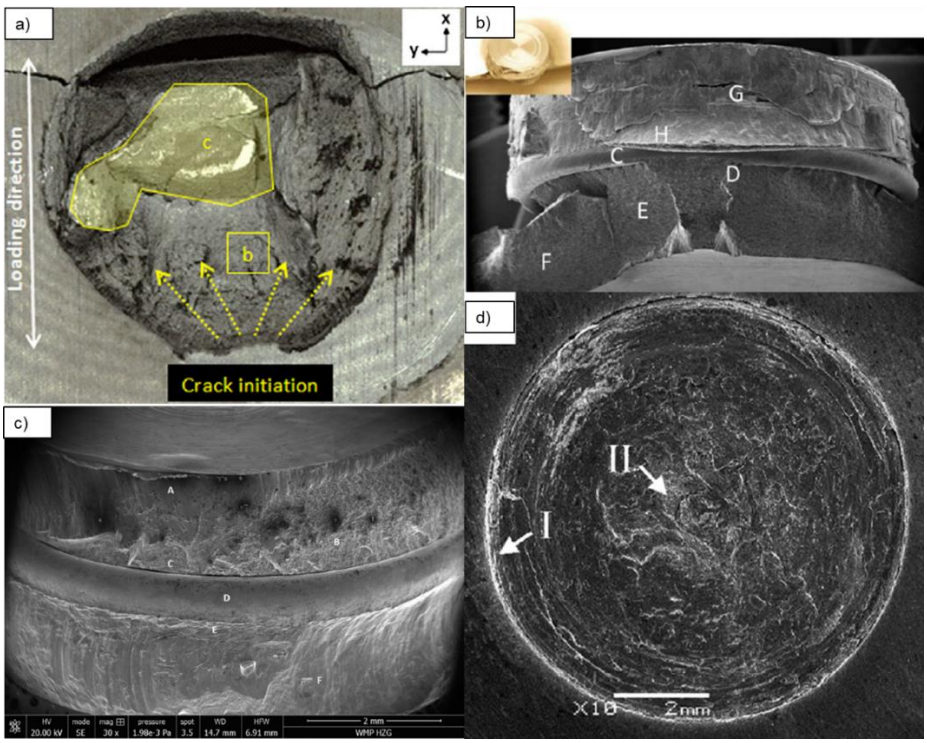

Figure 3.28 - Fatigue fracture surfaces of specimens tested in low-cycle conditions for RFSSW welds of a) AA5754/Ti6Al4V [81], b) AA2024-T3 [35], c) AA7050-T76 [80] and d) ZEK 100 magnesium alloy [79].

Considering the discussion made on these previous works, we can conclude that there is a general trend of EB fracture for high-cycle fatigue conditions, a complex fracture behavior in low-cycle conditions and that crack initiation occurs around hook region. However, there is a need for further investigations in fatigue fracture behavior of RFSSW welds, for example, it is still unclear the effect of hook tip shape on fatigue life, fatigue crack initiation and propagation.

4 MATERIALS AND METHODS

4.1 Materials

The material used for this work was 100x25.4x2 mm sheets of AA6082-T6 aluminum alloy. Chemical composition in weight percentage is presented in Table 4.1.

Table 4.1 - Chemical composition of AA6082-T6 aluminum alloy in weight percentage (wt.%).

Si (%)	Fe (%)	Cu (%)	Mn (%)	Mg (%)	Zn (%)	Cr (%)
0.7-1.3	0.5 Max	0.1 Max	0.4-1.0	0.6-1.2	0.2 Max	0.25 Max

4.2 Welding machine and tool

Welds were produced by a Harms Wende machine RPS100® available in HZG. The machine has a software interface to control the time of each stage from the welding process explained in Figure 3.2 and also control the pin/sleeve position and rotational speed. Moreover, the clamping ring pressure can be changed manually by a pneumatic actuator.

The three elements of the welding tool exhibiting diameter and concentric attachment configuration are shown in Figure 4.1 (a) and (b) respectively.

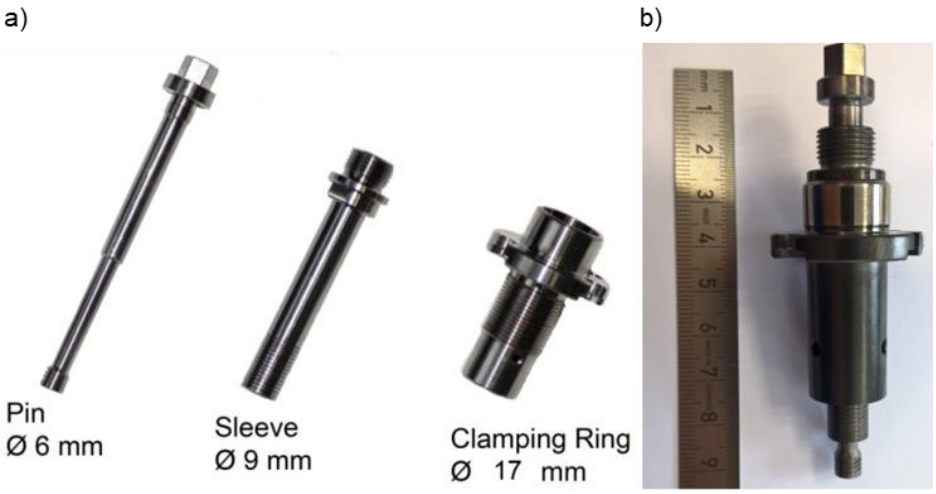

Figure 4.1 - a) Tools elements and b) tool concentric attachment configuration.

4.3 Process Parameters Optimization

4.3.1 Preliminary Study

Based on the characteristics of the welding machine available in HZG and in the literature review of process parameters effect in weld strength, the three process parameters chosen to be studied in this work were Plunge Depth (**PD**), Rotational Speed (**RS**) and Feeding Rate (**FR**) (Plunge Depth/Plunging Time). The initial process parameters window studied were determined by a preliminary evaluation of weld quality. This preliminary study involved a qualitative evaluation of weld surface, by evaluating the presence of rough surfaces defects such as cracks or lack of refilled material. It was tested 5 sets of process parameters with different values of plunge depth, rotational speed and feeding rate. Based on Equation 3.1, a high heat input set (high plunge depth, high rotational speed and low feeding rate) and a low heat input set (low plunge depth, low rotational speed and high feeding rate) were applied. Table 4.2 shows that sample 4 presented no surface defect applying a low heat input combination of process parameters (**PD**:1.8 mm, **RS**:1800 rpm and **FR**:4.5 mm/s) and sample 5 presented no surface defect applying a high heat input set of process parameters (**PD**:2.2 mm, **RS**:2600 rpm and **FR**:3.5 mm/s).

Table 4.2 - Preliminary study of weld surface defects from high and low heat input set of process parameters.

Sample	PD (mm)	RS (rpm)	FR (mm/s)	t (s)	Surface Defect
1	1.8	1500	4.5	0.8	Yes
2	2.2	2500	3.5	1.26	No
3	1.8	1700	4.5	0.8	Yes
4	1.8	1800	4.5	0.8	No
5	2.2	2600	3.5	1.26	No

4.3.2 Design of Experiments

From the two set of process parameters determined in the preliminary study it was defined the experimental welding sets for mechanical tests evaluation using Box Behnken Design. Box Behnken Design belongs to the class of rotatable or nearly rotatable second-order designs, based on three-level incomplete factorial designs [82]. Figure 4.2 shows Box-Behnken design for three factors that was applied in this work. This design contains three parts of four runs plus the replicates of the center point. Within each part, two factors are arranged in a full two-level design (-1 or 1), while the level of the third factor is set at zero. Therefore, this design requires only 12 runs plus the 3 replicates at the center point, which is substantially less experiments than the number demanded in full factorial or other central composite designs [82,83]. Considering the high and low heat input set of process parameters determined in the preliminary study as window boundaries, it was determined the center point of the Box Behnken Design (**RS**:2200 rpm, **PD**:2.2 mm and **FR**:4 mm/s) and the remaining sets of experiments as listed in Table 4.3.

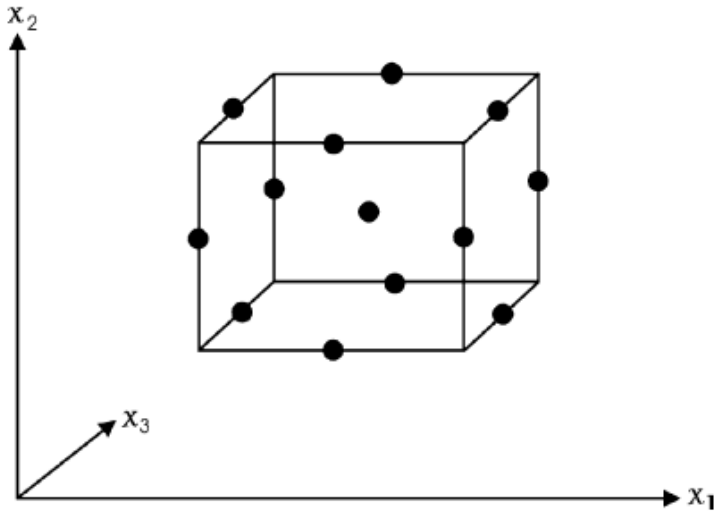

Figure 4.2 - Points representing the experimental runs of a three factor Box Behnken Design [82].

Table 4.3 - Experimental sets of process parameters using Box Behnken Design for mechanical tests evaluation.

Sample	RS [rpm]	PD [mm]	FR [mm/s]	t [s]
1	2200	2.2	4.5	0.97
2	1800	1.8	4.0	0.90
3	2200	2.2	3.5	1.26
4	1800	2.0	4.5	0.89
5	2600	2.0	4.5	0.89
6	2200	2.0	4.0	1.00
7	2200	2.0	4.0	1.00
8	2600	1.8	4.0	0.90
9	2600	2.0	3.5	1.14
10	1800	2.2	4.0	1.1
11	2200	1.8	4.5	0.8
12	1800	2.0	3.5	1.14
13	2200	1.8	3.5	1.03
14	2600	2.2	4.0	1.1
15	2200	2.0	4.0	1.1

4.3.3 Statistical Analysis for Parameters Optimization

Parameters optimization using statistical analysis were made by polynomial regression models, response surface methodology (RSM) [84], and Analysis of Variance (ANOVA) using MiniTab14® software. The responses optimized were maximum shear and peel load (mechanical tests methodologies are presented in the section 4.3.5) which are standardized results tests from D8.2M-2017 standard [13]. Regression models and response surfaces evaluation were assessed by the agreement reliability of the model with experimental results (R^2 values > 60%) and the achievement of a maximum shear and peel load value for at least one significant process parameter at the window range of values. The significance of each parameter was determined in ANOVA tables by p-values

analysis from each coefficient of the regression models considering a confidence level of 94%. This means that a significant coefficient had to present a maximum p-value of 0.06. Complementary mechanical tests were performed to produce new regression models in case of regression models R^2 values were lower than 60%, the maximum shear or peel load were found out the window range values for all process parameters or if all p-values determined in ANOVA tables were higher than 0.06.

Statistical analysis for parameters optimization gives a range of parameters values which maximizes the responses (peel and shear loads) in a predicted range of values according to the regression model. In addition to this, p-values determined in ANOVA tables indicates the significance of each process parameter.

4.3.4 Optimized set confirmation and individual effect analysis

A set of process parameters within the optimized range was chosen to confirm prediction values of peel and shear loads from the regression models and to confirm an optimized set of parameters. This confirmation was made by shear and peel tests using One Factor at a Time methodology (OFAT) [85] which also enables analysis of individual effect of each process parameter.

4.3.5 Mechanical tests

Welds were tested in a Zwick/Roell® testing machine with load capacity of 200 kN in lap-shear and coach peel test configuration, which are presented in Figure 4.3 (a) and (b). The tests were made at room temperature with a displacement rate of 2 mm/min according to specifications from AWS D8.2M-2017 standard [13].

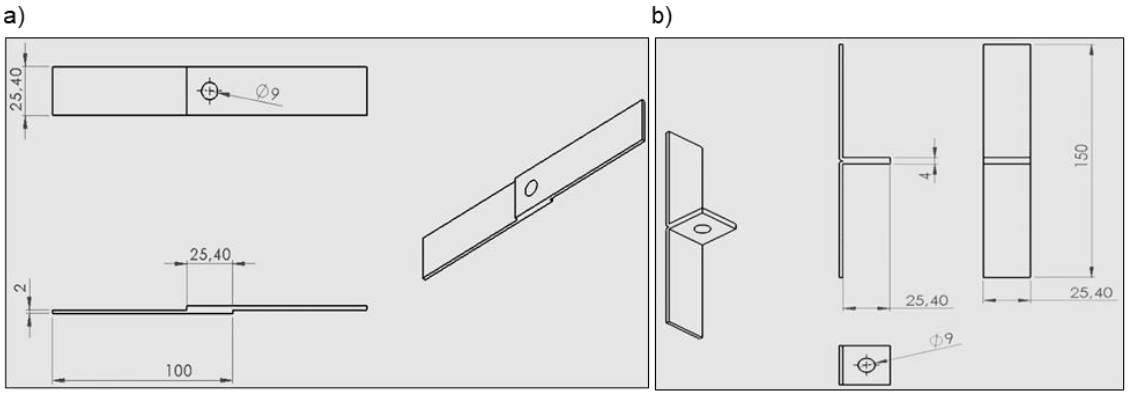

Figure 4.3 - a) Lap Shear test configuration and b) Coach Peel test configuration – dimensions presented in mm.

4.4 Influence of Process Parameters in Macro/Microstructure Features

4.4.1 Macro/Microstructure Characterization

In order to investigate influences of process parameters in macro/microstructure features formation it was carried out macro/microstructure characterization from samples produced by OFAT set of parameters. This procedure aimed to identify the effect of each parameter individually in the 6 features cited in Figure 3.5, namely SZ, TMAZ, HAZ, hook, drop region and Bonding Ligament. Qualitative evaluation was made based in relevant changes in size, shape or position of these elements.

Macro/microstructure characterization was performed in the following steps: cutting; embedding; grinding/polishing and etching. Samples were cut in the cross section near the weld center, embedded with Demotec-20® resin, grinded and polished in a Struers Tegramin® equipment in the following steps:

- Struers Molto® grinding disc of 320 mesh with water for 1 minute;
- Struers Largo® polishing cloth disc with 9 µm diamond suspension lubricant for 3 minutes;
- Struers Dac® polishing cloth disc with 3 µm diamond suspension lubricant for 10 minutes;

- Struers Chem® polishing cloth disc with OP-S 0.04 µm silica suspension lubricant for 3 minutes;

Etching step was made using Barkers Etchant in a Struers LectroPol-5® using 25 V for 180 seconds.

Macro/microstructure analysis were made in a Leica SM IRM® optical microscope equipped with polarized light using Leica Application Suite® software.

4.4.2 Stop action procedure

To further investigate hook tip shape formation, an stop action procedure, which consists in interruptions of the welding process during one of the weld stages (see Figure 3.2) was carried out. In this work, it was produced 9 samples changing plunge depth values and interrupting the weld during plunging, retracting and final stage as described below:

- **PD**=1.9 mm during plunging stage.

- **PD**=1 mm during retracting stage after **PD**=1.9 mm during plunging stage.

- Final stage after **PD**=1.9 mm during plunging stage.

- **PD**=2.1 mm during plunging stage.

- **PD**=1.1 mm during retracting stage after **PD**=2.1 mm during plunging stage.

- Final stage after **PD**=2.1 mm during plunging stage.

- **PD**=2.3 mm during plunging stage.

- **PD**=1.6 mm during retracting stage after **PD**=2.3 mm during plunging stage.

- Final stage after **PD**=2.3 mm during plunging stage.

The samples produced were quenched in water in order to avoid any microstructure change after stopping the process due to thermal effects. Then, microstructure analysis was carried out in the cross sections of those samples applying the same procedure mentioned in section 4.4.1.

4.5 Interrupted mechanical tests

In order to investigate fracture behavior of different RFSSW welds, interrupted mechanical tests were carried out. The general procedure consists of interrupting the test loading as soon as crack propagation process starts. Then, macro/microstructure characterization in the weld cross section aligned to Loading axis is carry out aiming at characterizing the partially propagated crack to better understand the fracture behavior. Since determining the exactly loading point to stop the test is difficult, it was pre-stablished a drop range in Load between 100 and 200 N after the Load curve reached the maximum point as a cut-off load, as illustrated in Figure 4.4.

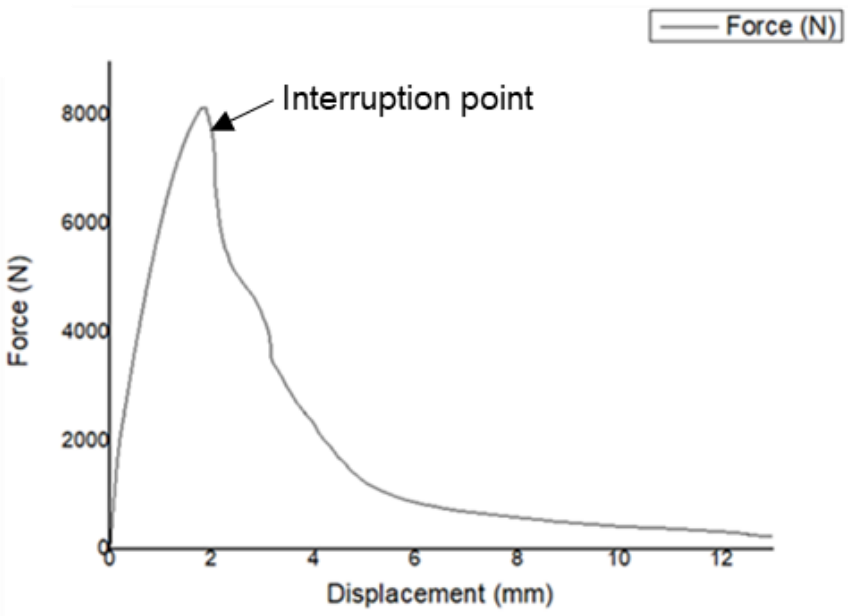

Figure 4.4 - Load versus Displacement curve demonstrating the interruption criteria for fracture analysis.

4.6 Bake Hardening effect on RFSSW welds

As discussed in the introduction and literature review, Bake Hardening treatment is frequently used in automotive industry and reaches temperatures that might have influence in phases distribution and amount of precipitates in precipitation strengthened alloys. Therefore, in order to investigate the effect of

this heat treatment on the RFSSW welded AA6082-T6 alloy, a series of characterization procedures to evaluate the structural changes of the samples before and after Bake Hardening treatment was carried out.

4.6.1 Bake Hardening Treatment

With the purpose of provide comparison between welds with and without Bake Hardening treatment, it was applied Bake Hardening treatment to some samples after welding process (process parameters applied were the optimized condition determined by mechanical test evaluation). This treatment involved heating samples to 180 ºC for 40 minutes followed by air cooling at room temperature. Natural aging before Bake Hardening treatment was limited to 1 hour in post welded samples.

4.6.2 Temperature measurements

Aiming to characterize thermal effects on the alloy's structure, temperature measurements during welding were employed to evaluate the temperature profile along the different position of the weld. 2 K-type thermocouples were used to record the temperature in the SZ and HAZ regions. The thermocouples were inserted in the central region in the bottom plate as illustrated in Figure 4.5.

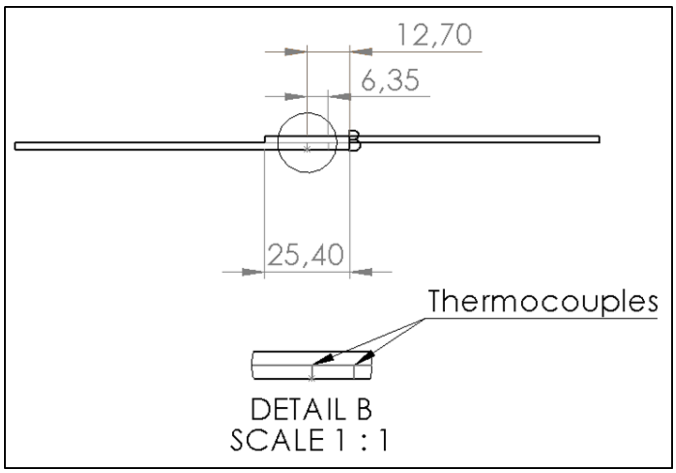

Figure 4.5 - Thermocouples approach applied in Lap Shear configuration to measure temperature profile in SZ and HAZ regions during welding process.

4.6.3 Thermal analysis (DSC)

Thermal analysis using Differential Scanning Calorimetry (DSC) in a DSC 200 F3 Maia were performed in samples removed from the base material region and from the HAZ and SZ regions (same region where the thermocouples were placed). Heat rate and maximum temperature used for the DSC measurements were 10 ºC/s and 500 ºC, respectively. Endothermic and exothermic signals were determined based on literature review about phases precipitation and dissolution in AA6082 applying FSW process and based in Figure 3.18, which presents the 8 possible enthalpic effects determined by DSC analysis from AA6082 discs solutioned and quenched.

4.6.4 Hardness evaluation

Hardness maps were produced in a Zwick/Roell-ZHV® machine in cross sections from welded samples with and without Bake Hardening treatment. Hardness Vickers Tests specifications were: Load test=0.2 kg, indentation time=10s, and minimum distance between indentation 0,25 mm. In each sample, 9 lines with 100 indentations each were made to characterize the whole cross section area as illustrated in Figure 4.6.

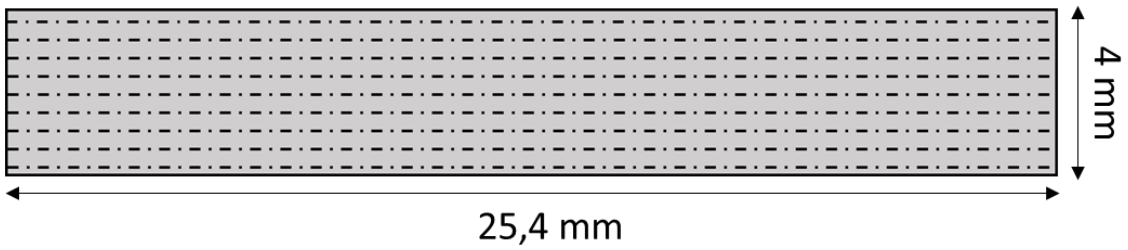

Figure 4.6 - Weld Cross section illustration indicating hardness lines position.

4.6.5 Mechanical behavior

In order to have a preliminary evaluation of the effect of Bake Hardening treatment on the mechanical properties, shear mechanical tests in welded samples with and without Bake Hardening treatment were performed.

Correlations and comparisons of shear strength, fracture behavior and microstructure characteristics between these two conditions were assessed in this work. These correlations and comparisons were based on the results from process parameters optimization, fracture analysis, temperature measurements, hardness maps and DSC results.

4.7 Fatigue properties evaluation

4.7.1 Fatigue tests

Fatigue tests were carried out in room temperature in a servo hydraulic machine Schenck Instron. Samples configuration were similar to the configuration presented in Figure 4.3 (a). The load ratio applied ($R=L_{min}/L_{max}$) was R=0.1, the frequency was 20 Hz and load levels evaluated were between 4382–657 N (50%-7.5% of the maximum load obtained in monotonic shear mechanical test). Three samples for each load level were tested with a stopping criteria of $5x10^6$ cycles.

Based on industry applications, it was decided to apply Bake Hardening treatment in all samples before fatigue tests. The heat treatment sequence followed the same steps described in section 4.6.1.

4.7.2 L-N curves determination and Weibull statistical analysis

L-N curves were obtained through Weibull statistical analysis, which is an appropriate methodology to assess fatigue behavior in Load levels near to the fatigue limit [18,35,80]. A two-parameter Weibull distribution was applied to analyze the probability aspects of the fatigue results. The probability density function $f(x)$ for a two-parameters Weibull distribution is defined as:

$$f(x) = \beta \frac{x^{\beta-1}}{\alpha^{\beta}} \exp\left[-\left(\frac{x}{\alpha}\right)^{\beta}\right] \qquad \alpha \geq 0, \beta \geq 0 \qquad (4.1)$$

Where α is the scale parameter or characteristic life, which is associated to the failure probability in 63.2 % and β is the shape parameter or Weibull slope, which determines the shape of the distribution.

A cumulative density function $F(x)$ is obtained from the integration of the Equation 4.1, which results in the Equation 4.2.

$$F(x) = \int_{-\infty}^{x} f(z)dz = 1 - \exp\left[-\left(\frac{x}{\alpha}\right)^{\beta}\right] \qquad (4.2)$$

Since $F(x)$ cannot be obtained directly from Equation 4.2 (the whole population is never tested) an empirical estimator (Bernard's Median Rank-MR) was used in this work to represent $F(x)$. This estimator is presented in Equation 4.3.

$$F(x) \cong MR = \frac{i - 0.3}{n - 0.4} \qquad (4.3)$$

where i is the failure serial number and n is the total number of samples.

In order to determine Weibull parameters (α, β), it was applied $\ln$ function twice in Equation 4.2 resulting in the Equation 4.4. From linear plots of $\ln \ln \left[\frac{1}{1-F(x)}\right]$ vs $\ln(x)$ was obtained a slope coefficient (β) and a linear coefficient (-$\beta \ln(\alpha)$), which allows α and β determination.

$$\ln \ln \left[\frac{1}{1 - F(x)}\right] = \beta \ln x - \beta \ln \alpha \qquad (4.4)$$

Based on α and β determination, the Weibull mean life or mean time to failure (MTTF) was calculated using Equation 4.5, which represents the expected life for a given load amplitude for fatigue testing.

$$MTTF = \propto \Gamma\left(1 + \frac{1}{\beta}\right) \qquad (4.5)$$

where $\Gamma()$ is the gamma function [86].

From α and β values, it is also possible to calculate fatigue life of load levels for different reliability levels using the Equation 4.6.

$$N_{R_x} = \alpha(-\ln(R_x))^{-\frac{1}{\beta}} \qquad (4.6)$$

where N_{R_x} is the value of fatigue life for a reliability level (R_x%). Therefore, it is possible obtain L-N curves for different reliability levels. In this work, it was plotted L-N curves with reliability levels of 10%, 36.8%, 50% e 99%.

The fit of the data set to the two-parameter Weibull distribution was visually assessed using Weibull plots using Equations 4.3 and 4.4. This plot indicates whether the data follow a Weibull distribution or not, by demonstrating the linearity of the arranged points.

Fatigue properties were evaluated in high and low load levels analyzing fracture behavior and fatigue life. Fatigue limits of the L-N curves were determined considering the Load level that reached a fatigue life of 1000000 cycles, and it was compared to previous works evaluations of fatigue properties in RFSSW.

4.7.3 Fracture surface analysis

Fatigue fracture surface analysis were carried out to have a preliminary investigation about crack initiation and propagation mechanisms. The main characteristics of fatigue fracture surface features were analyzed by Scanning Electron Microscopy (SEM) using Secondary Electron (SE) emission signal.

5 RESULTS AND DISCUSSIONS

5.1 Process Parameters Optimization

5.1.1 Shear strength optimization

Equation 5.1 represents shear strength model obtained in MiniTab software using a polynomial regression of the results from Box Behnken Design experiments presented in Table A (see supplementary section). Shear Load Model presented good reliability in fitting experimental results since R^2=81.1%.

Shear Load (N) = -3.5328***RS** + 80156.2062***PD** + 23322.0975***FR** + 0.0008***RS²** - 9972.7187***PD**^{2} - 1867.9550***FR**^{2} - 3.518***RS***PD** + 2.0109***RS***FR** - 6891.4250***PD***FR** (5.1)

Figure 5.1 (a), (c), (e) and (g) show the response surfaces and contour plots obtained by Equation 5.1 through the analysis of the process parameters effects. Initially, the surfaces profiles resulted in optimized process parameters values in regions out of the initial experimental range. According to these results, the maximum shear load would have been reached in sets with Plunge Depths higher than 2.2 mm, Rotational Speed values higher than 2600 rpm and Feeding Rate values lower than 3.5 mm/s. In order to reach the optimized set of process parameters values and based on these initial trends, further experiments were carried out expanding the range of values analyzed (complementary data of these experiments are present on Table B of the supplementary section). Therefore, it was determined a new regression model expressed by Equation 5.2.

Shear Load (N) = 3.2250***RS** + 94930.4137***PD** + 16677.1428***FR** - 0.0006***RS²** - 18566.5400***PD²** - 1791.4917***FR²** - 1.9967***RS***PD** + 1.1322***RS***FR** -2878.1947***PD***FR** (5.2)

From Equation 5.2 new response surfaces and contour plots were obtained as shown in Figure 5.1 (b), (d), (f) and (h). Although Shear Model reliability was slightly reduced (R^2=76.9%) with the new data, all process parameters presented an optimized value within the window. According to the response surfaces and model predictions, the optimized set of process

parameters gives a maximum shear load higher than 8 kN, which is demonstrated in Figure 5.1 (h). This is achieved applying plunge depth values between **PD:** 2.05-2.20 mm, rotational speed values between **RS:** 2500-3000 rpm and feeding rate values between **FR:** 3.5-4.2 mm/s.

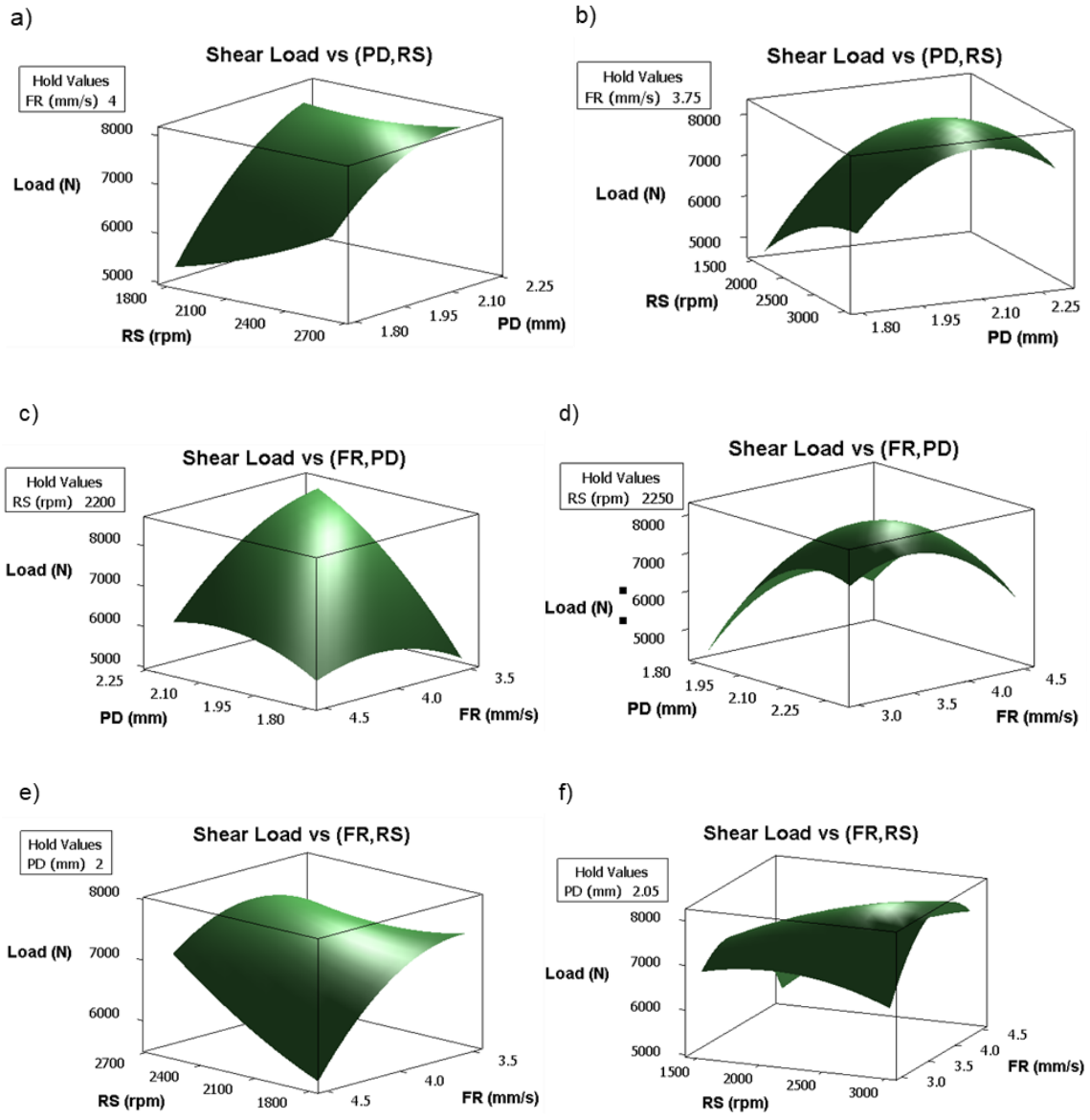

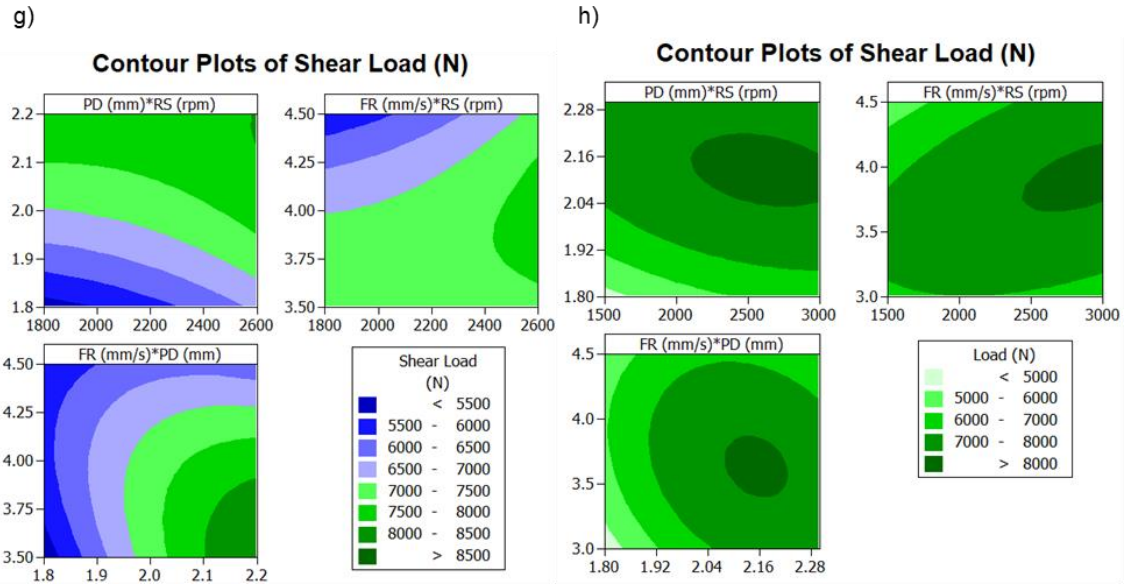

Figure 5.1 - Response surfaces and contour plots obtained by Box Behnken Design experiments changing process parameters: a) PDxRS, c) FRxPD, e) FRxRS and g) contour plots. Response surfaces and contour plots obtained after complementary experiments; b) PDxRS, d) FRxPD, f) FRxRS and h) contour plots.

5.1.2 ANOVA from shear model

According to ANOVA results presented in Table 5.1, considering a confidence level of 94%, the linear and quadratic terms of plunge depth, the linear term of rotational speed and the quadratic coefficient of feeding rate showed a significant effect on shear strength, since for these terms the p-values were lower than 0.06. These results demonstrate that all process parameters have a significant effect on the shear strength within the range of the studied values.

Table 5.1 - Analysis of Variance (ANOVA) for shear model.

ANOVA – Shear model				
Term	**Coef**	**SE coef**	**T**	**p-value**
Const	**7906.99**	**165.7**	**47.713**	**0**

PD	**880.46**	**147.9**	**5.954**	**0**
RS	**455.46**	**234.9**	**1.939**	**0.06**
FR	**-83.88**	**178.7**	**-0.469**	**0.642**
PD*PD	**-1160.41**	**241.9**	**-4.797**	**0**
RS*RS	**-346.3**	**238.8**	**-1.45**	**0.156**
FR*FR	**-1007.71**	**261.5**	**-3.853**	**0**
PD*RS	**-374.38**	**339.9**	**-1.101**	**0.278**
PD*FR	**-539.66**	**323.4**	**-1.669**	**0.104**
RS*FR	**636.88**	**559.8**	**1.138**	**0.263**

5.1.3 Peel Strength optimization

Based on the process parameters optimization results from shear strength, it was determined a new Box Behnken set of experiments including the complementary range of values analyzed. This new set is shown in Table 5.2.

Table 5.2 - Box Behnken Design of experiment for Peel Strength optimization.

Sample	RS [rpm]	PD [mm]	FR [mm/s]	t [s]
1	2300	2.3	3.9	1.18
2	2700	2.3	3.3	1.39
3	3100	1.9	3.9	0.97
4	2700	2.1	3.9	1.08
5	3100	2.3	3.9	1.18
6	2700	1.9	3.3	1.15
7	2700	2.1	3.9	1.08
8	2700	2.1	3.9	1.08
9	2300	1.9	3.9	0.97
10	3100	2.1	3.3	1.27
11	2700	2.3	4.5	1.02

12	2300	2.1	3.3	1.27
13	3100	2.1	4.5	0.93
14	2300	2.1	4.5	0.93
15	2700	1.9	4.5	0.84

Equation 5.3 shows peel strength model obtained in MiniTab software using a polynomial regression of the results from Box Behnken design experiments presented in Table C. Peel Load Model presented good reliability in fitting experimental results since R^2=91.2%.

Peel Load (N) = 0.6048*__RS__ + 39566.4688*__PD__ - 1666.6354*__FR__ - 0.0002*__RS__^{2} - 8998.7500*__PD__^{2} + 243.0556*__FR__^{2} - 0.3072*__RS__*__PD__ + 0.2159*__RS__*__FR__ -362.9167*__PD__*__FR__ (5.3)

Figure 5.2 (a), (b), (c) and (d) show the response surfaces and contour plots obtained by Equation 5.3 through the analysis of the process parameters effects. The response surfaces and contour plots indicate that the maximum peel strength (higher than 1.2 kN) is reached in values of plunge depth between **PD**: 2.00–2.16 mm. Furthermore, the effect of feeding rate and rotational speed on the peel strength is relatively lower when compared to the plunge depth effect. This was concluded based on the difference between the peel loads observed by changing the feeding rate and rotational speed values, which was comprised in an interval of just 100 N as demonstrated in Figure 5.2 (d).

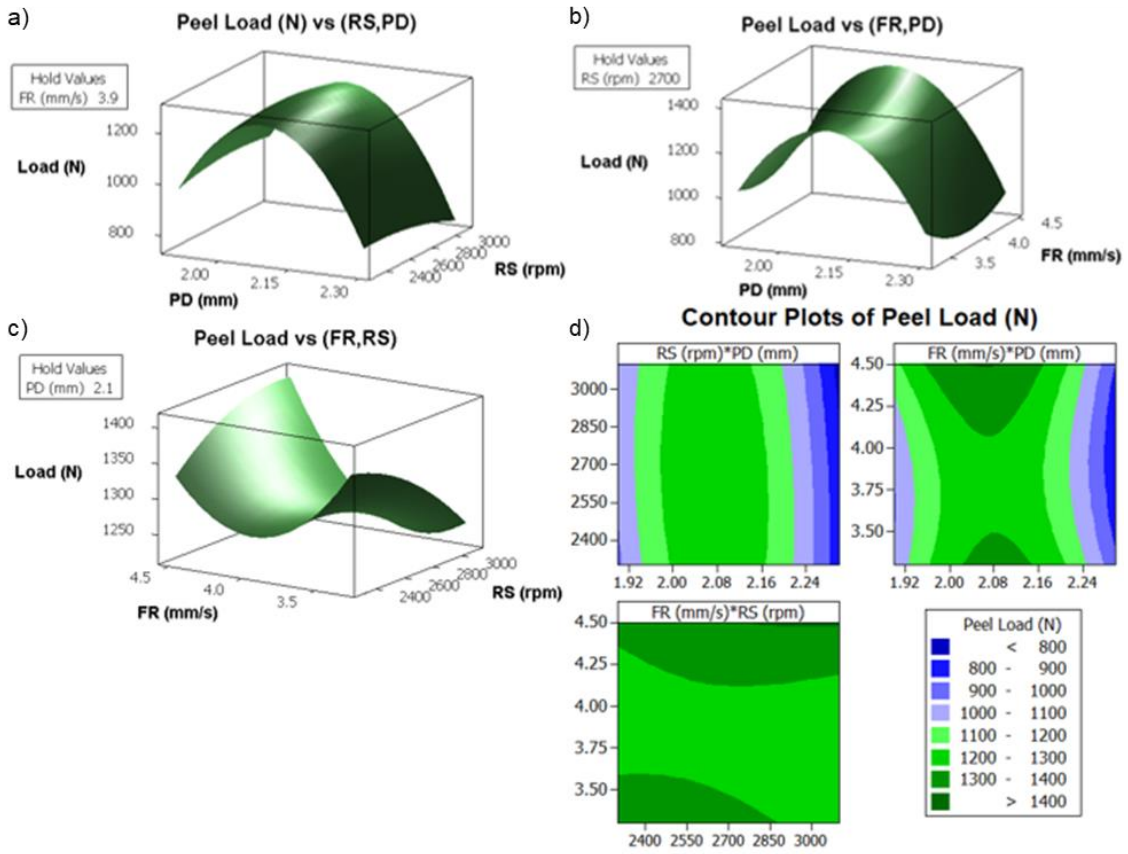

Figure 5.2 - Peel Strength Response surfaces and contour plots obtained by Box Behnken Design experiments changing process parameters: a) PDxRS, b) FRxPD, c) FRxRS and d) contour plots.

5.1.4 ANOVA from Peel model

According to the ANOVA results presented in Table 5.3, considering a confidence level of 94%, the terms of the model that show significant effect on peel strength are the linear and quadratic coefficients of plunge depth, since for these two terms the p-values were lower than 0.06. These results demonstrate that only plunge depth parameter has a significant effect on peel strength for the range of values studied.

Table 5.3 - Analysis of Variance (ANOVA) for peel model.

ANOVA CA				
Term	**Coef**	**SE coef**	**T**	**p-value**
Const	**1276.9**	**63.58**	**20.084**	**0**
PD	**-94.61**	**38.93**	**-2.43**	**0.059**
RS	**-13.02**	**38.93**	**-0.335**	**0.752**
FR	**30.06**	**38.93**	**0.772**	**0.475**
PD*PD	**-359.95**	**57.31**	**-6.281**	**0.002**
RS*RS	**-24.72**	**57.31**	**-0.431**	**0.684**
FR*FR	**87.5**	**57.31**	**1.527**	**0.187**
PD*RS	**-24.57**	**55.06**	**-0.446**	**0.674**
PD*FR	**-43.55**	**55.06**	**-0.791**	**0.465**
RS*FR	**51.82**	**55.06**	**0.941**	**0.39**

Comparing the results from shear and peel strength optimization it was provided information about the optimized set of process parameters. Plunge depth values between 2.05 and 2.15 mm optimize both peel and shear strength. Rotational Speed between 2500-3000 rpm and Feeding Rate between 3.5-4.2 mm/s optimize shear strength. P-values from ANOVA showed that all studied processing parameters are significant for shear strength, but only plunge depth is a relevant parameter for peel strength, considering a confidence level of 94%. The predicted optimized values for shear and peel strength are higher than 8 and 1.2 kN, respectively.

Based on such analysis, one possible set of optimized process parameters is (**PD**=2.1 mm, **RS**=2900rpm and **FR**=3.9mm/s), which according to the models will result in shear and peel loads higher than 8 and 1.2 kN, respectively. Therefore, this set of process parameters was employed to confirm this finding

and to perform individual effect analysis using the One Factor at a Time methodology.

5.1.5 One Factor at a Time (OFAT)

Analyzing each single process parameter effect separately, using OFAT methodology (considering the following set of process parameters: **PD**=2.1 mm, **RS**=2900rpm and **FR**=3.9mm/s), the graphs of Figure 5.3 (a), (b) and (c) for shear strength were build (data available in Table D). Figure 5.3 (a) shows the effect of Feeding Rate on the Shear strength. The maximum Shear Load achieved (8.4±0.3 kN) were determined between 3.4 and 3.9 mm/s, which is in agreement with predictions made by shear strength model, that predicted optimized values of feeding rate between 3.5-4.2 mm/s, resulting in shear loads higher than 8 kN. Figure 5.3 (b) shows the effect of plunge depth on the shear strength. The maximum shear load reached (8.3±0.2 kN) was obtained with 2.1 mm of plunge depth, also in accordance with model predictions, which stablished shear loads higher than 8 kN to plunge depth values between 2.05 and 2.15 mm. Figure 5.3 (c) shows the effect of rotational speed on the shear strength. It is observed that for values higher than 2500 rpm of rotational speed, shear loads reached more than 8 kN as predicted by the shear load model.

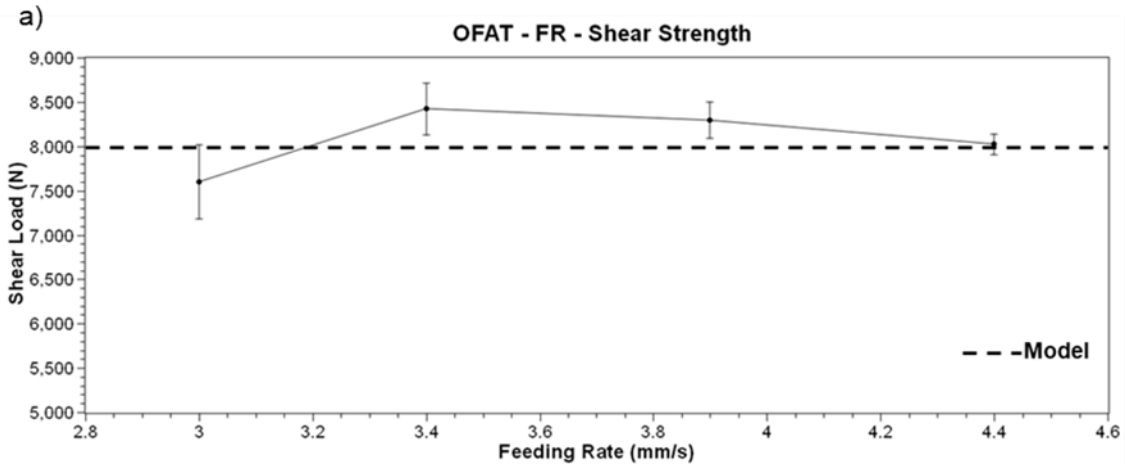

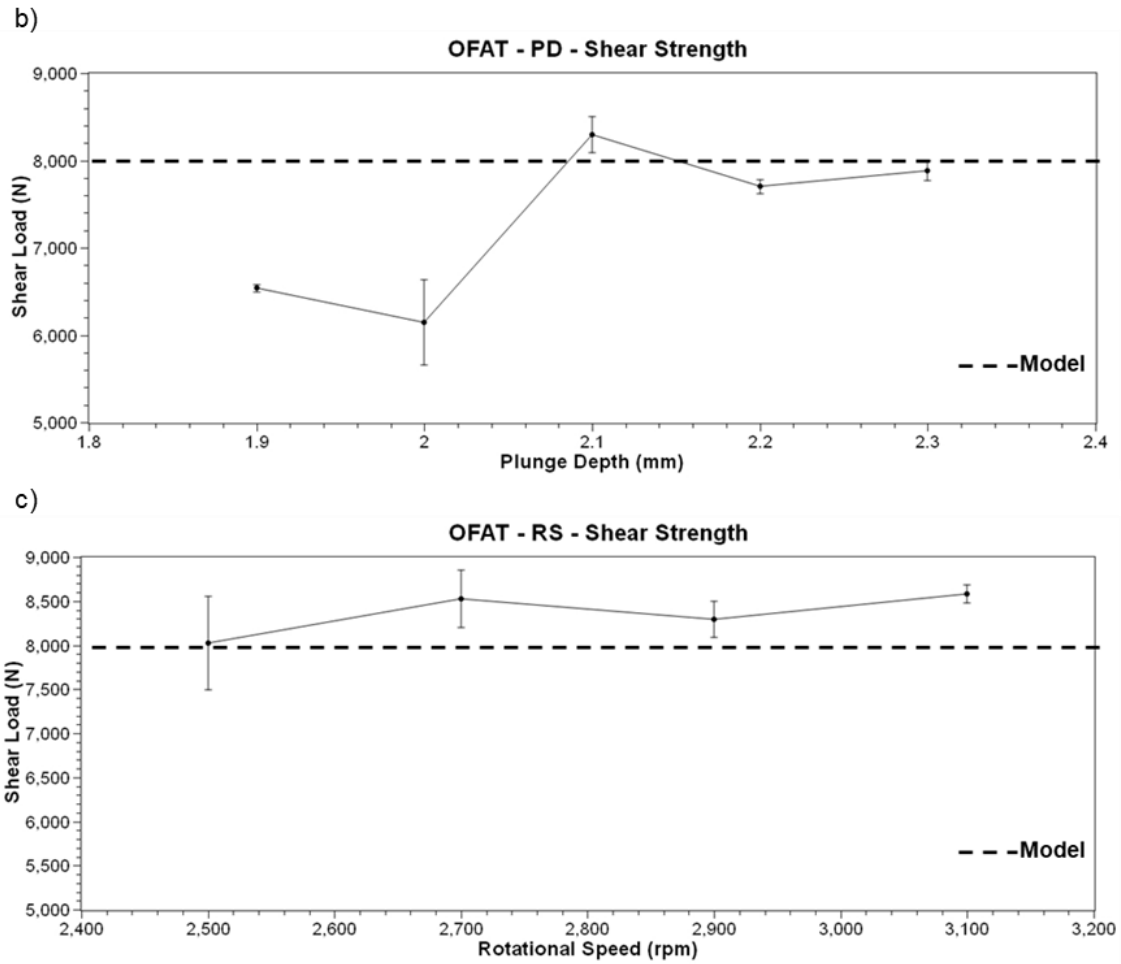

Figure 5.3 - Shear strength OFAT results for a) Feeding Rate, b) Plunge Depth and c) Rotational Speed.

Figure 5.4 (a), (b) and (c) show the results of the OFAT for peel strength analysis (data available in Table E). Figure 5.4 (a) shows the influence of Feeding rate on the Peel strength. Peel loads higher than 1.2 kN were obtained for values of feeding rate lower than 3.9 mm/s, but the difference between the average load of these values was only 100 N, which, considering the standard deviation, has low significance. Figure 5.4 (b) presents the effect of plunge depth on the peel strength. It is observed that the maximum level of peel load (1.3±0.1 kN) was reached for 2.1 mm of plunge depth, also in agreement with model's predictions. Nonetheless, Figure 5.4 (c) illustrates the effect of the rotational speed on the peel strength. Maximum value of peel loads was attained for rotational speeds higher than 2700 rpm, but the difference observed in peel loads was not

significant (100 N) considering standard deviation, as also indicated by the models.

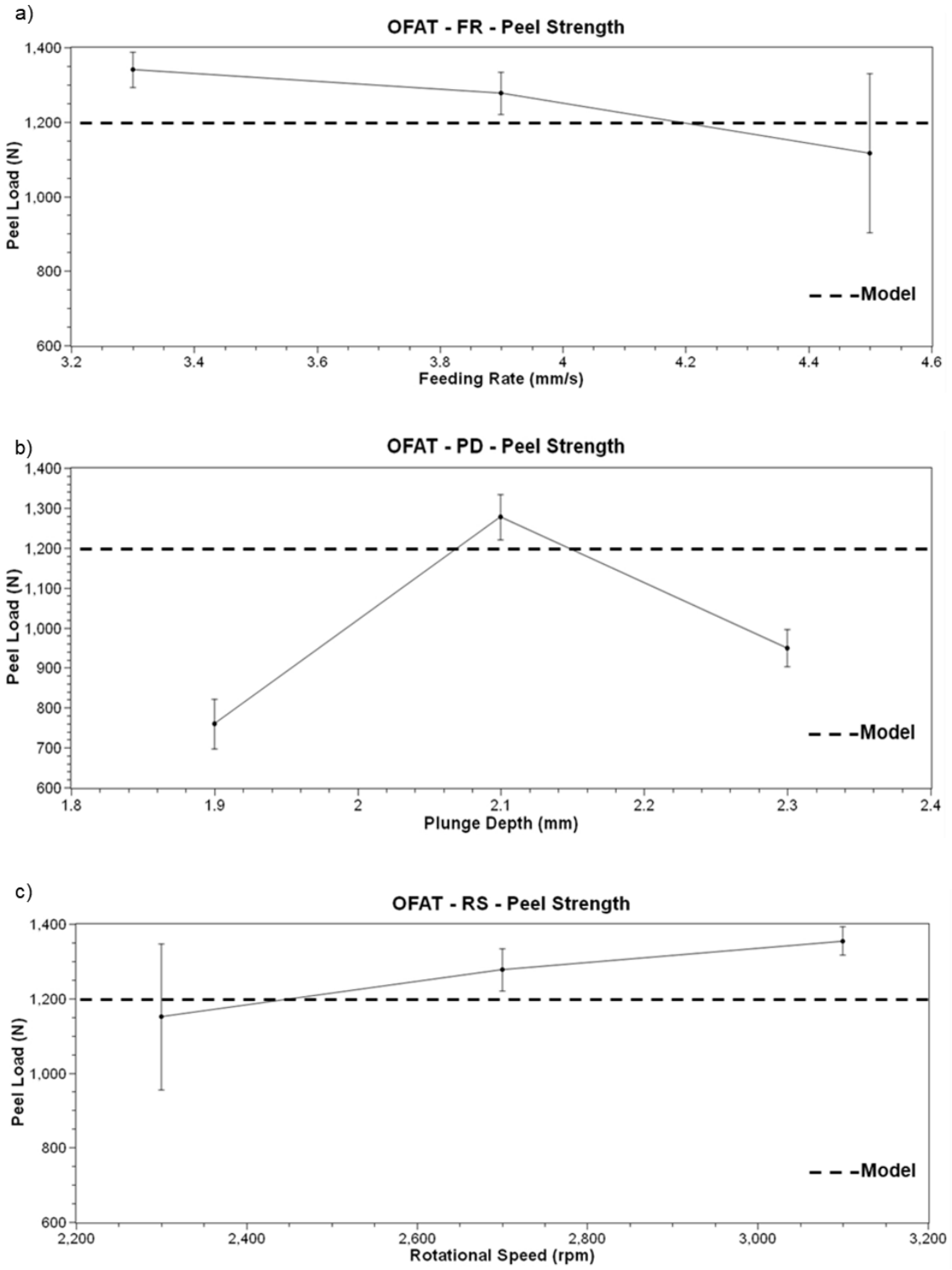

Figure 5.4 - Peel strength OFAT results for a) Feeding Rate, b) Plunge Depth and c) Rotational Speed.

Some processing parameters values as 3100 rpm of rotational speed and 4.5 mm/s of feeding rate have showed interesting shear or peel strength, but these results were close to the mechanical limits of the welding machine (RS=3300 rpm and FR=5 mm/s), therefore these conditions were excluded of the optimization study. Furthermore, in order to increase efficiency and reducing the welding time, it was decided to use the highest feeding rate possible which maintained levels of peel and shear load higher than those predicted by the models. Based on these analysis, the optimized set of process parameters found were: **PD**:2.1mm, **FR**:3.9 mm/s and **RS**:2700 rpm, which resulted in an average shear and peel load of 8.5±0.3 kN and 1.3±0.1 kN respectively. Additionally, the welding time obtained in this condition was 1.08±0.01 s.

The Shear Load strength obtained in this work is similar to the values found by Wang [14] and only 5.5% lower than the value reported by Marschner [6]. But it is worth noting that these values are considerably higher than the requirements for aerospace specification (4.8 kN), which is more rigid than automotive standards [28]. However, the welds of this work were performed in only 1.08 s when the optimized parameters set was employed. This result is 40% faster than Marschners results which was the more efficient process parameters set reported up to date. This welding time efficiency is compatible with automotive industry demands [5].

Peel Load results are less frequently reported in literature for RFSSW welds. However, considering a previous evaluation regarding standard requirements and comparison with other techniques currently applied in automotive industry, the results obtained in this work (1.3±0.1 kN) fulfill the standard requirements, but presents lower values than those reported for RSW and SPR techniques (1.8-2 kN) [5,13,87].

Regarding individual parameters effect, it was observed similar trends than those discussed in literature review (section 3.3). But our results, using ANOVA and OFAT, were conclusive to show that the plunge depth has more influence in weld strength than the other parameters, as suggested by several authors [9,16,18,20,25,26,41–43].

5.2 Influence of Process Parameters on Macro/Microstructure Features

5.2.1 Macro/Microstructure Characterization

Macrostructure characterization of the OFAT samples for different Feeding Rate and Rotational Speed values are presented in Figure 5.5 (a), (b), (c) and Figure 5.6 (a), (b), (c). There are only small differences in the size and shape of hook, Bonding Ligament, drop region, HAZ, TMAZ and SZ between all the samples.

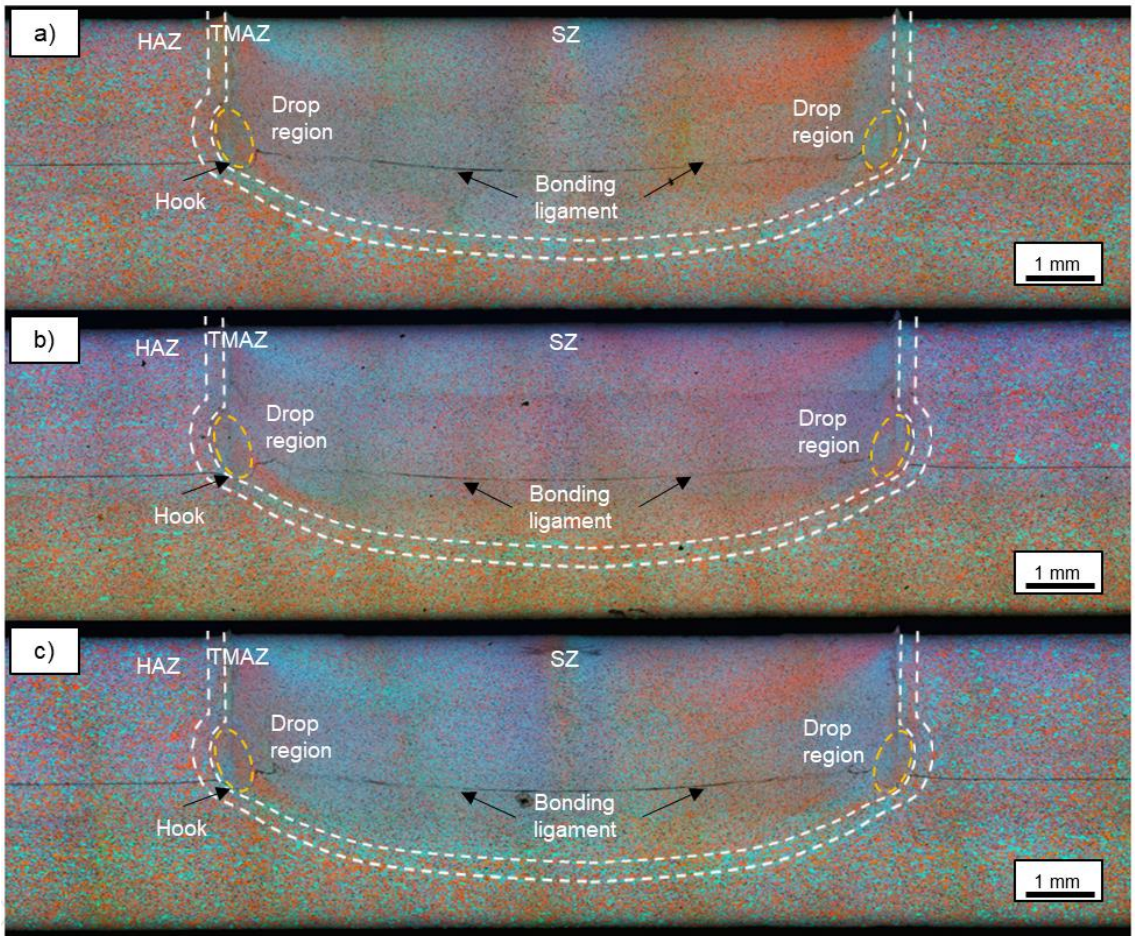

Figure 5.5 - Macrostructure of the samples produced with PD=2.1mm, RS=2900rpm and feeding of a) FR=3.3mm/s, b) FR=3.9mm/s and c) FR=4.5mm/s.

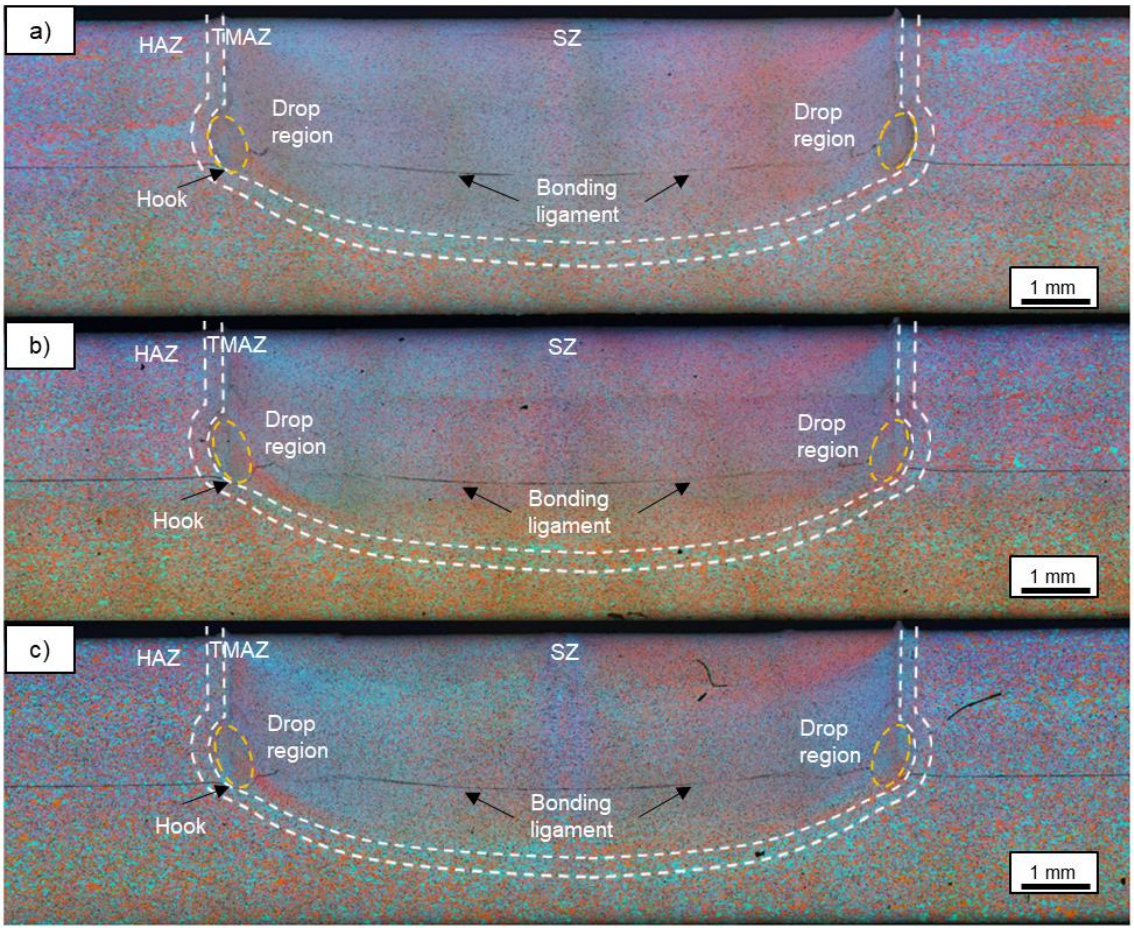

Figure 5.6 - Macrostructure of the samples produced with PD=2.1mm, FR=3.9mm/s and Rotational Speed of a) RS=2500rpm, b) RS=2900rpm and c) RS=3100rpm.

On the other hand, for different conditions of plunge depth significant changes in hook tip shape, Bonding Ligament and drop region features is observed, as shown in Figure 5.7 (a), (b) and (c). Figure 5.7 (a) shows the weld macrostructure of the sample produced with the lower value of plunge depth. In this sample a flat hook tip connected with the Bonding Ligament is observed. Figure 5.7 (b) shows the weld macrostructure for the sample produced with intermediate value of plunge depth, where a hook tip pointing down connected with Bonding Ligament is observed. Finally, Figure 5.7 (c) presents the weld macrostructure for the sample produced using higher plunge depth value and a hook tip pointing up with no connection with the Bonding Ligament can be seen. Regarding Drop region changes for these three conditions, it is observed that

drop region position is affected by plunge depth. This is expected since the drop region is formed underneath the sleeve position at the deepest penetration during the welding process. For the remaining weld features including SZ, HAZ, TMAZ size and shape, only small differences are noted. For instance, SZ area increases with higher plunge depths. Then, deeper analysis regarding these changes were not held in this work.

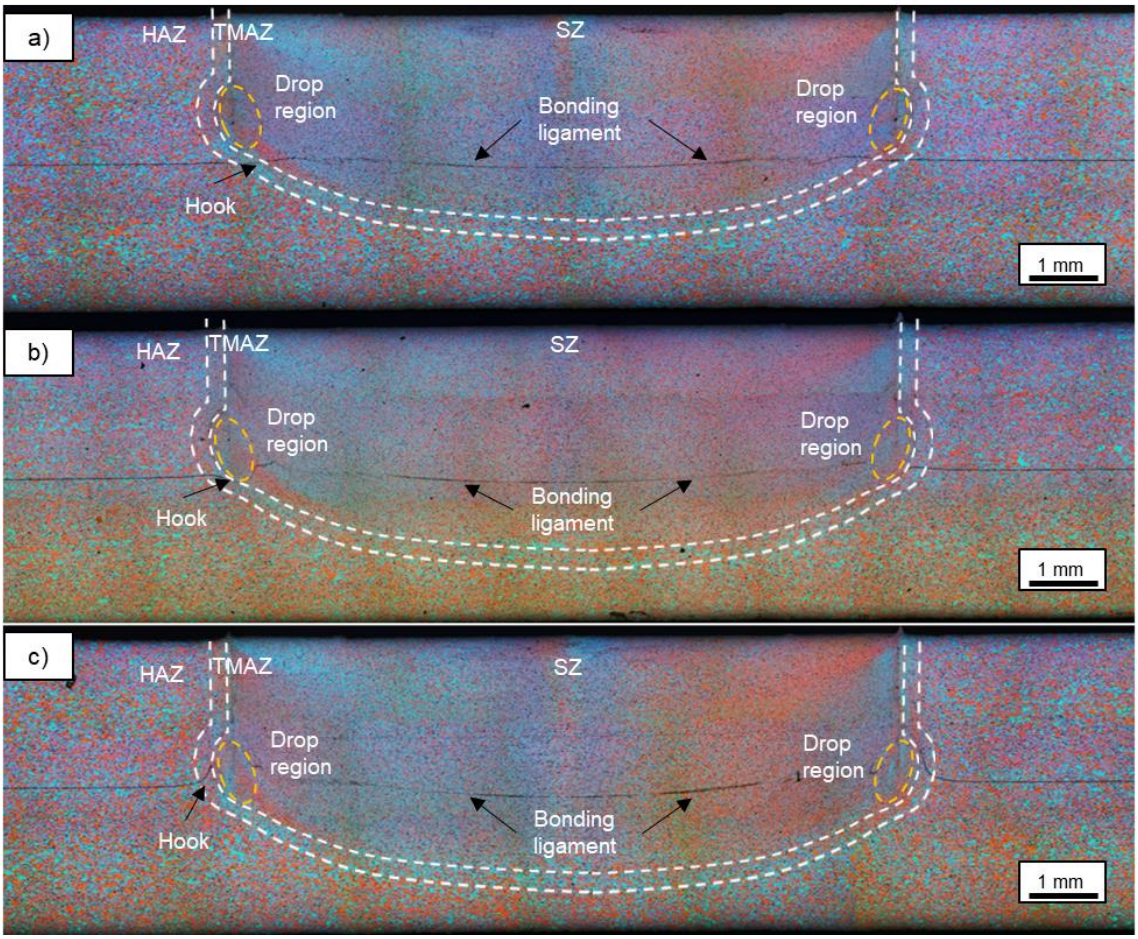

Figure 5.7 - Macrostructure of the samples produced with FR=3.9mm/s, RS=2900rpm and Plunge Depth of a) PD=1.9mm, b) PD=2.1mm and c) PD=2.3mm.

For a better observation, Figure 5.8 (a), (b) and (c) present the hook tip region with higher magnification showing the differences in the hook tip shape and Bonding Ligament for these three conditions.

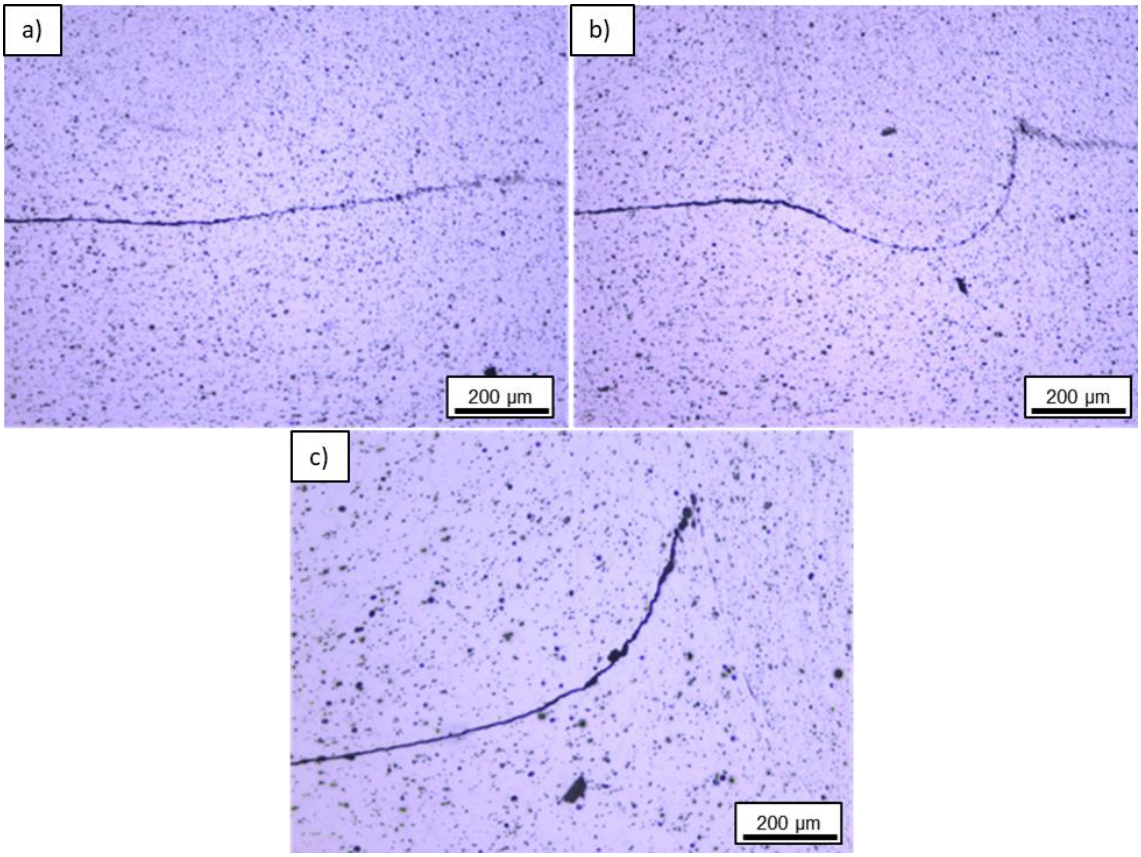

Figure 5.8 - Hook tip shapes of the welds produced with the same RS=2900 rpm, FR=3.9 mm/s and different Plunge Depth values. a) Flat hook (PD=1.9mm), b) hook tip pointing down (PD=2.1mm) and c) hook tip pointing up (PD=2.3mm).

5.2.2 Hook tip shape formation

In this work, the hook formation was studied using the stop action procedure. Figure 5.9, Figure 5.10 and Figure 5.11 show the sleeve path microstructures from each stage of the welding process (plunging, retracting and final stage) for the three process conditions studied here.

Figure 5.9 (a), (b) and (c) illustrate how the flat hook tip is formed. During plunging stage, a material flow around the sleeve (feature 1) is formed and pulls the interface between the two plates (remaining oxide layer) as indicated in Figure 5.9 (a). During retracting stage (Figure 5.9 (b)), the material flow around the sleeve moves away from the interface and due to drop region formation (feature 2), the interface is pushed back to its original position. Therefore, in the last stage,

Drop region is completely formed above the interface resulting in the flat hook tip formation as showed in Figure 5.9 (c).

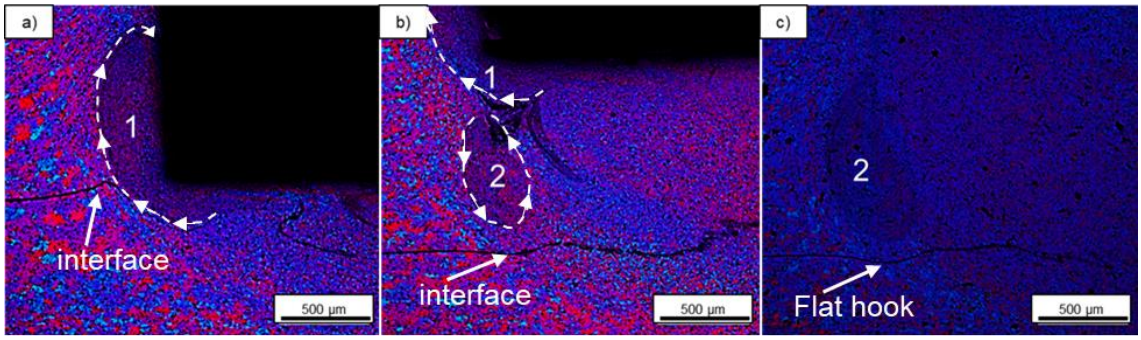

Figure 5.9 - Flat hook formation - Microstructures of hook tip region from stop action samples: a) PD=1.9 mm during plunging stage, b) PD=1 mm during retracting stage, and c) final stage.

Figure 5.10 (a), (b) and (c) illustrate the formation of the hook tip pointing down. During plunging stage, material flow around the sleeve (feature 1) presented a higher interaction with the interface between the two plates than in flat hook formation (compare the curved interfaces in Figure 5.9 (a) and Figure 5.10 (a)). During the retracting stage Drop region (feature 2) it is formed pushing the interface below its original position (Figure 5.10 (b)). Therefore, in the last stage the Drop region is completely formed resulting in the hook tip pointing down formation as seen in Figure 5.10 (c).

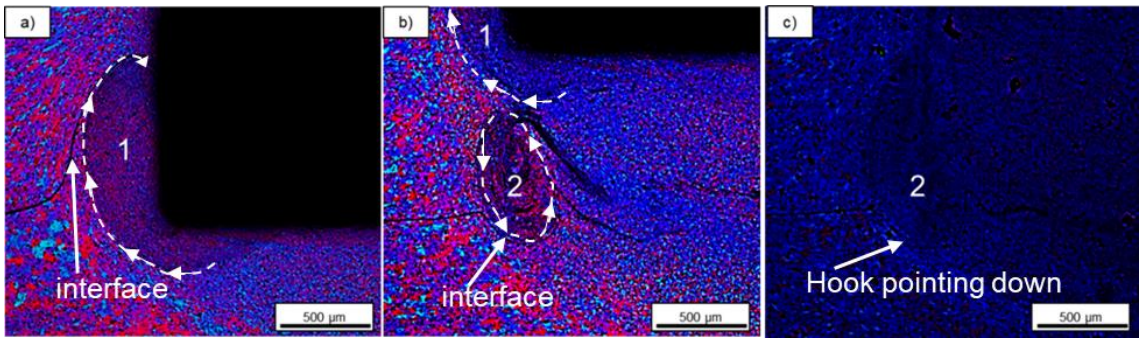

Figure 5.10 - Hook tip shape pointing down formation - Microstructures of hook tip region from stop action samples: a) PD=2.1 mm during plunging stage, b) PD=1.1 mm during retracting stage and c) final stage.

Figure 5.11 (a), (b) and (c) illustrate the formation of the Hook tip pointing up. During plunging stage, it is observed again a higher interaction of the material flow around the sleeve (feature 1) with the interface between the plates (compare the curved interfaces in Figure 5.9 (a), Figure 5.10 (a) and Figure 5.11 (a)). However, differently from the two previous hook tip formation, during retraction stage, Drop region is formed below the interface, while the material flow around the sleeve still pulls the interface in the opposite direction as indicated in Figure 5.11 (b). Therefore, after the material flow around the sleeve moves away from the interface, the Drop region is almost completely formed, which avoids the interface being pushed down, resulting in the hook tip pointing up (Figure 5.11 (c)).

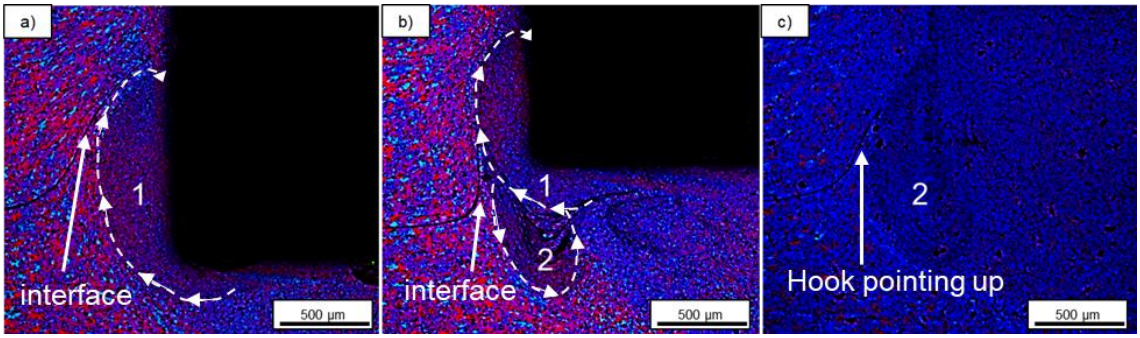

Figure 5.11 - Hook tip shape pointing up formation - Microstructures of hook tip region from stop action samples: a) PD=2.3 mm during plunging stage, b) PD=1.6 mm during retracting stage and c) final stage.

Summarizing this topic, it was observed from macrostructure characterization of the OFAT samples that Feeding Rate and Rotational Speed have only small influence on the hook tip shape. Stop action results showed that Plunge Depth controls the hook tip shape throughout formation/position of material flow around the sleeve and Drop region. Although some works have reported the influence of other parameters in hook height [6,18,24–26,30], none of them have reported their influence in hook tip shape, which is in agreement with results from this work. The understanding of the hook tip shape formation is important to control the quality of RFSSW welds and to improve this welding technique. For example, the tool design could be changed to have an effect on material flow and Drop region features and then controlling the hook tip shape.

5.3 Fracture analysis of static mechanical tests

5.3.1 Fracture modes

Similarly to what was reported in other works [6,18,25,35], two different fracture modes during static mechanical tests was found in this work: (i) Through the Weld (TW) and (ii) Pull-Out (PO) fracture. Figure 5.12 (a) shows a sample which presented TW fracture. As explained in section 3.3.2, TW fracture occurs along the interface of the welded sheets. Indications of brittle behavior was linked to this type of fracture due to the sharp drop of measured load seen during the test (see Figure 5.13 (a)). Figure 5.12 (b) shows an example of PO fractured sample. The main characteristic of this fracture is the circumferential path along the welded spot, pulling out the welded region. Apparently, this fracture mode has a more ductile behavior as can be seen in the Force vs Displacement curve presented in Figure 5.13 (b).

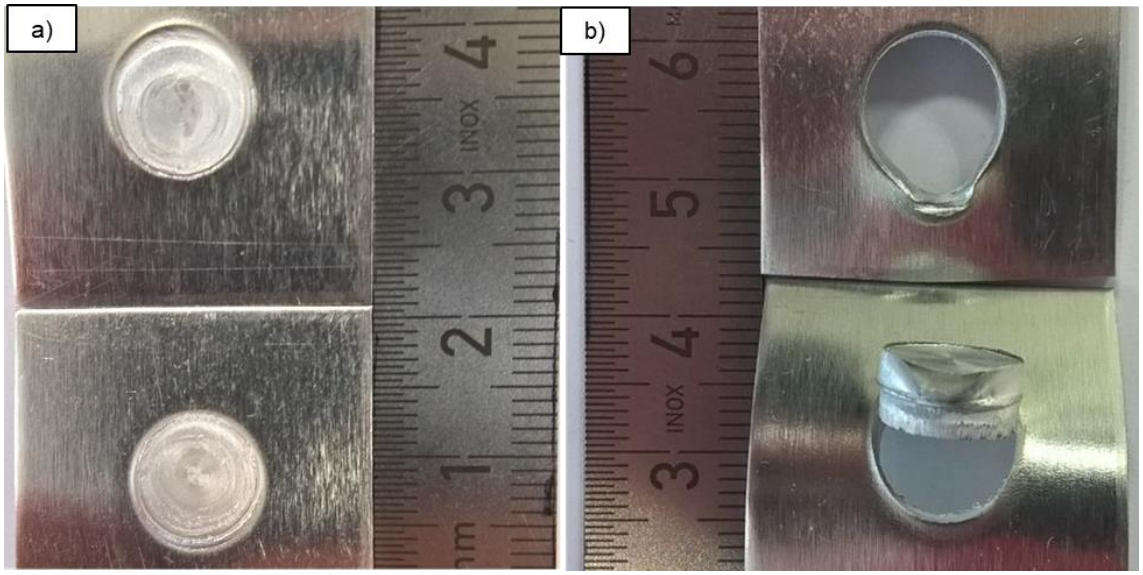

Figure 5.12 - Fracture modes observed during Static Mechanical tests. a) Through weld fracture (TW) b) Pull-Out fracture (PO).

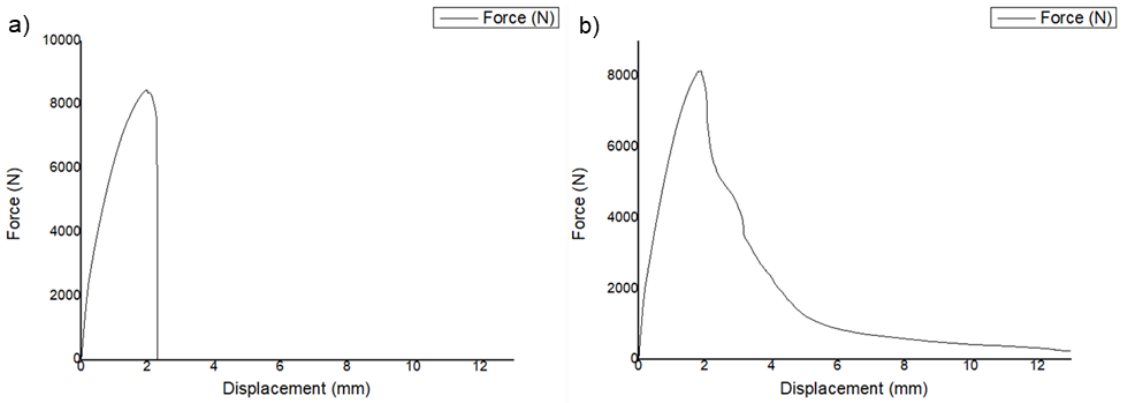

Figure 5.13 - Force vs Displacement curve tests from samples with a) TW fracture and b) PO fracture.

5.3.2 Failure Mode Transition

Aiming at finding a clear trend between process parameters, weld strength and fracture mode, graphs correlating these features were plotted using data from the process parameter optimization results. Figure 5.14 (a), (b), (c) and Figure 5.15 (a), (b), (c) correlate the results of shear and peel strength regarding each process parameter applied and the fracture behavior presented. No clear trend between fracture mode and strength is identified for Rotational Speed and Feeding Rate as shown in Figure 5.14 (a), (b) and Figure 5.15 (a), (b). However, a clear correlation between the Plunge Depth, strength and fracture mode was found. A failure mode transition was observed in Figure 5.14 (c) and Figure 5.15 (c). For both mechanical test procedures (Peel and Shear tests), applying low values of plunge depth results in TW fracture, whereas PO fracture mode occurs when high values of plunge depth is applied. Furthermore, it is important noting that the optimized values of strength were found for intermediate plunge depth, in the transition region of failure mode.

Taking into account that Plunge Depth is the main process parameter to define hook tip shape formation and based on the clear effect of Plunge Depth on the failure mode, there are some indicative that weld mechanical performance and fracture behavior are related to the hook tip shape. This hypothesis was investigated using interrupted mechanical tests and microstructure analysis,

aiming to identify crack initiation and propagation for different hook tip shapes in RFSSW welds. The results are presented in the next section.

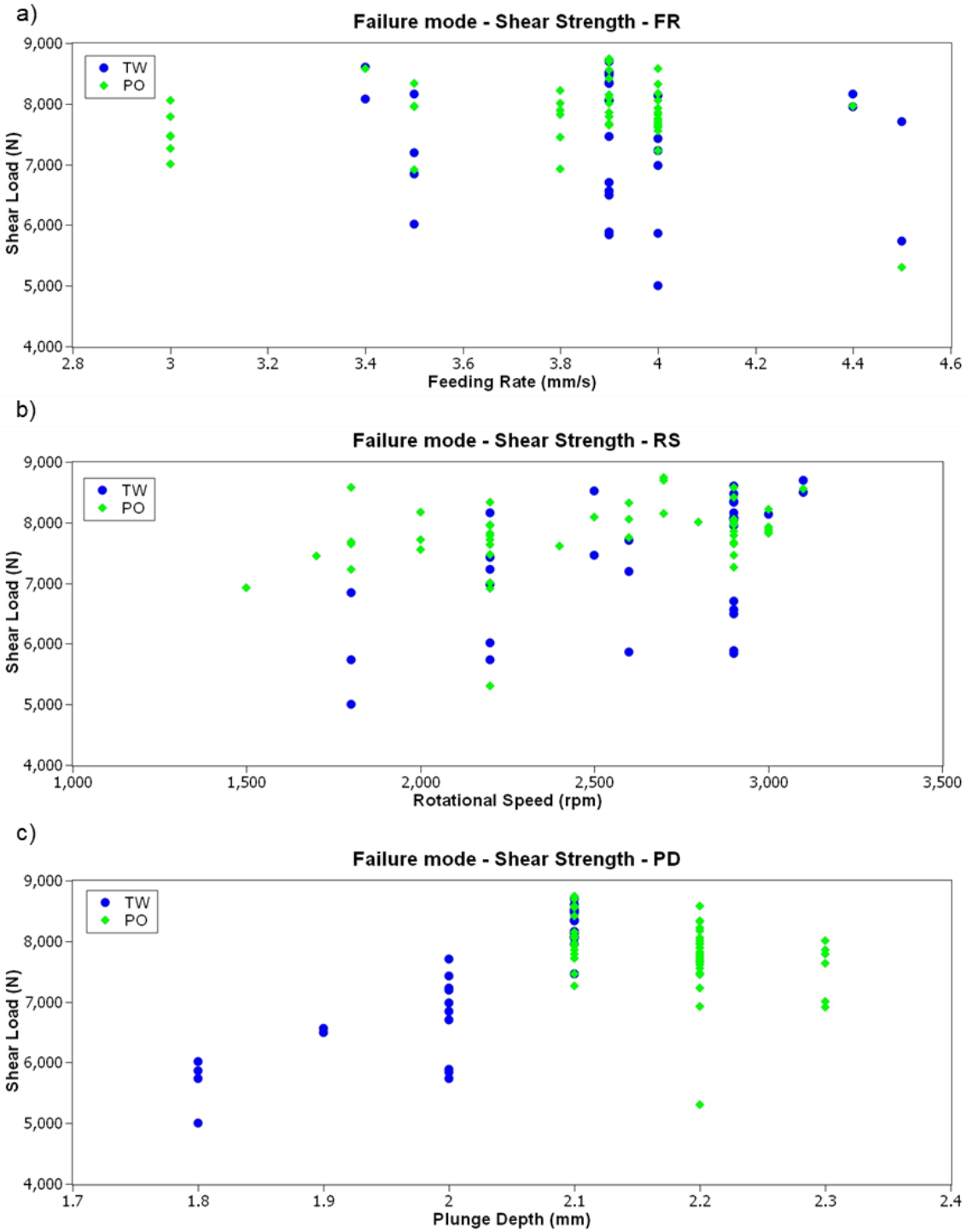

Figure 5.14 - Correlations between shear strength, fracture mode and processes parameters: a) Feeding Rate, b) Rotational Speed and c) Plunge Depth.

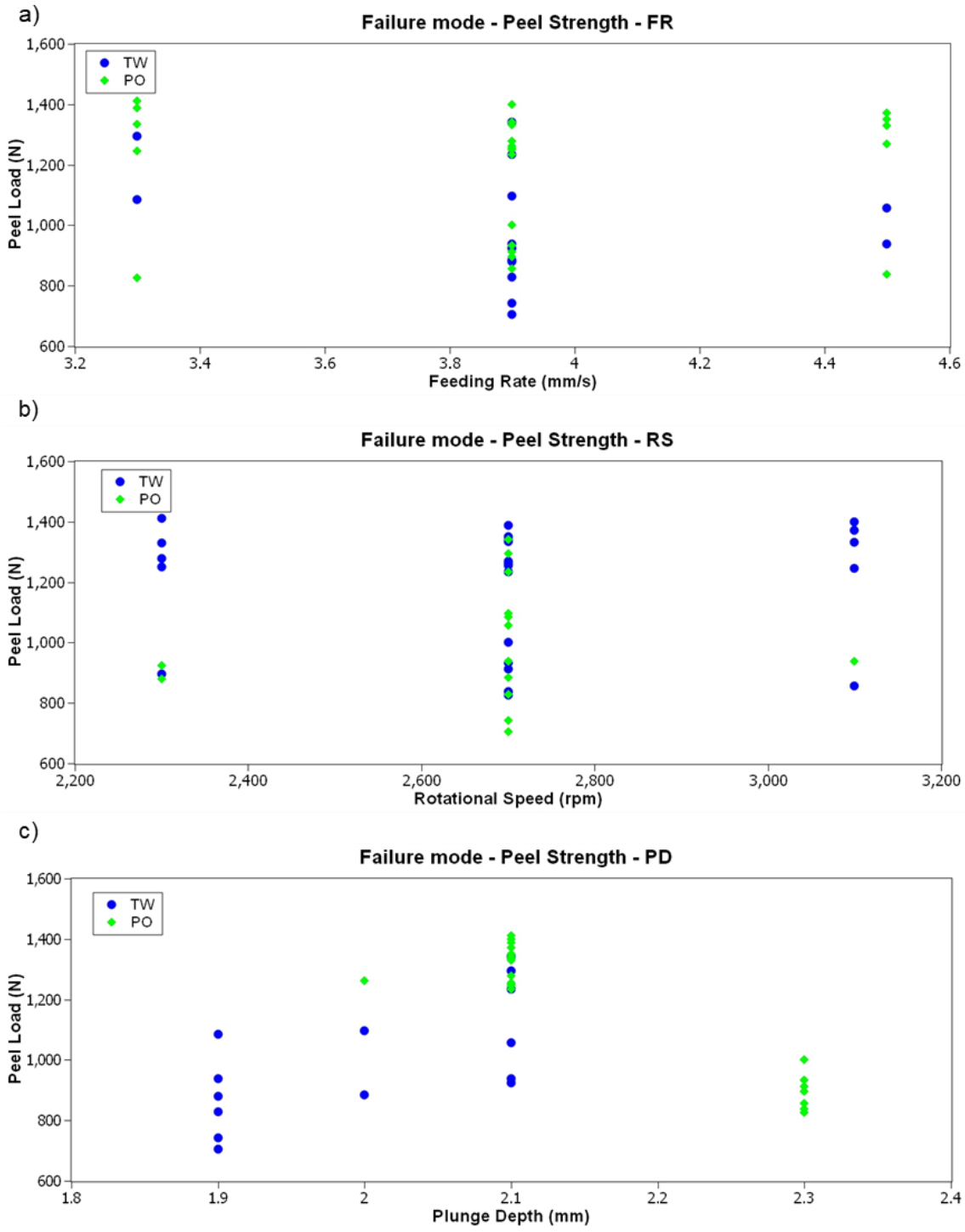

Figure 5.15 - Correlations between peel strength, fracture mode and processes parameters: a) Feeding Rate, b) Rotational Speed and c) Plunge Depth.

5.3.3 Interrupted mechanical tests

Figure 5.16 shows the macrostructure of an interrupted shear test of a welded sample produced with low Plunge Depth value (**PD**=1.9 mm), which is related to flat hook tip shape. It is observed the interfacial fracture related to TW fracture for this configuration. Moreover, by analyzing the microstructure around the crack tip region (Figure 5.17) it can be noted that the crack started in the hook tip defect and propagated exactly through the Bonding Ligament indicating that this region is susceptible to crack propagation.

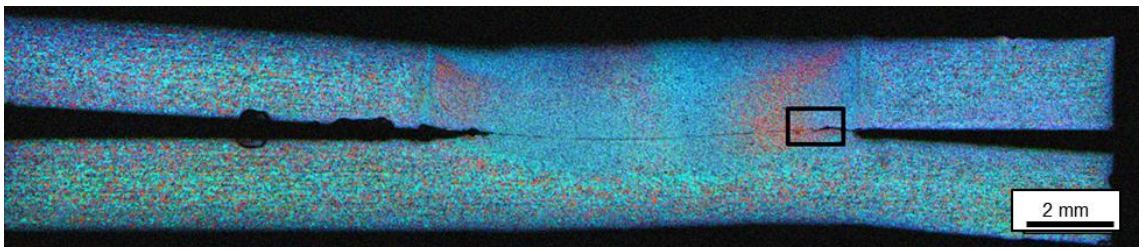

Figure 5.16 - Macrostructure of an interrupted shear test sample with flat hook tip shape produced using low value of Plunge Depth (PD:1.9mm).

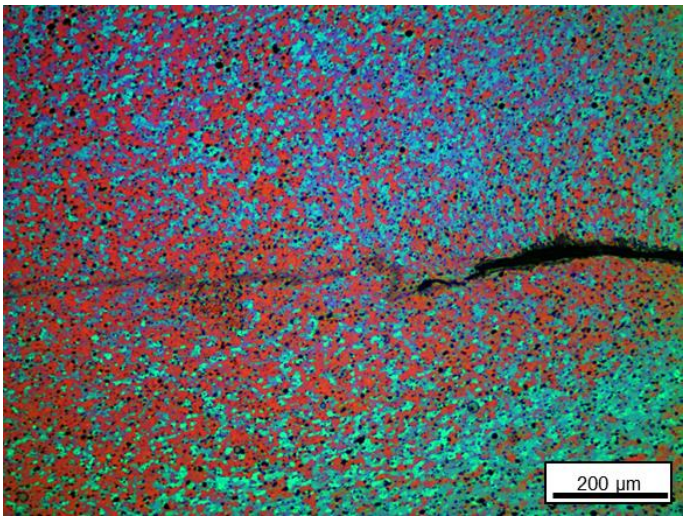

Figure 5.17 - Microstructure of the crack tip region from interrupted shear test sample with flat hook tip shape produced with low value of Plunge Depth (PD:1.9mm).

Figure 5.18 shows the macrostructure of an interrupted shear test of a sample produced with high plunge depth value (**PD**=2.3mm), which is related to

hook tip pointing up. Fracture path around the nugget region indicates PO fracture mode. By analyzing the microstructure around the crack region in Figure 5.19, one can see that the crack started in the hook tip region and propagated by the region between TMAZ and HAZ indicating that this region is susceptible to crack propagation. It is important to note that the hook tip shape pointing up acts as a stress concentration site, as also reported in literature [23], and since this region is connected to TMAZ/HAZ (a soft region of the weld), the crack propagates easily through this region.

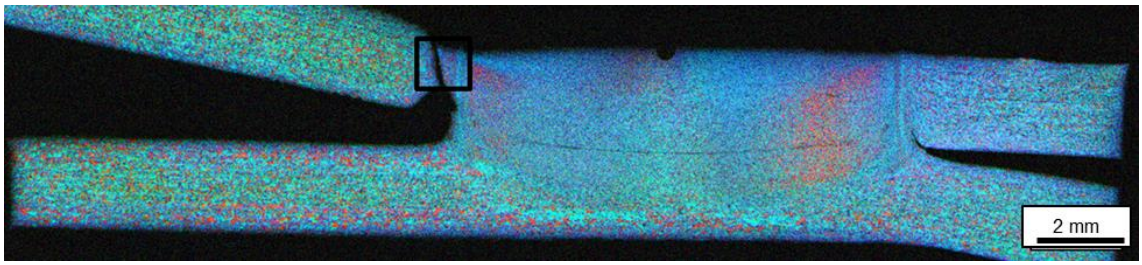

Figure 5.18 - Macrostructure of an interrupted shear test sample with hook tip pointing up, produced using high value of Plunge Depth (PD:2.3mm).

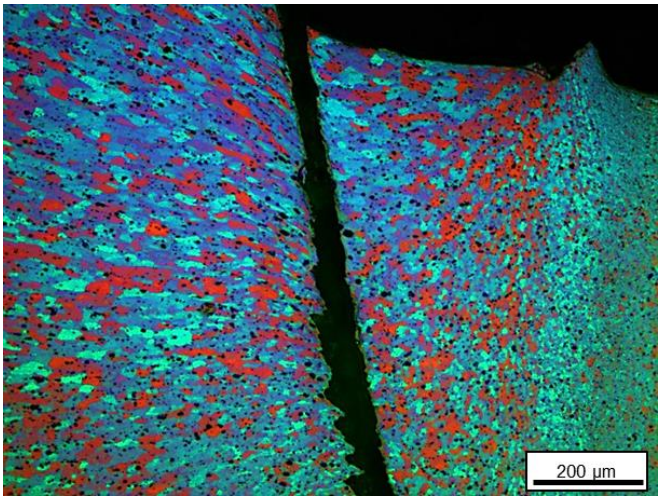

Figure 5.19 - Microstructure of the crack region from interrupted shear test sample, with hook tip shape pointing up produced by high value of Plunge Depth (PD:2.3mm).

Figure 5.20 shows macrostructure of an interrupted shear test from a sample produced by intermediate plunge depth (**PD**=2.1mm), which is related to hook tip pointing down. Figure 5.21 (a) presents apparently a Pull-Out fracture

mode since the crack starts at the hook defect region and propagates through the HAZ/TMAZ region. However, Figure 5.21 (b) presents signs of both types of fracture modes. One of the cracks started at the hook tip region and propagated through the Bonding Ligament, similarly to the interfacial fracture mode observed in Figure 5.16 and Figure 5.17. On the other hand, the other crack seems to start at the hook tip region, but it propagates through the base material region in the lower sheet resulting in PO fracture. It is also important noting that the interfacial crack has stopped exactly under the Drop region (Figure 5.21 (b)), which can be characterized as a mechanical barrier avoiding crack propagation through the Bonding Ligament.

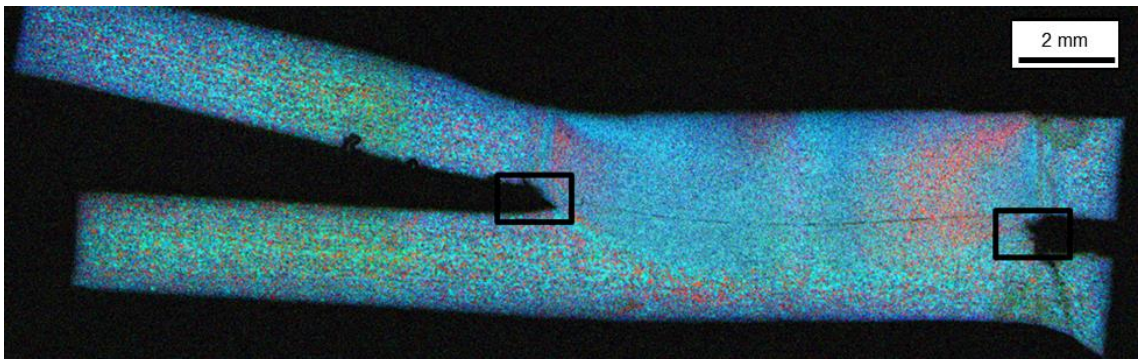

Figure 5.20 - Macrostructure of an interrupted shear test sample with hook tip pointing down produced using intermediate value of Plunge Depth (PD:2.1mm).

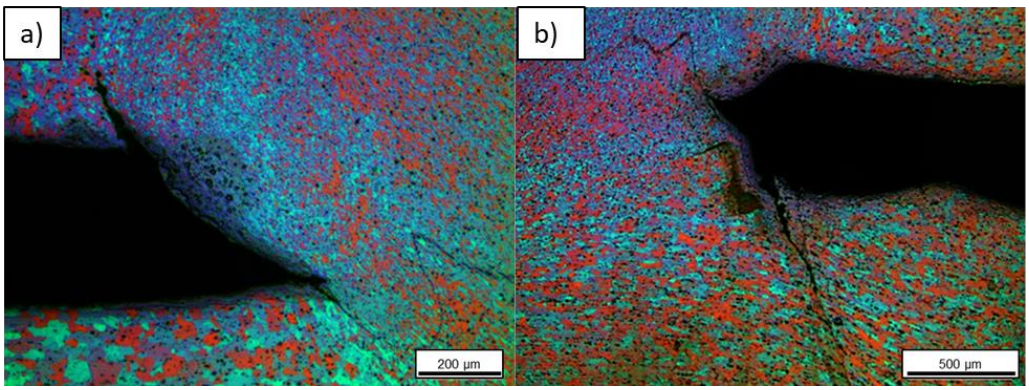

Figure 5.21 - Microstructures of the cracks regions from interrupted shear test sample with hook tip pointing down produced with intermediate value of Plunge Depth (PD:2.1mm). a) crack following TMAZ/HAZ region and b) cracks following hook tip region and base material.

Based on the results presented in this work, it was possible to find the main features of RFSSW weld that control the weld strength and fracture behavior in monotonic mechanical tests. The microstructure feature that controls the fracture mode is the hook tip shape and its interaction with the Bonding Ligament. The combination of a weakly bonded Bonding Ligament connected to a flat hook tip favors TW fracture. This combination is provided by low values of Plunge Depth (lower than the sheet thickness). PO fracture mode occur in the hook tip region and the soft region between TMAZ and HAZ. The combination of the hook tip stress concentration (which is higher for hook tip pointing up [23]) connected with the soft region between TMAZ and HAZ favors PO fracture. Using high values of Plunge Depth these characteristics are more pronounced. In the intermediate condition between these two conditions (hook tip pointing down, intermediate values of Plunge Depth), stress concentration at the hook tip region is reduced when compared to hook tip pointing up [23]. Moreover, the Bonding Ligament region presents stronger bond when compared to the Bonding Ligament formed for low Plunge Depth. In addition, Drop region formation in front of the hook tip region acts as barrier for crack propagation through the Bonding Ligament. Therefore, both types of fracture can happen, which will depend on the Bonding Ligament and TMAZ/HAZ strength. In conclusion, it was found that Plunge Depth controls the microstructure features as well the hook tip shape, Drop region and others, which in turn control the weld strength and fracture behavior.

5.4 Bake Hardening effect on weld structure and properties

5.4.1 Temperature measurements

During the welding process, deformation and frictional heat produce microstructural changes regarding amount, morphology and size of phases present in the material. Considering the AA6082 alloy, the fraction of GP zones, β'', β' and β phases can be altered. In the case of the AA6082-T6 alloy, the volume of β'' must be higher than the other precipitated phases because of the T6 heat treatment [68]. Thus, it is expected that heat input during the welding process will result in β'' coarsening, transformation of β'' into β'/β, or complete

precipitates dissolution as discussed in section 3.5. Then, characterizing the thermal profile in the welded regions is the first step to recognize which precipitation/dissolution process takes place during welding process.

Temperature measurements in the SZ and HAZ regions (Figure 5.22) shows that there is a large difference between the thermal history of these two regions. The maximum temperature of the SZ region was around 500 ºC, which is near to the solubilization temperature. It is worth remembering that the SZ is subjected to high strain levels, which also contribute to fragmentation/dissolution process in this region. On the other hand, the maximum temperature reached in the HAZ region was almost half of the one observed for the SZ region, which might have resulted in precipitate coarsening [61,64,73].

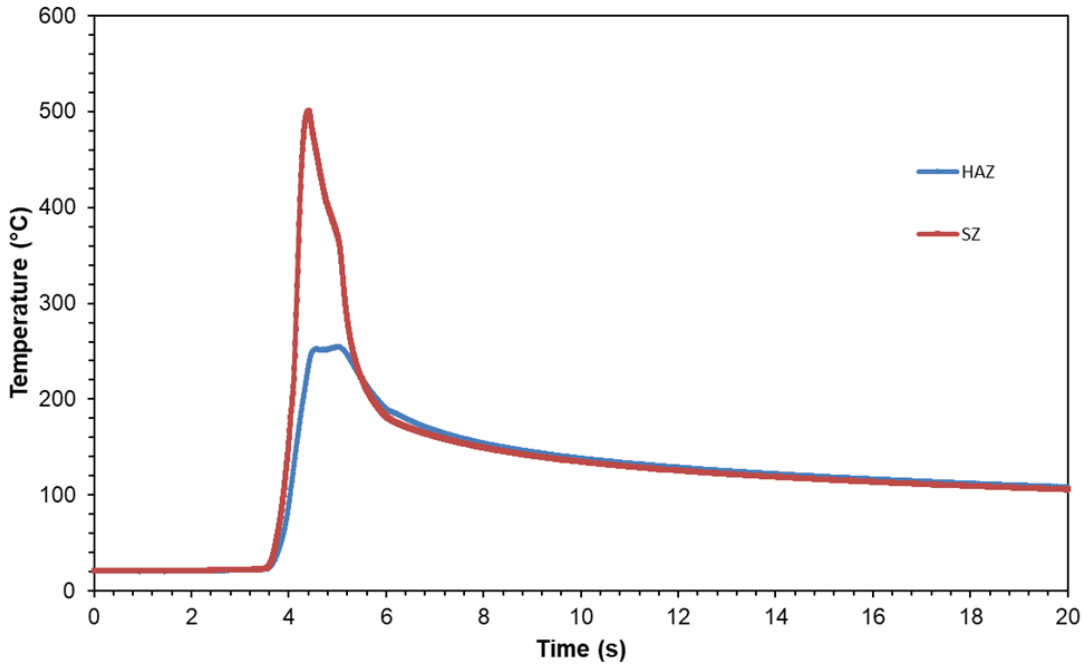

Figure 5.22 - Temperature measurements in the SZ and HAZ regions during RFSSW welding. (process parameters applied - PD: 2.1 mm, FR: 3.9 mm/s and RS: 2700 rpm)

5.4.2 Thermal Analysis (DSC)

To confirm the hypothesis of dissolution process in SZ and coarsening process in HAZ, DSC analysis were carried out in samples from these two regions and from the base material (BM). The thermal behavior of these three regions (Figure 5.23) were compared with the 8 enthalpic signals reported by Birol for the AA6082 alloy [45]. The first enthalpic signal found in BM sample was the endothermic peak associated with the dissolution from remaining GP-Zones present in the material. The second signal determined in the BM sample is a weak exothermic precipitation signal, associated to β'' precipitation. Since in T6 conditions β'' is the main phase precipitated, this signal was expected to be weak demonstrating just a remaining precipitation process for this phase. The three last signals determined in BM sample are associated to overaging conditions, β' precipitation, β''/β' dissolution and β precipitation, which are in accordance to Birol's observations.

Regarding the HAZ sample, it was detected three enthalpic signals: the first one between 200-270 ºC was related to an overlapping effect of β''/β' precipitation; the second peak was associated with the β''/β' dissolution; and the third was related to β precipitation. It is likely that, in this condition, the remaining pre-existent GP-Zones were completely dissolved or precipitated into β''/ β' during welding procedure, therefore, no dissolution peak of GP-Zones was detected during DSC analysis agreeing with the hypothesis of coarsening process in this region. Similarly, the pre-existent β'' might be coarsened and transformed to β' during the weld, resulting in the overlapping peak of β''/ β' during DSC analysis. This affirmative is supported by the absence of an intense peak of β' precipitation, since most of this phase was supposed to form by coarsening mechanisms during welding process. However, this assumption must be further investigated in future works.

Differently from HAZ and BM samples, SZ sample shows weak enthalpic signals before 200 ºC, which are related to GP-Zones formation, demonstrating reprecipitation process as discussed in section 3.4. Therefore, this behavior in DSC curve supports the hypothesis of dissolution process in SZ region during

welding process, since the BM (which is in T6 condition) presented no signal before this temperature. In addition, the SZ sample presented a dissolution peak of GP-Zone phase, which was not detected in the HAZ, demonstrating the differences of precipitation conditions between these regions. It is also important to notice the intense peak of β'' and β' precipitation found in the SZ, quite different from the overlapping effect observed in HAZ sample. Finally, it must be highlighted the resemblance between SZ behavior and the curve obtained by Birol [45] from a solutioned and quenched sample of AA6082. Regarding on the number of peaks, the only difference observed was the absence of the first peak observed by Birol, which is associated to extensive clustering effect. This peak absence might be related to the difference of quenching treatment, since Birol quenched the samples in water, while in this work the samples were air cooled after welding. Therefore, the saturation levels might not be high enough to show the clustering peak in DSC analysis. Nevertheless, these assumptions also need further investigation (TEM or 3DAP characterizations are suggested in future works).

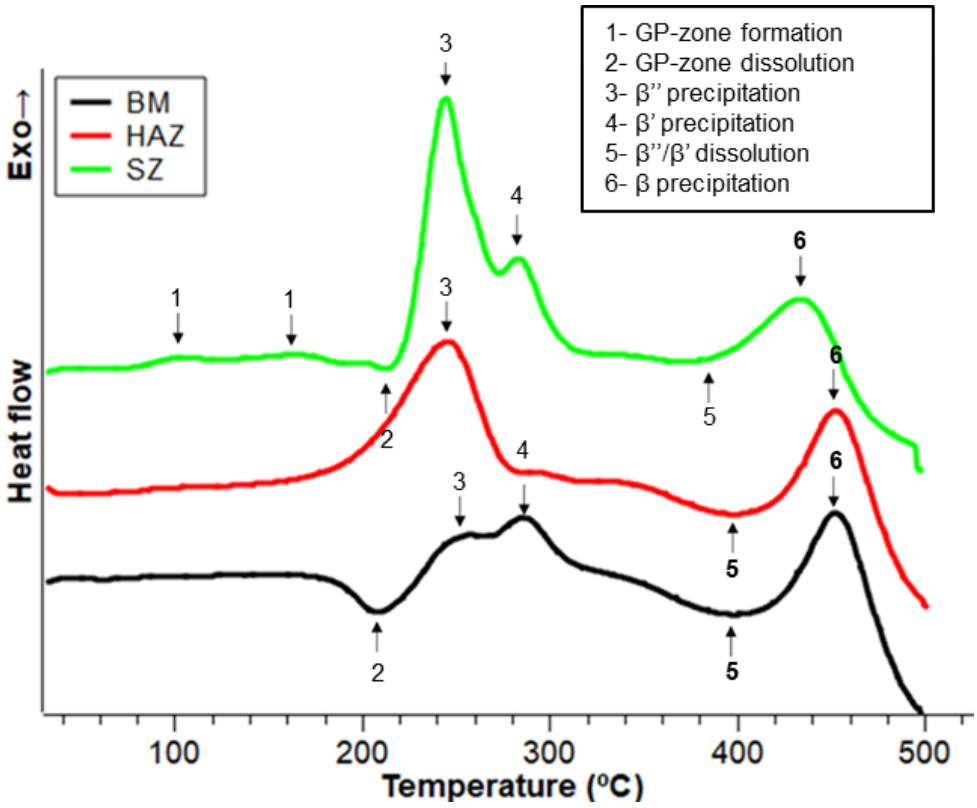

Figure 5.23 - DSC curves of BM, HAZ and SZ samples.

5.4.3 Hardness evaluation

Hardness maps produced from weld samples with and without Bake Hardening treatment are shown in Figure 5.24. Hardness profile from as welded sample presented hardness in base material around 110 HV. At the same sample, hardness in HAZ region showed values varying between 63-110 HV, whereas in SZ values between 63-75 HV were found. After Bake Hardening treatment, the BM and most part of HAZ region reduced hardness around 10-20 HV, whereas for the SZ region the hardness values increased 10-20 HV. These results also support the hypothesis of high dissolution levels in SZ and coarsening process in HAZ during welding.

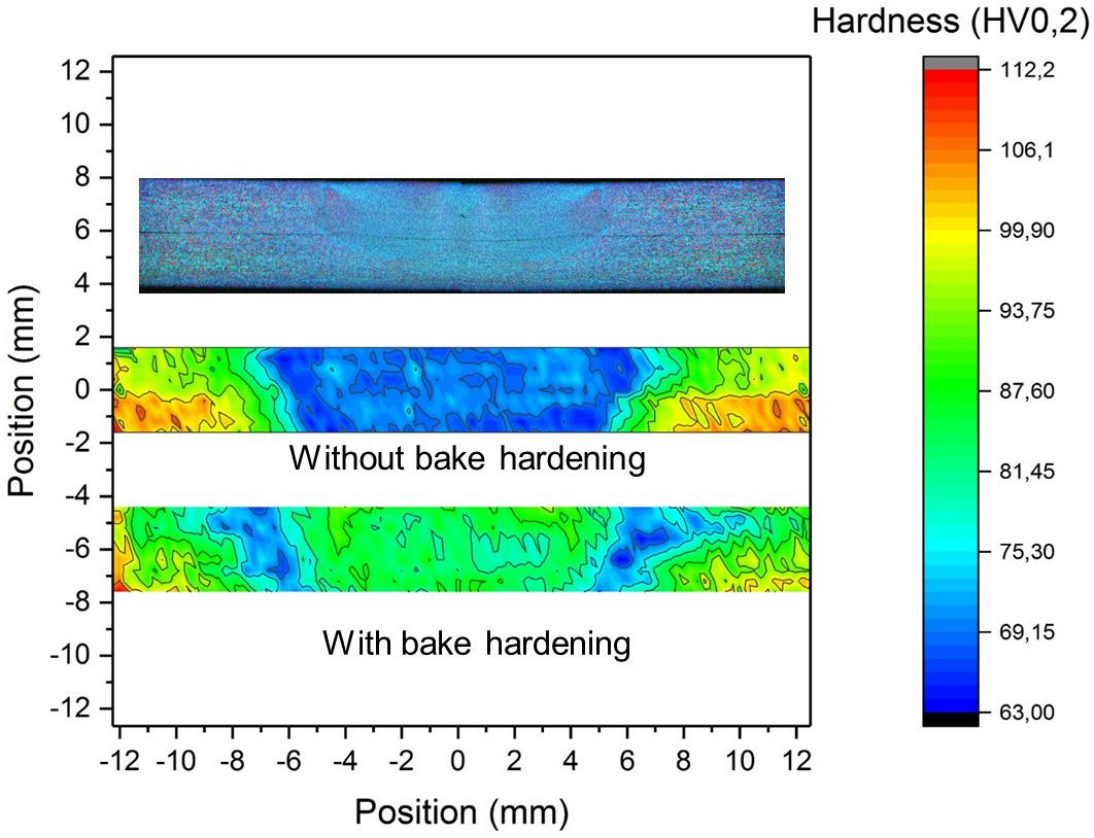

Figure 5.24 - Hardness maps produced from RFSSW welds of AA6082-T6 with and without Bake Hardening treatment.

5.4.4 Mechanical Behavior

Figure 5.25 shows the effect of Bake Hardening Treatment in shear strength for the three hook shapes (flat, pointing down and pointing up) studied in previous sections. Although Bake Hardening slightly improved shear strength for hook pointing down and hook pointing up conditions, the effect of Bake Hardening on the mechanical properties of these configurations can be considered negligible. On contrary, for flat hook configuration a significant improvement in the shear strength was detected. For flat hook condition, TW fracture is favored due to hook connection with Bonding Ligament, which is usually a weak region from RFSSW weld. However, since Bonding Ligament is within the SZ region, shear strength improvement for flat hook configuration might be related to the reprecipitation process (which improved hardness in the SZ region) caused by Bake Hardening treatment as observed in Figure 5.24. For the hook pointing down configuration without Bake Hardening, fracture occurred either through SZ or between HAZ/TMAZ region, resulting in either TW or PO fracture mode (see section 5.3.3). Therefore, considering the effect of Bake Hardening treatment in each region, it is expected that this treatment favors PO fracture, since SZ strength is improved and HAZ/TMAZ strength is reduced after treatment. Nevertheless, as PO fracture occurs through a region that is not hardened by Bake Hardening treatment, it is plausible that shear strength has no significant improvement for hook pointing down condition. The negligible improvement in shear strength for hook pointing up might be justified with similar assumptions regarding HAZ/TMAZ strength reduction, since for this configuration PO fracture is the main fracture mode even without Bake Hardening treatment.

In order to further support these assumptions relating Bake Hardening effect on weld strength and fracture behavior for the three hook configurations, a plot correlating fracture mode, Plunge Depth parameter and maximum shear load is showed in Figure 5.26. Observing the fracture modes of the bake hardened samples, it can be seen that the only fracture mode obtained for hook tip shape pointing down configuration (**PD**=2.1mm) was PO, whereas in Figure 5.14 and Figure 5.15 both types of fracture can be seen for the same configuration of hook

tip without Bake Hardening. These results confirmed the assumptions made about precipitation evolution in SZ and HAZ from welded conditions to bake hardened conditions, since SZ dissolution/reprecipitation and HAZ coarsening process favors PO fracture because of the higher hardness of SZ region avoid TW fracture.

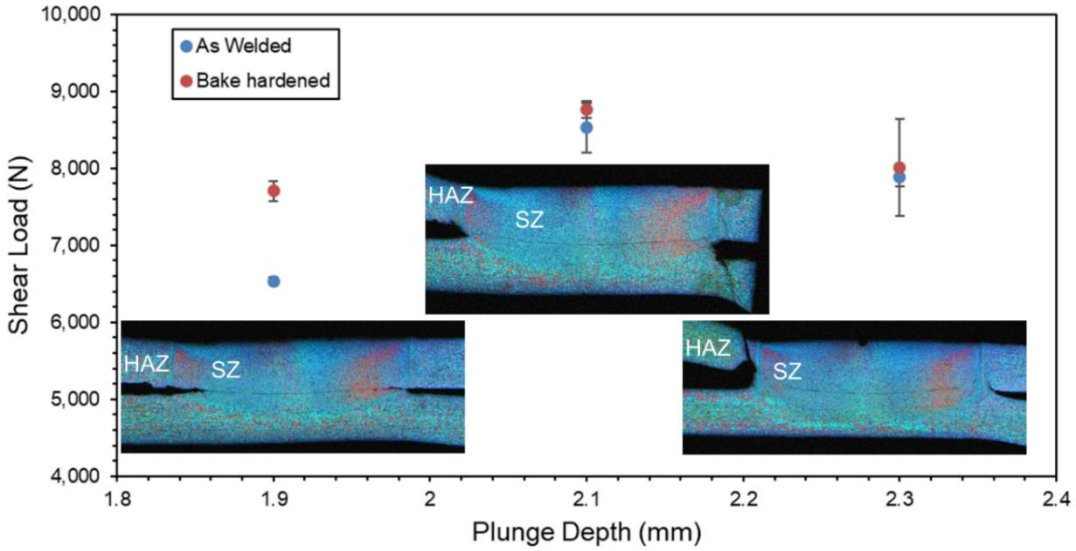

Figure 5.25 - Bake Hardening effect on the shear strength for the three hook tip shape configuration (flat, pointing down and pointing up).

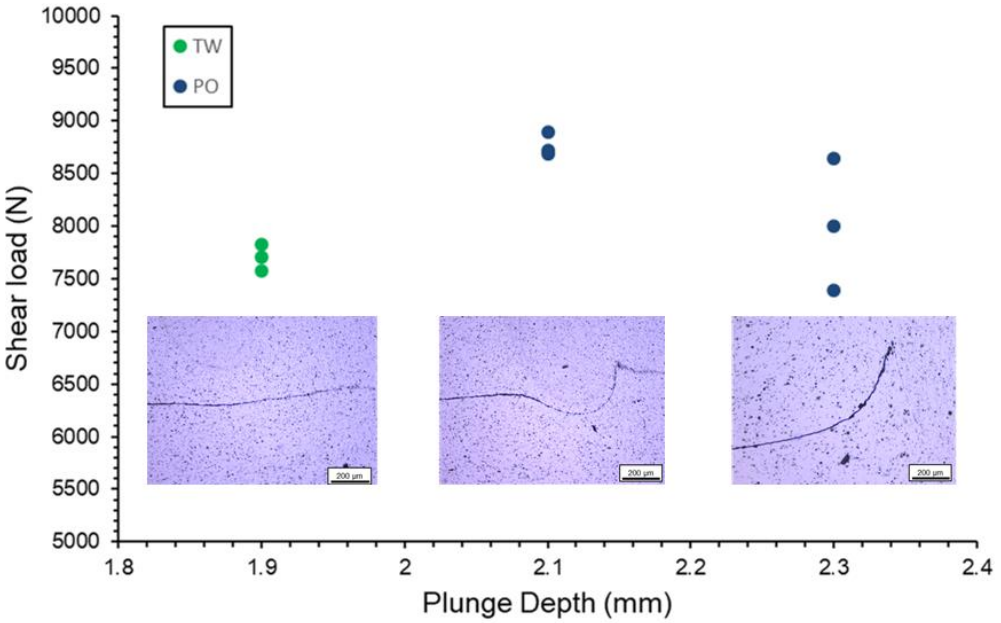

Figure 5.26 - Bake Hardening effect in fracture mode on the three hook tip shape configurations (flat, pointing down and pointing up).

These results are in agreement with the discussion of the effect of Bake Hardening treatment in aluminum alloys in different aging conditions from previous works [7,74–78]. Moreover, it is highlighted the effect of this treatment in mechanical properties and fracture behavior, which potentially provides information to future industry applications, for instance, in automotive industry, where it is often applied.

5.5 Fatigue results

5.5.1 Fatigue properties evaluation and Weibull Statistical analysis

Fatigue tests were performed for the three hook conditions analyzed in this work. Therefore it was tested welds with the following process parameters set (PD:2.1 mm, FR:3.9 mm/s and RS:2700 rpm), (PD:1.9 mm, FR:3.9 mm/s and RS:2700 rpm) and (PD:2.3 mm, FR:3.9 mm/s and RS:2700 rpm) which produced welds with hook pointing down, flat hook and hook pointing up configuration, respectively.

In Table F, Table G and Table H are available the tests conditions, fatigue life results and fracture mode observed for the three hook conditions. Weibull plots were obtained applying the data of number of cycles to fracture and the Load levels on the Equations 4.2, 4.3 and 4.4. The fitting of these data with the Weibull distribution was assessed in Figure 5.27 (a), (b) and (c). It is observed a reasonable linearity for all load levels of the three hook conditions (R^2 values were higher than 0.7 for all linear regressions). Nevertheless, it was considered that the data had a reasonable fitting with Weibull distribution.

The linear coefficient ($-\beta\ln(\alpha)$) and the slope (β) of each line in Figure 5.27 (a), (b) and (c) provided the Weibull parameters (α,β) for each Load level. Weibull parameters and the Weibull Mean Time To Fracture (MTTF) (calculated by Equation 4.5) are presented for the three hook conditions in Table 5.4, Table 5.5 and Table 5.6.

a)

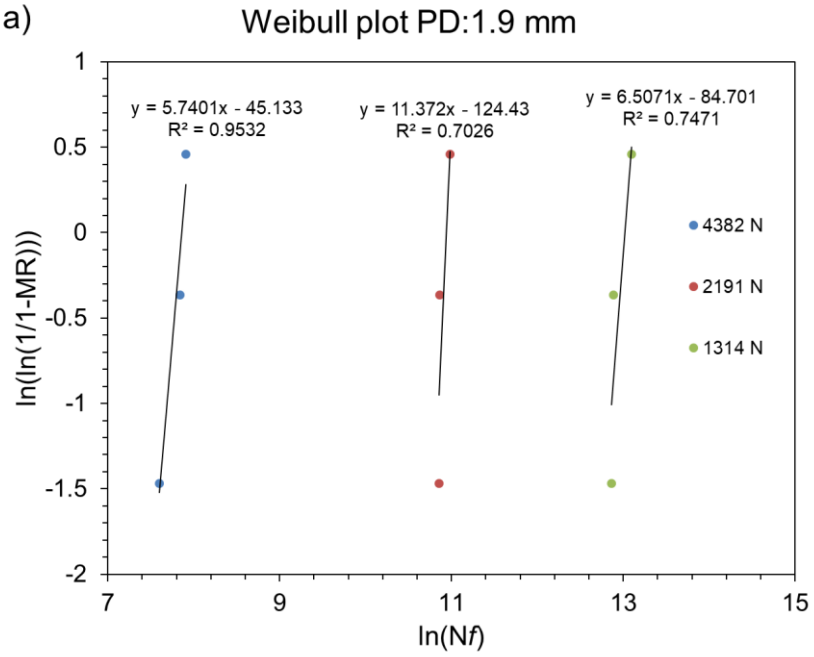
Weibull plot PD:1.9 mm
y = 5.7401x - 45.133
R² = 0.9532
y = 11.372x - 124.43
R² = 0.7026
y = 6.5071x - 84.701
R² = 0.7471
4382 N
2191 N
1314 N
ln(ln(1/1-MR)))
ln(Nf)
1
0.5
0
-0.5
-1
-1.5
-2
7
9
11
13
15

b)

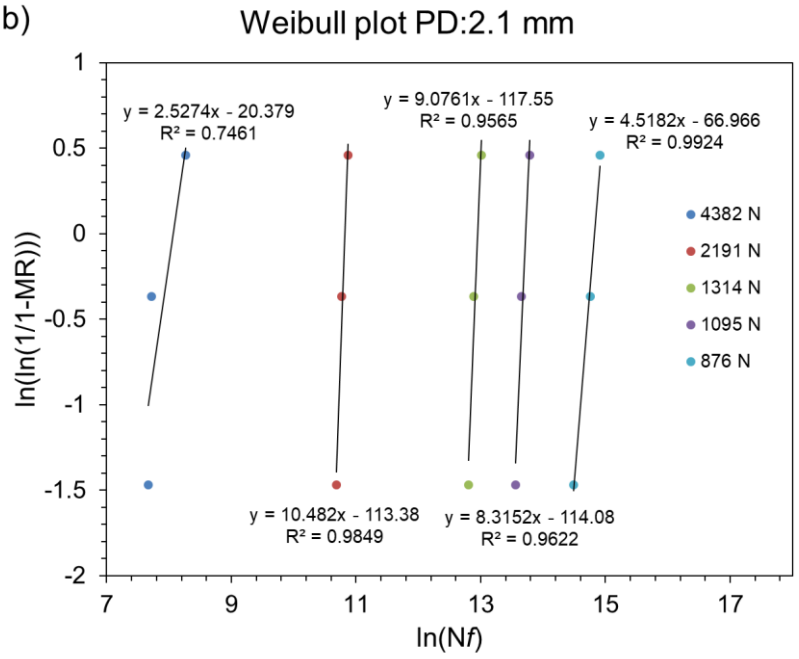
Weibull plot PD:2.1 mm
y = 2.5274x - 20.379
R² = 0.7461
y = 9.0761x - 117.55
R² = 0.9565
y = 4.5182x - 66.966
R² = 0.9924
y = 10.482x - 113.38
R² = 0.9849
y = 8.3152x - 114.08
R² = 0.9622
4382 N
2191 N
1314 N
1095 N
876 N
ln(ln(1/1-MR)))
ln(Nf)
1
0.5
0
-0.5
-1
-1.5
-2
7
9
11
13
15
17

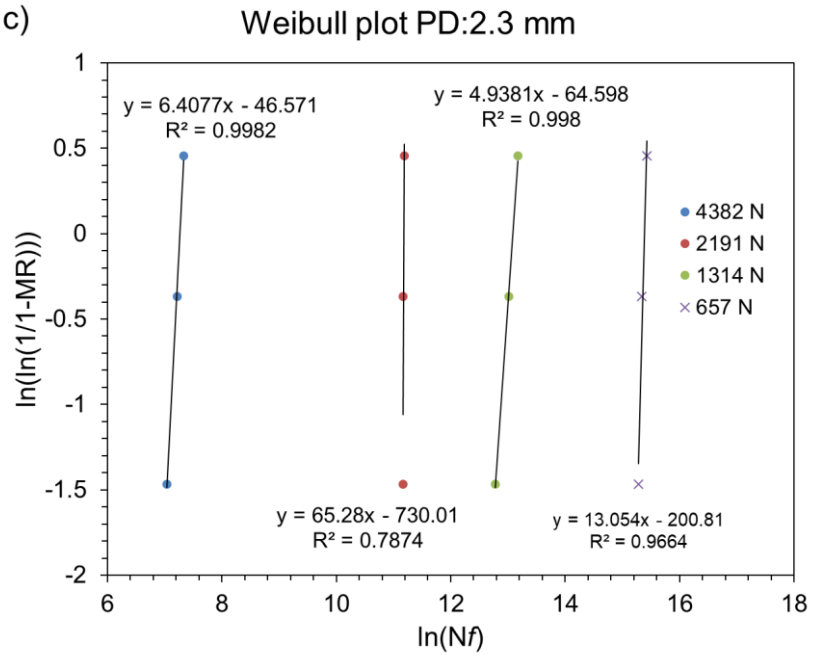

Figure 5.27 - Weibull plots of the data from a) flat hook condition, b) hook pointing down condition and c) hook pointing up condition.

Table 5.4 - Weibull parameters and Mean Time to Fracture from flat hook condition.

Load Level (N)	Scale Parameter (α)	Shape Parameter (β)	Mean Time To Fracture - MTTF (cycles)
4382	2598.8	5.74	2405
2191	56475.6	11.37	54009
1314	449833.0	6.51	419170

Table 5.5 - Weibull parameters and Mean Time to Fracture from hook pointing down condition.

Load Level (N)	Scale Parameter (α)	Shape Parameter (β)	Mean Time To Fracture – MTTF (cycles)
4382	3175.0	2.53	2818
2191	49826.9	10.48	47496
1314	421310.1	9.08	399118
1095	908601.1	8.32	857259
876	2734575.5	4.52	2496085

Table 5.6 - Weibull parameters and Mean Time to Fracture from hook pointing up condition.

Load Level (N)	Scale Parameter (α)	Shape Parameter (β)	Mean Time To Fracture – MTTF (cycles)
4382	1433.7	6.41	1335
2191	71877.9	65.28	71259
1314	480062.4	4.94	440461
657	4796854.0	13.05	4610780

Using data from Table 5.4, Table 5.5 and Table 5.6 it was plotted the L-N curves for the three hook shape conditions as shown in Figure 5.28. The regression equations showed a good fitting of the analyzed data as R^2 values were higher than 0.9795. It is observed a similar trend in the three conditions, in special for load levels near the fatigue limit. This result suggests that hook tip shape has a negligible effect on fatigue life, specially near the fatigue limit. Considering the regression equations in Figure 5.28, it was calculated fatigue limit values of 1080 N, 1065 N and 1032 N (approximately 12% of the maximum load reached in monotonic shear test) for flat hook, hook pointing down and hook pointing up, respectively. These results are quite similar to the results obtained by previous works discussed in the literature review [18,35,79–81] demonstrating that RFSSW is not recommendable in applications that requires high load cyclic solicitation.

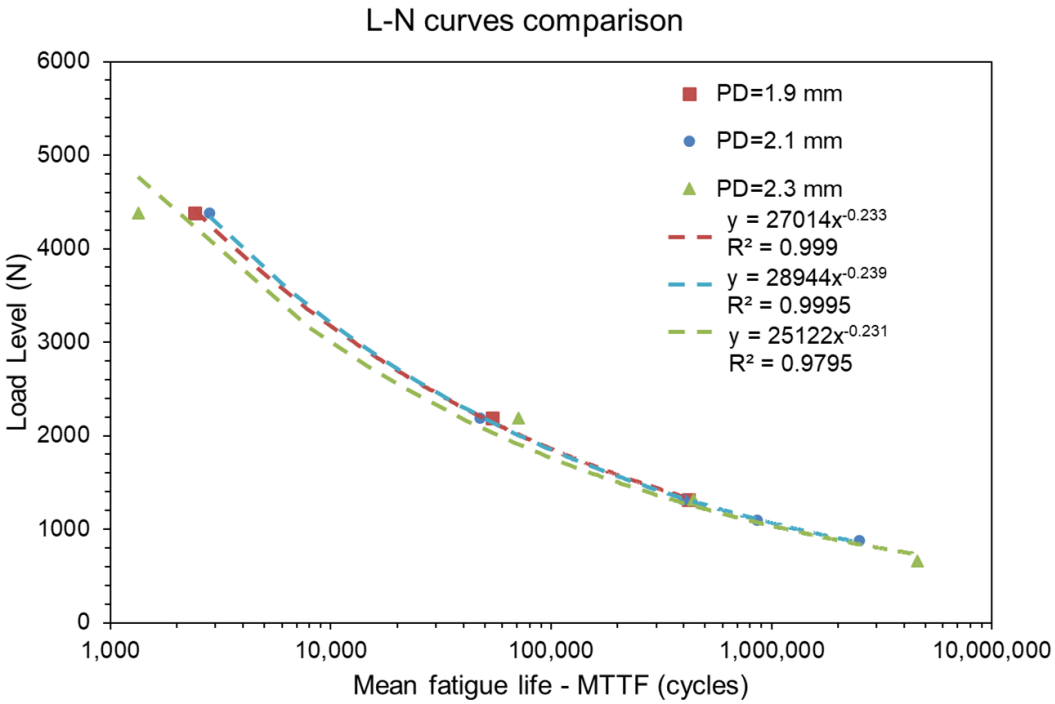

Figure 5.28 - L-N curves obtained by Weibull Statistical analysis for the three hook conditions.

Applying α and β values determined in Table 5.4, Table 5.5 and Table 5.6 in Equation 4.6 and using reliability levels of R_x =0.10, R_x =0.368, R_x =0.50 and R_x =0.99, L-N curves with different confidence levels for each hook configuration were plotted. Figure 5.29 (a), (b) and (c) show the L-N curves for the three hook conditions with different failure probabilities obtained by Weibull statistics. It is observed a good fitting coefficient of the regression equations, which showed R^2 values higher than 0.9615. It is important to highlight the similarity of these curves, specially near the fatigue limit, where Weibull distribution is more appropriated. On the other hand, for high levels of load it is observed a slight discrepancy comparing the L-N curves of the three hook conditions. For hook pointing down condition (Figure 5.29 (b)) a wider range between the L-N curves is observed than in hook pointing up and flat hook condition (Figure 5.29 (a) and (c)). These results demonstrate how useful Weibull statistical analysis are for fatigue life assessment. For instance, these curves allow us to predict the fatigue life according to the level of reliability desired by an engineer in automotive, aerospace and other transportation industries.

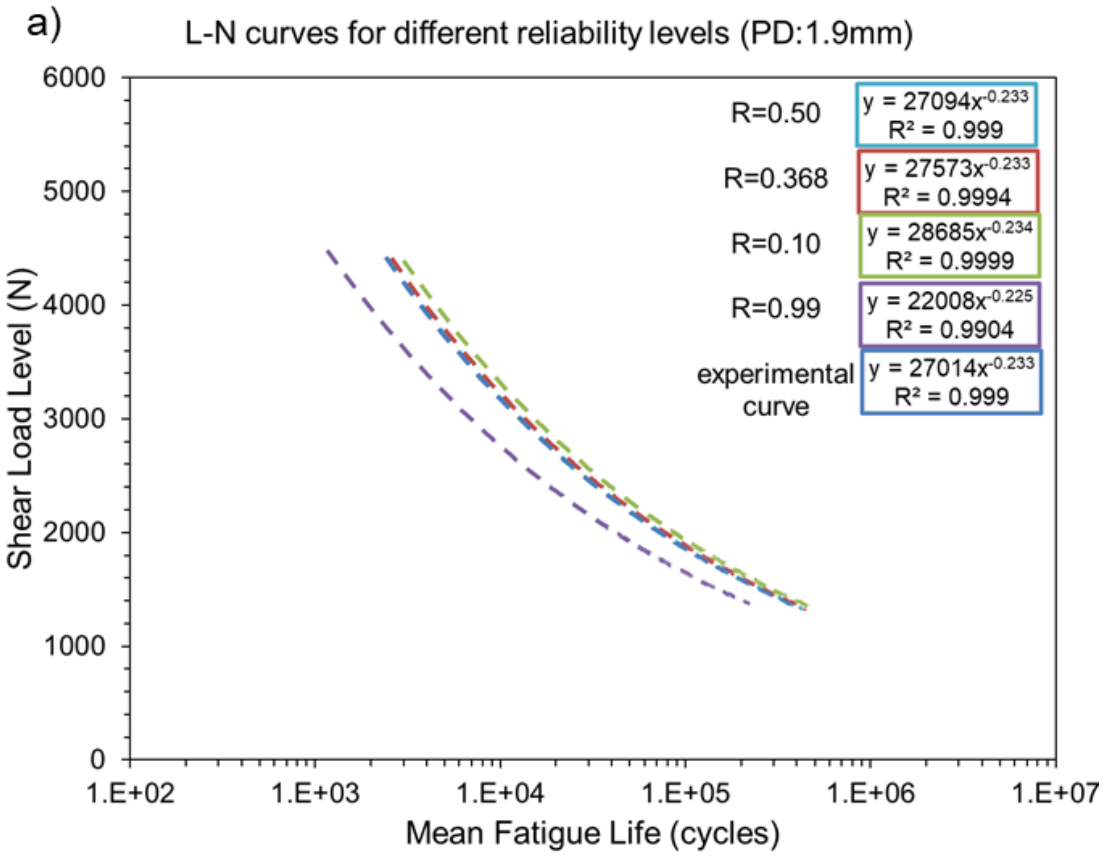
a)
L-N curves for different reliability levels (PD:1.9mm)
Shear Load Level (N)
Mean Fatigue Life (cycles)
6000
5000
4000
3000
2000
1000
0
1.E+02
1.E+03
1.E+04
1.E+05
1.E+06
1.E+07
R=0.50
y = 27094x-0.233
R² = 0.999
R=0.368
y = 27573x-0.233
R² = 0.9994
R=0.10
y = 28685x-0.234
R² = 0.9999
R=0.99
y = 22008x-0.225
R² = 0.9904
experimental curve
y = 27014x-0.233
R² = 0.999

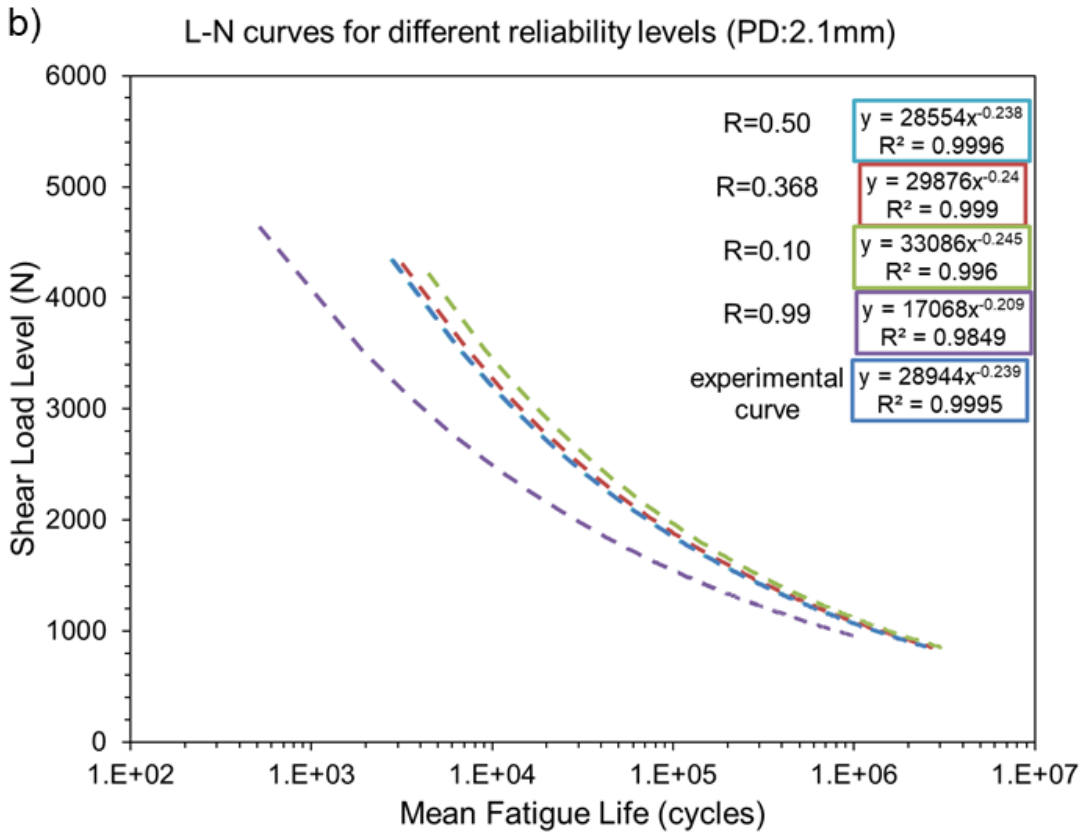
b)
L-N curves for different reliability levels (PD:2.1mm)
Shear Load Level (N)
Mean Fatigue Life (cycles)
6000
5000
4000
3000
2000
1000
0
1.E+02
1.E+03
1.E+04
1.E+05
1.E+06
1.E+07
R=0.50
y = 28554x-0.238
R² = 0.9996
R=0.368
y = 29876x-0.24
R² = 0.999
R=0.10
y = 33086x-0.245
R² = 0.996
R=0.99
y = 17068x-0.209
R² = 0.9849
experimental curve
y = 28944x-0.239
R² = 0.9995

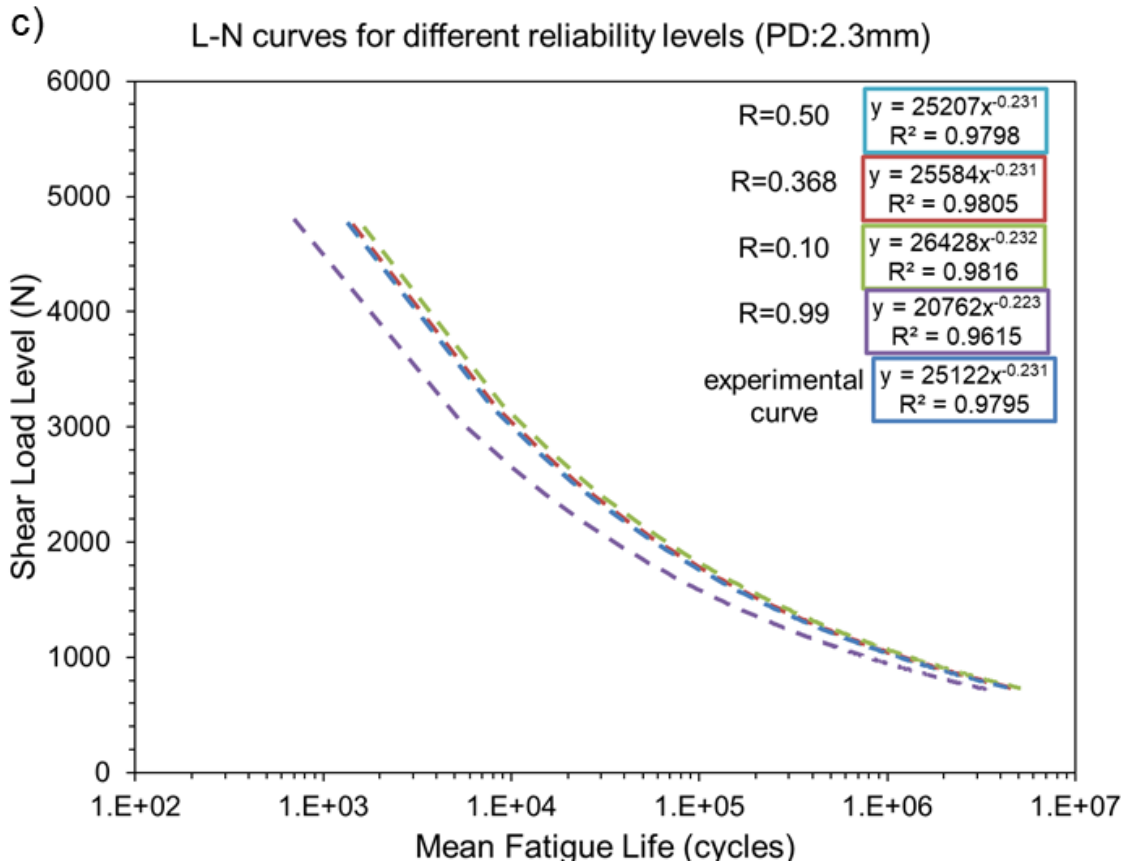

Figure 5.29 - L-N curves with different reliability levels for a) flat hook condition, b) hook pointing down condition and c) hook pointing up condition.

5.5.2 Fracture analysis

In order to understand the fatigue behavior for the three hook conditions, fracture analysis were carried out to identify the influence of hook defect on crack initiation and crack propagation process.

Four failure modes were identified during the tests as illustrated in Figure 5.30 (a), (b), (c) and (d). Figure 5.30 (a) shows a Through the Weld (TW) fracture, similar to the fracture showed in Figure 5.12 (a) and to fracture observation made by Plaine et al. and Shen et al [79,81], where the crack propagates along the interface between the two plates. Figure 5.30 (b) shows a circumferential fracture, where the nugget was pulled-out (PO1) from both plates. Figure 5.30 (c) shows a different circumferential fracture, where the nugget is pulled out (PO2) from only

one of the plates. These last two failure modes have similarities with the observations made by Brzostek et al. [35] and Effertz et al. [80]. Finally, Figure 5.30 (d) shows the Eyebrow (EB) shaped fracture, which was also discussed in several works on literature review [18,35,79–81].

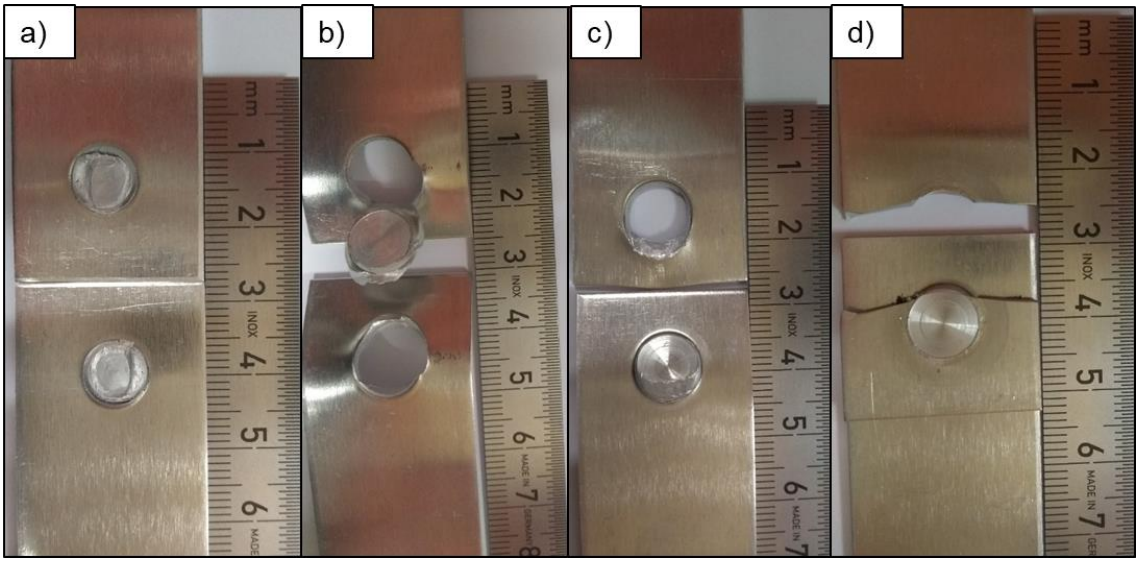

Figure 5.30 - Fracture modes identified during fatigue tests: a) Through the Weld (TW), b) Pull-Out the nugget from both plates (PO1), c) Pull-Out the nugget from only one plate (PO2) and d) Eyebrow fracture (EB).

A plot correlating fatigue life, fracture type and Load level is presented in Figure 5.31. A failure mode transition is observed. For low-cycle load conditions, the fracture mode behaves similarly to the described in monotonic shear and peel tests in section 5.3 (TW for flat hook and PO for hook pointing up and down), whereas for high-cycle load conditions (with loads lower than 25% of the maximum shear load), samples with the three hook conditions presented the same fracture type (EB). These results demonstrate that hook shape effect on fatigue life and fracture behavior are reduced according to the Load level applied and reaches a negligible level for high-cycle load conditions. These considerations are in agreement with previous work evaluations [35,79–81], in which a failure mode transition was observed in fatigue behavior from low-cycle to high-cycle conditions. Considering these observations, the similarities of the three curves in Figure 5.28 are reasonable, especially near the fatigue limit, since aside from hook tip shape, the welds are almost identical.

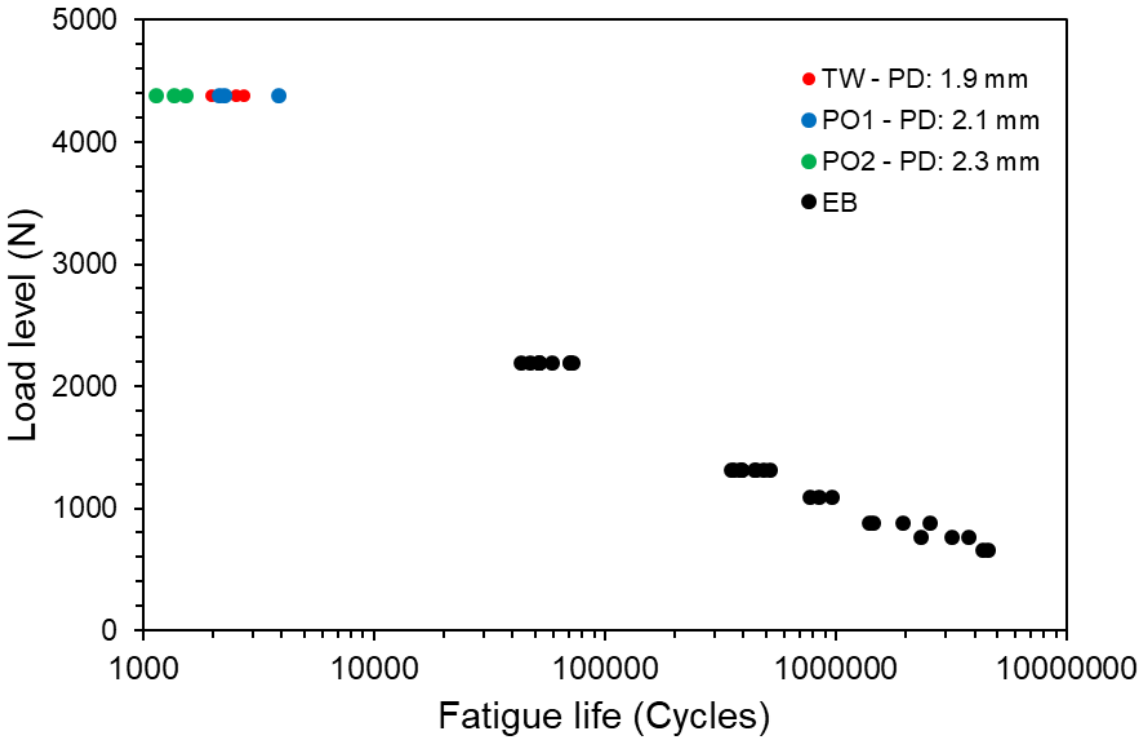

Figure 5.31 - Failure mode transition in fatigue solicitation for the three hook conditions.

Fatigue fracture surface analysis were carried out to investigate the fracture mechanisms for the four fracture modes observed during fatigue tests. Figure 5.32 shows the macrograph of an Eyebrow fatigue fracture surface. Higher magnification SEM images of selected regions (a-g) are shown in Figure 5.33.

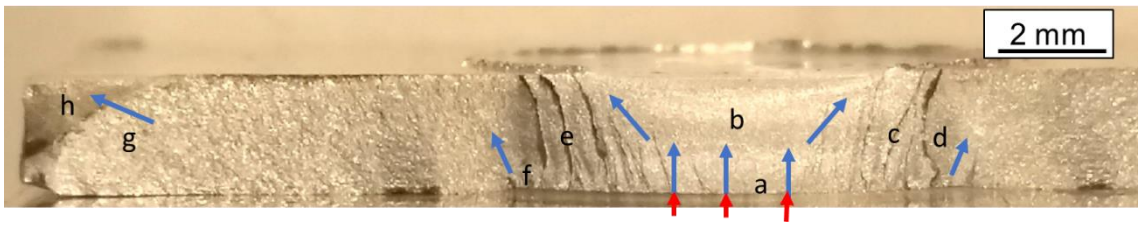

Figure 5.32 - Macrograph of the Eyebrow fatigue fracture surface indicating cracks nucleation site (red arrows) and crack propagation directions (blue arrows).

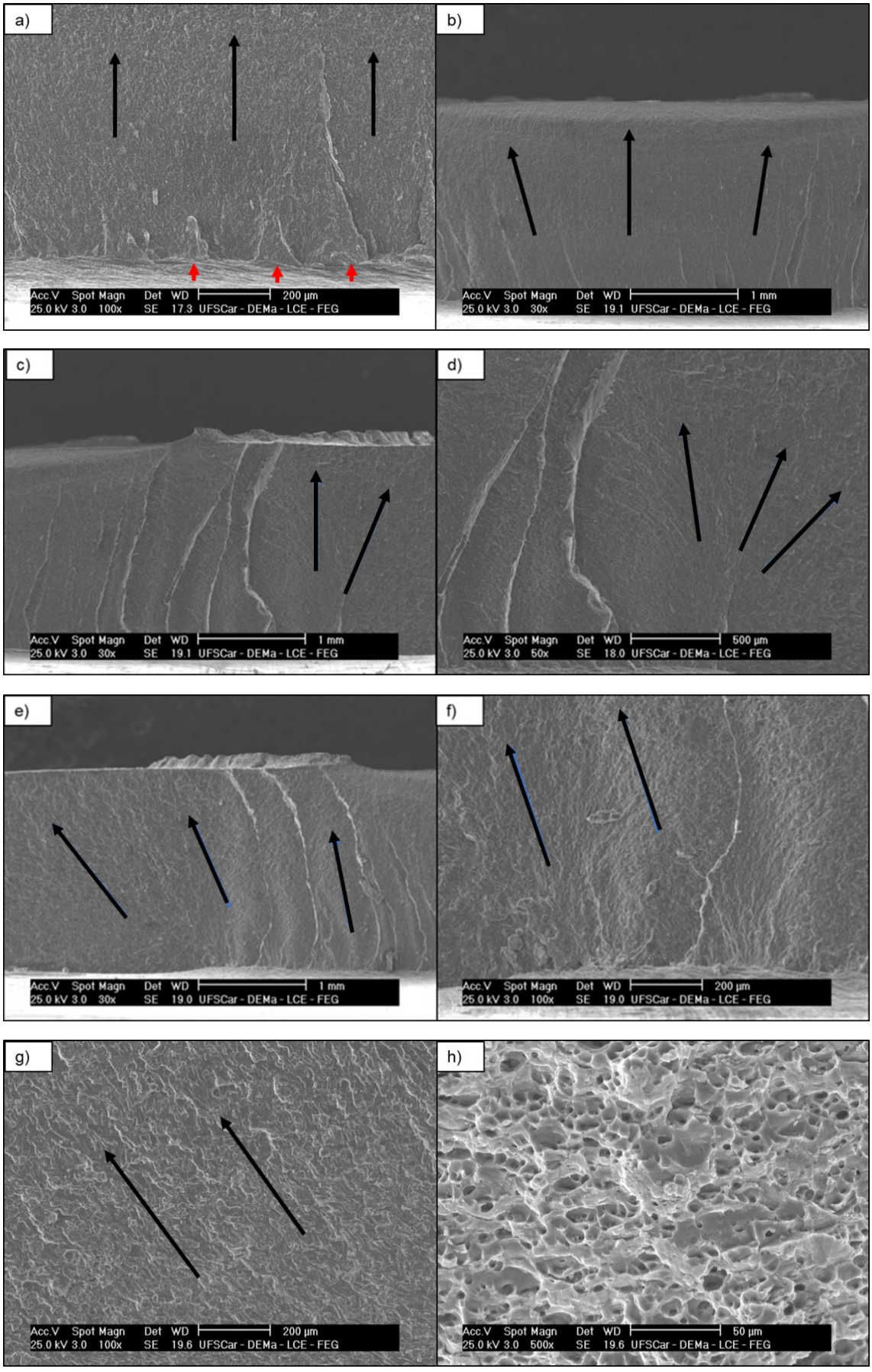
a)
Acc.V Spot Magn Det WD 200 µm
25.0 kV 3.0 100x SE 17.3 UFSCar - DEMa - LCE - FEG
b)
Acc.V Spot Magn Det WD 1 mm
25.0 kV 3.0 30x SE 19.1 UFSCar - DEMa - LCE - FEG
c)
Acc.V Spot Magn Det WD 1 mm
25.0 kV 3.0 30x SE 19.1 UFSCar - DEMa - LCE - FEG
d)
Acc.V Spot Magn Det WD 500 µm
25.0 kV 3.0 50x SE 18.0 UFSCar - DEMa - LCE - FEG
e)
Acc.V Spot Magn Det WD 1 mm
25.0 kV 3.0 30x SE 19.0 UFSCar - DEMa - LCE - FEG
f)
Acc.V Spot Magn Det WD 200 µm
25.0 kV 3.0 100x SE 19.0 UFSCar - DEMa - LCE - FEG
g)
Acc.V Spot Magn Det WD 200 µm
25.0 kV 3.0 100x SE 19.6 UFSCar - DEMa - LCE - FEG
h)
Acc.V Spot Magn Det WD 50 µm
25.0 kV 3.0 500x SE 19.6 UFSCar - DEMa - LCE - FEG

Figure 5.33 - Fatigue fracture characteristics and crack propagation in Eyebrow fracture indicating a) Multiple crack nucleation, b) crack propagation in thickness direction (TMAZ/SZ interface) of the upper sheet, c) d) e) f) presence of steps and fatigue striation along the transition from nugget region to base material and g) h) failure mechanism transition from fatigue striation to shear lips. (black arrows indicate propagation direction and red arrows indicate cracks nucleation)

Multiple crack nucleation in the hook region (by the edge of the weld nugget) and fatigue striations in direction of the upper sheet thickness (between TMAZ and SZ) were identified by observations of the Figure 5.33 (a). Figure 5.33 (b) illustrates the cracks propagation in thickness direction (TMAZ/SZ interface) of the upper sheet. Figure 5.33 (c) (d), (e) and (f) show the presence of steps and fatigue striation marks along the transition from the nugget region to the base material region in width direction, in both sides of the nugget weld. The same pattern of fatigue striations remain unchanged until crack propagation reaches regions close to the ones indicated in Figure 5.33 (g) and (h), where a different sign of fatigue striations and dimples are observed, respectively. This fracture behavior on the last region is described as shear lips, where fracture occurs in a 45^{o} angle in relation to the fatigue fracture propagation plane and presents ductile behavior.

The mechanisms and characteristics of the Eyebrow fracture observed in this work are quite similar to previous works observations and explanations [18,35,80,81].

Figure 5.34 shows the surface fatigue fracture produced by flat hook sample in a low-cycle load condition. It is observed the presence of a secondary crack in thickness direction, between SZ and TMAZ, close to hook region. This crack might have grown until a critical size, resulting in a small resistance area and intensifying the load at the hook tip region. Therefore, when the resistance area was too small, the joint could not withstand the overstress, and the spot-weld catastrophic failed through the weld. This hypothesis is supported by SEM analysis from regions (a-d) in the fracture surface, since no fatigue striations were found and signs of cleavage and plastic deformation (dimples) were identified as

illustrated in Figure 5.35. Although some works also support these explanations with similar conclusions [35,79,81], further examinations are needed in future works to confirm these assumptions.

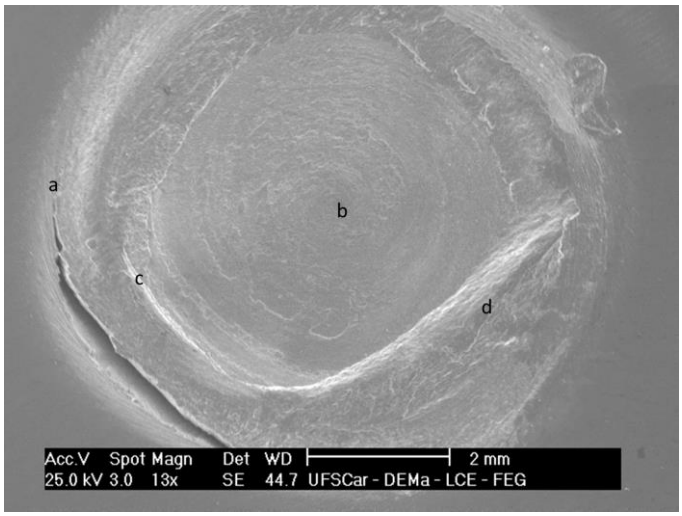

Figure 5.34 - Fatigue fracture surface of flat hook specimen obtained in low-cycle load conditions.

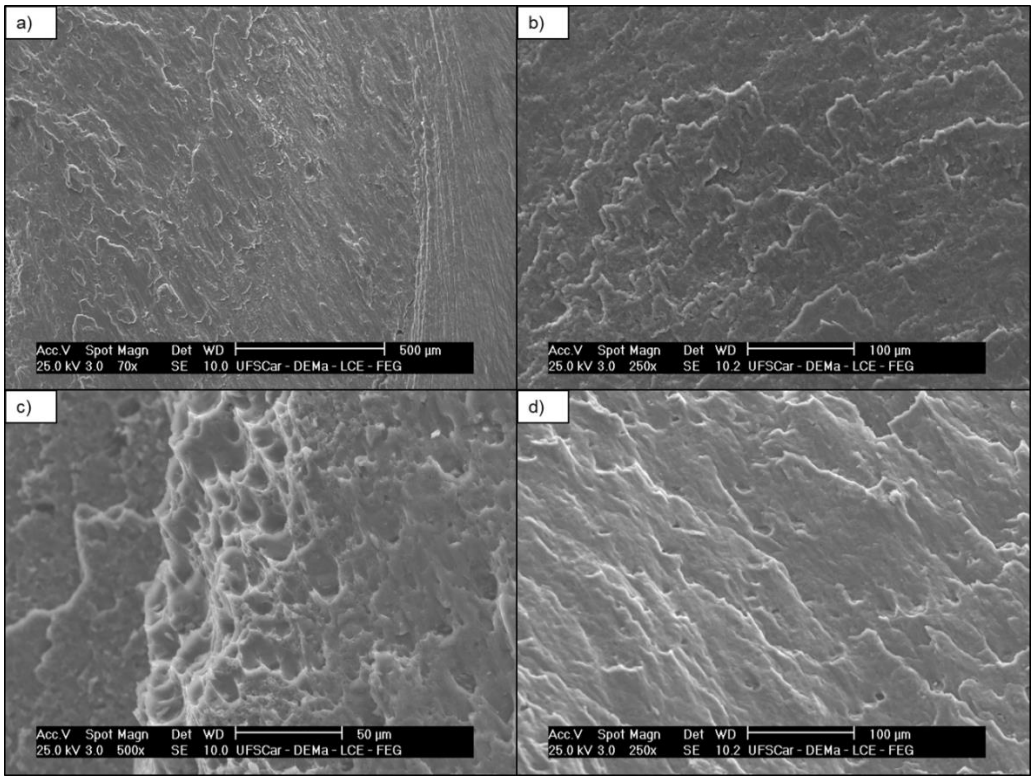

Figure 5.35 - Fracture characteristics from flat hook specimen exhibiting a),b) cleavage, c) dimples and d) cleavage.

Figure 5.36 (a) shows the fatigue fracture surface produced by hook tip pointing up sample in a low-cycle load condition. Similar to flat hook condition, the presence of a secondary crack in thickness direction was also observed, but towards the base material. The same hypothesis of this secondary crack growth up to a critical size, resulting in a spot-weld catastrophic failure due to overstress in hook region is also reasonable. However, since the hook pointing up causes a stress concentration in direction of SZ and TMAZ region, when the sample was overloaded the crack propagated by SZ region in a 45º angle up to sheet thickness. SEM analysis of regions (b-d) in the fracture surface showed no fatigue striations signs. Nonetheless, signs of cleavage and plastic deformation (dimples) was observed as shown in Figure 5.36 (b), (c) and (d).

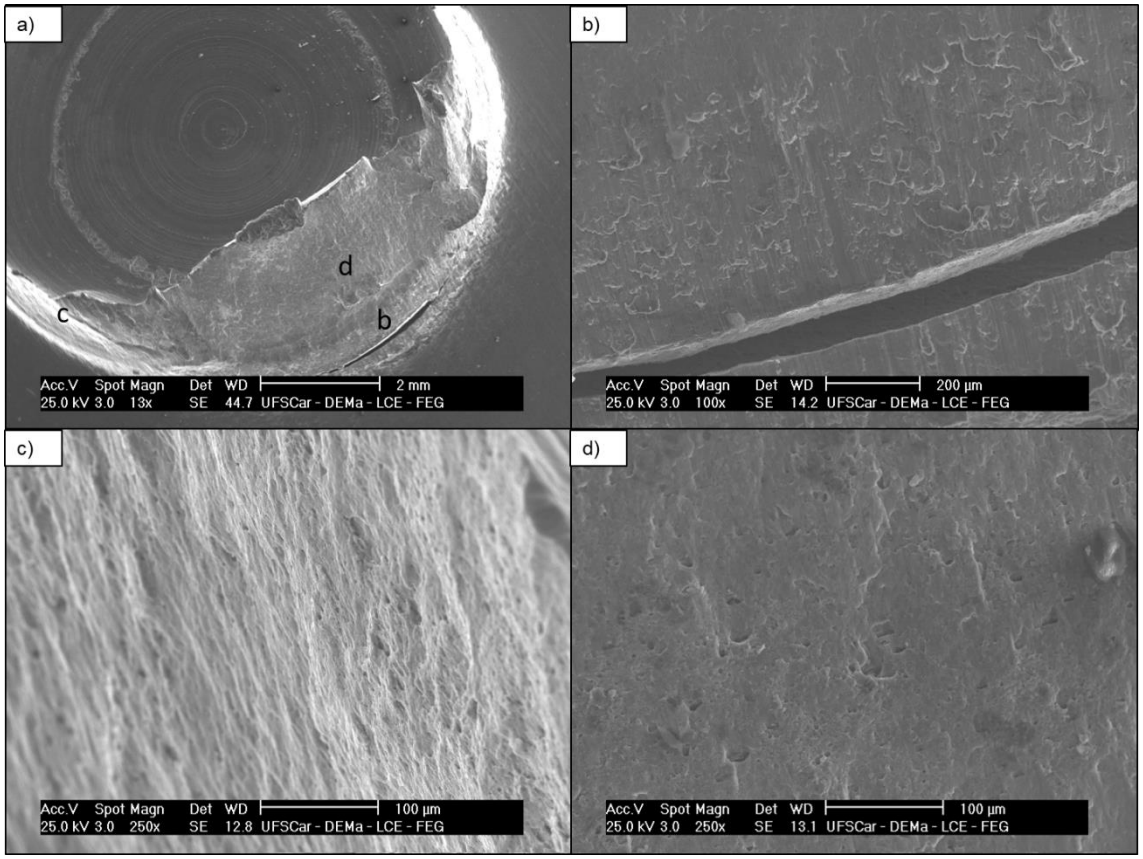

Figure 5.36 - a) Fatigue fracture surface of hook pointing up specimen obtained in low-cycle load conditions b),c) and d) fracture characteristics indicating the presence of cleavage and dimples in the fractured surface.

Since for hook pointing down condition the fatigue fracture for low-cycle load conditions took place pulling-out the nugget from both plates, the surface analyzed was from the nugget region as illustrated in Figure 5.37. Comparing this fracture with previous works observations, several similarities are identified with fractures observed by Effertz and Brzostek [35,80]. For example, cracks nucleation near the hook region, fatigue striation signs in TMAZ/SZ region, signs of sliding near the edge of the nugget top region, signs of cleavage in the other areas of the interface TMAZ/SZ and the presence of dimples also indicating some level of plastic deformation. These features are presented in the regions a-d in Figure 5.38.

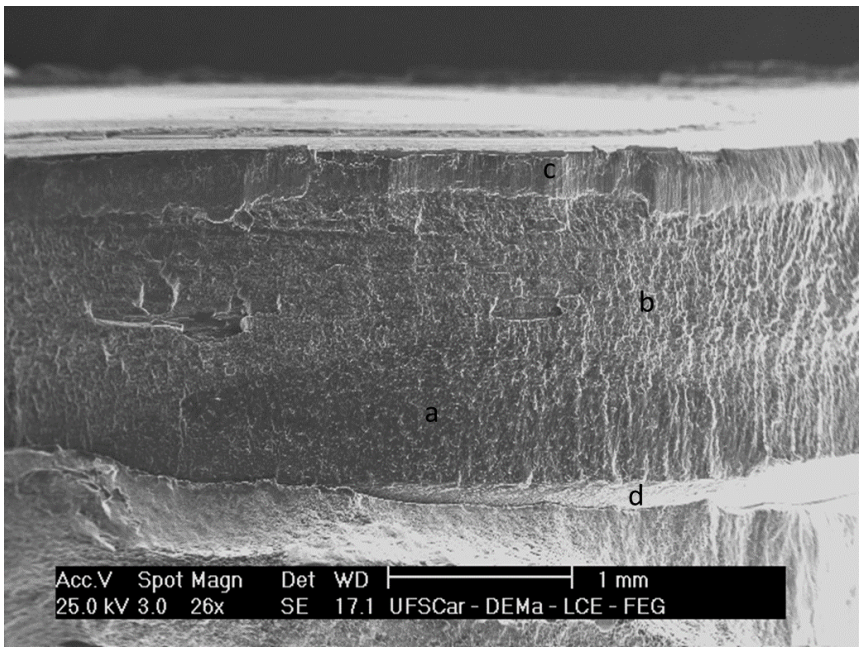

Figure 5.37 - Fatigue fracture surface from hook pointing down condition tested in low-cycle load condition.

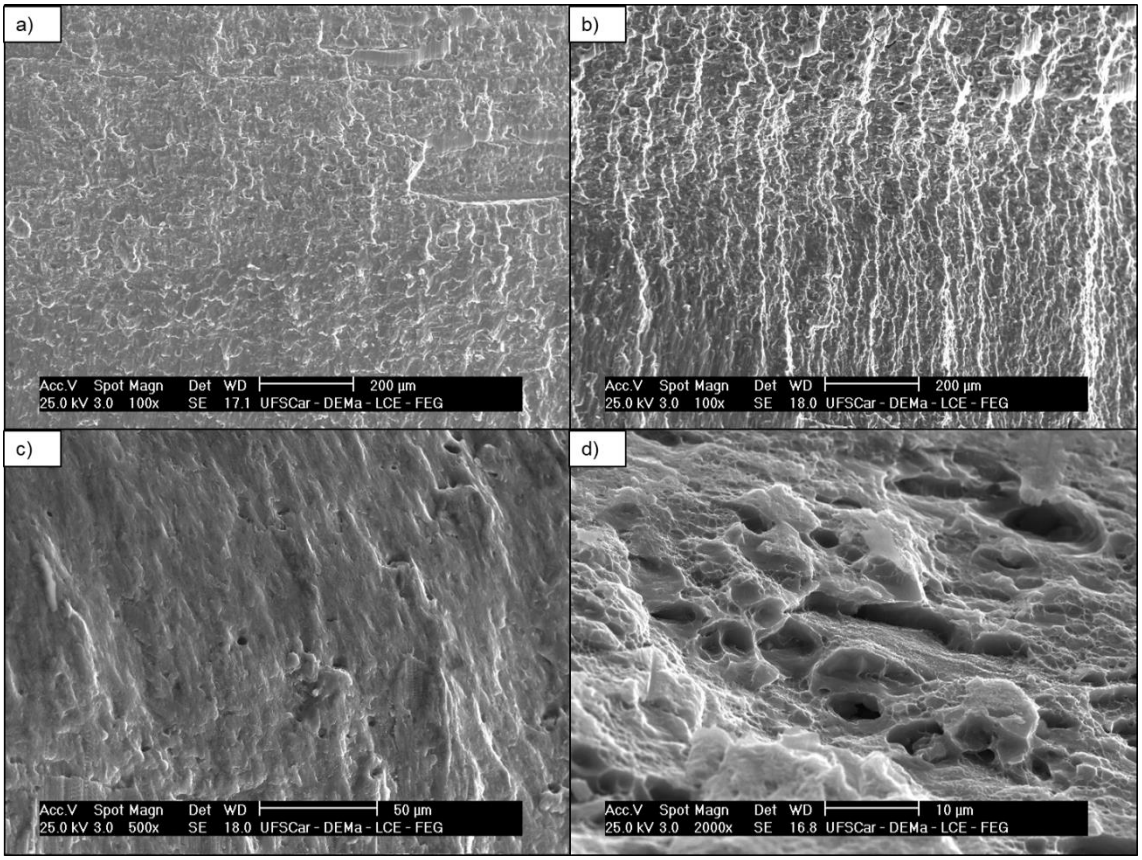

Figure 5.38 - Fracture characteristics from hook pointing down specimen exhibiting a) b) fatigue striation, c) cleavage and d) dimples.

In comparison with hook pointing up condition, although hook pointing down favors PO fracture, the fact of hook tip shape presents a lower level of stress concentration in direction of TMAZ/HAZ interface, could favor some crack propagation through the sheet thickness in the lower sheet (base material). Considering the different fractures behavior presented in Figure 5.38, it is also reasonable to assume that the same mechanism of crack initiation found in EB occurred in this case, but as long the crack reached a critical size, the overstress in hook regions allowed PO fracture in a catastrophic manner pulling-out the nugget from both plates. Again, although some evidence in previous works [35,79,80] support these theories, a more detailed explanation and further investigation are necessary to confirm all these assumptions.

Finally, it is important mentioning that all samples were bake hardened. Therefore, considering the effect of this treatment in SZ and HAZ region, it is

possible that fracture mechanisms through the interface were less likely to occur than fracture mechanisms through the interface of HAZ/SZ region. For example, hook pointing down have not presented any fracture through SZ region, although hook shape is connected to Bonding Ligament, which is expected to be a susceptible region to fatigue crack propagation. Another evidence is that flat hook configuration has presented fatigue life similar to the other two configurations. Without Bake Hardening treatment, the flat hook configuration showed lower static mechanical properties than hook pointing down and hook pointing up conditions, whereas with Bake Hardening the level of shear strength of the three configurations were similar. Thus, the same improvement could occur in fatigue solicitations. Hence, evaluating the effect of hook shape in fatigue properties and fracture behavior without Bake Hardening may be interesting for future works.

6 CONCLUSIONS

Considering the main objectives of this work, the following conclusions were drawn:

- An optimized process parameters set was obtained (PD:2.1 mm, FR:3.9 mm/s and RS:2700 rpm), which resulted in maximum Shear and Peel Load of 8.5±0.3 kN and 1.3±0.1 kN respectively. Additionally, the welding time obtained in this condition was 1.08±0.01 s, which is suitable to automotive applications. In agreement with previous works, Plunge Depth showed a more relevant effect on weld strength considering a confidence level of 94% in the range of values tested.
- Feeding Rate and Rotational Speed showed small influence on the macrostructure features evaluated. On contrary, changing Plunge Depth values, three hook shapes were formed (low PD - flat hook; intermediate PD - hook pointing down; high PD - hook pointing up), which was a result of the formation of a material flow around the sleeve and the drop region.
- For low values of Plunge Depth, Through the Weld fracture was favored due to flat hook formation and for high values of Plunge Depth, nugget Pull-Out fracture was favored due to hook pointing up formation. Intermediate values of Plunge Depth presents both types of failure modes and maximizes the weld strength because of hook pointing down formation.
- Bake Hardening treatment increases the SZ hardness by reprecipitation process and reduces the HAZ hardness by coarsening process. Nevertheless, Bake Hardening treatment improved only the strength of welds presenting flat hook configuration, which fracture propagation occurs through the SZ region.
- L-N curves for the three hook configurations demonstrated similar trend. Fatigue limit values were found at 12% of the ultimate maximum shear load levels in agreement to previous works. Through the Weld fracture was related to flat hook configurations, Pull-Out from one plate was related to hook pointing up configuration and Pull-Out from both plates was related to hook pointing down configuration. But this behavior was identified only for low-cycle load conditions. For high-cycle load conditions, all the specimens showed the same failure mode (Eyebrow fracture) regardless the hook configurations. Crack initiation starts on

hook region and depending on hook shape and on the level of overstress reached (due to crack size) the fracture might catastrophically occurs Through the Weld or by Pulling-Out the nugget. If the weld does not reach a critical level of overstress, fatigue cracks propagates throughout the thickness of the nugget (TMAZ/SZ interface) and by the width of the base material region in a non-catastrophic behavior resulting in the Eyebrow fracture.

7 SUGGESTIONS FOR FUTURE WORKS

Although a satisfactory evaluation of RFSSW welds of AA6082-T6 for automotive applications was successfully achieved, additional analysis are proposed to have a more comprehensive investigation.

- To evaluate the mechanical properties and structural characteristics of joints with similar and dissimilar combinations of other aluminum alloys or/with steel alloys, considering the same approach of welding times suitable in automotive industry.
- Developing and optimizing tool design in order to change material flow around the sleeve and control hook shape and, consequently, improving mechanical properties.
- Investigating reprecipitation and overaging process in different weld regions after Bake Hardening using Transmission Electron Microscope (TEM) and tomography techniques as 3DAP.
- To carry out statistical analysis of the individual effect of feeding rate and rotational speed parameters in fatigue properties and fatigue fracture behavior and determine a possible combined effect of more than one parameter at a time. Optimizing process parameters to maximize fatigue properties.
- Investigating the fatigue fracture mechanisms under low-cycle load conditions for the different conditions analyzed in this work.

8 REFERENCES

[1] S.J. Doshi, A.V. Gohil, N.D. Mehta, S.R. Vaghasiya, Challenges in Fusion Welding of Al alloy for Body in White, Mater. Today Proc. 5 (2018) 6370–6375. doi:10.1016/j.matpr.2017.12.247.

[2] W.S. Miller, L. Zhuang, J. Bottema, A.J. Wittebrood, P. De Smet, A. Haszler, A. Vieregge, Recent development in aluminium alloys for the automotive industry, Mater. Sci. Eng. A. 280 (2000) 37–49. doi:10.1016/S0921-5093(99)00653-X.

[3] European Aluminium Association, The Aluminum Automotive Manual: Car body – Body structures, 2013. http://www.alueurope.eu/wp-content/uploads/2011/12/1_AAM_Body-structures.pdf.

[4] M. Haghshenas, A.P. Gerlich, Joining of automotive sheet materials by friction-based welding methods: A review, Eng. Sci. Technol. an Int. J. 21 (2018) 130–148. doi:10.1016/j.jestch.2018.02.008.

[5] P. Briskham, N. Blundell, L. Han, R. Hewitt, K. Young, D. Boomer, Comparison of Self-Pierce Riveting, Resistance Spot Welding and Spot Friction Joining for Aluminium Automotive Sheet, 1 (2006) 774–786. doi:10.4271/2006-01-0774.

[6] U. Suhuddin, R. Mesquita, J.F. Santos, Friction Spot Welding of Similar Aluminum Alloys AA6082-T6 for Application in Automotive Industry, in: Int. Automot. Congr. - IABC, 2016.

[7] H. Li, Z. Yan, L. Cao, Bake hardening behavior and precipitation kinetic of a novel Al-Mg-Si-Cu aluminum alloy for lightweight automotive body, Mater. Sci. Eng. A. 728 (2018) 88–94. doi:10.1016/j.msea.2018.05.014.

[8] A. Cuniberti, A. Tolley, M.V.C. Riglos, R. Giovachini, Influence of natural aging on the precipitation hardening of an AlMgSi alloy, Mater. Sci. Eng. A. 527 (2010) 5307–5311. doi:10.1016/j.msea.2010.05.003.

[9] J.Y. Cao, M. Wang, L. Kong, L.J. Guo, Hook formation and mechanical properties of friction spot welding in alloy 6061-T6, J. Mater. Process. Technol. 230 (2016) 254–262. doi:10.1016/j.jmatprotec.2015.11.026.

[10] Ľ. Kaščák, E. Spišák, Mechanical Joining Methods in Car Body Construction, Transf. Inovácií. 28 (2013) 168–171.

[11] European Aluminium Association, The Aluminium Automotive Manual – Joining, 2015. http://european-aluminium.eu/wp-content/uploads/2015/01/9-Joining_2015.pdf.

[12] A. Kumar, S.S. Gautam, Heat Input & Joint Efficiency of Three Welding Processes TIG , MIG and FSW Using AA6061, Int. J. Mech. Eng. Robot. Res. 1 (2014) 89–94.

[13] American Welding Society, AWS D8.2M:2017 Specification for Automotive Weld Quality- Resistance Spot Welding of aluminium, 2017.

[14] X.J. Wang, X.L. Wang, Z.K. Zhang, W.X. Jing, Comparison of Properties on Withdrawing and Refill Friction Stir Spot Welding Joints, Appl. Mech. Mater. 633 (2014) 601–606. doi:10.4028/www.scientific.net/AMM.633-634.601.

[15] C. Schilling, J.F. Dos Santos, Method and device for joining at least two adjoining work pieces by friction welding. US 6722556 B2, 2004.

[16] Z. Xu, Z. Li, S. Ji, L. Zhang, Refill friction stir spot welding of 5083-O aluminum alloy, J. Mater. Sci. Technol. 34 (2018) 878–885. doi:10.1016/j.jmst.2017.02.011.

[17] T. Rosendo, B. Parra, M.A.D. Tier, A.A.M. Silva, J.F. Santos, T.R. Strohaecker, N.G. Alcântara, Mechanical and microstructural investigation of friction spot welded AA6181-T4 aluminium alloy, Mater. Des. 32 (2011) 1094–1100. doi:10.1016/j.matdes.2010.11.017.

[18] S.B.M. Lage, C. Bolfarini, Otimização dos parâmetros de soldagem a ponto por fricção (FSpW) da Liga AlMgSc e avaliação das propriedades mecânicas estáticas e dinâmicas. Dissertação (Mestrado em Engenharia) - Departamento de Engenharia de Materiais, Universidade Federal de São Carlos, 2017.

[19] G. Zhang, L. Zhang, C. Kang, J. Zhang, Development of friction stir spot brazing (FSSB), Mater. Des. 94 (2016) 502–514. doi:10.1016/j.matdes.2016.01.057.

[20] M.D. Tier, T.S. Rosendo, J.F. Santos, N. Huber, J.A. Mazzaferro, C.P. Mazzaferro, T.R. Strohaecker, The influence of refill FSSW parameters on the microstructure and shear strength of 5042 aluminium welds, J. Mater. Process. Technol. 213 (2013) 997–1005. doi:10.1016/j.jmatprotec.2012.12.009.

[21] Z. Shen, Y. Ding, O. Gopkalo, B. Diak, A.P. Gerlich, Effects of tool design on the microstructure and mechanical properties of refill friction stir spot welding of dissimilar Al alloys, J. Mater. Process. Tech. 252 (2018) 751–759. doi:10.1016/j.jmatprotec.2017.10.034.

[22] L.C. Campanelli, N.G. Alcântara, J.F. Santos, Soldagem por Ponto no Estado Sólido de Ligas Leves, Soldag. Insp. São Paulo. 16 (2011) 301–307.

[23] L.C. Campanelli, U.F.H. Suhuddin, A.I.S. Antonialli, J.F. Santos, N.G. Alcântara, C. Bolfarini, Metallurgy and mechanical performance of AZ31 magnesium alloy friction spot welds, J. Mater. Process. Tech. 213 (2013) 515–521. doi:10.1016/j.jmatprotec.2012.11.002.

[24] Z. Shen, Y. Chen, J.S.C. Hou, X. Yang, A.P. Gerlich, Influence of processing parameters on microstructure and mechanical performance of refill friction stir spot welded 7075-T6 aluminium alloy, Sci. Technol. Weld. Join. 20 (2015) 48–57. doi:10.1179/1362171814Y.0000000253.

[25] P.A.F. Barros, L.C. Campanelli, N.G. Alcântara, J.F. Santos, An

investigation on friction spot welding of AA2198-T8 thin sheets, Fatigue Fract. Eng. Mater. Struct. 00 (2016) 1–8. doi:10.1111/ffe.12512.

[26] C.C. Castro, A.H. Plaine, G.P. Dias, N.G. Alcântara, J.F. Santos, Investigation of geometrical features on mechanical properties of AA2198 refill friction stir spot welds, J. Manuf. Process. 36 (2018) 330–339. doi:10.1016/j.jmapro.2018.10.027.

[27] M.J. Starink, A. Deschamps, S.C. Wang, The strength of friction stir welded and friction stir processed aluminium alloys, Scr. Mater. 58 (2008) 377–382. doi:10.1016/j.scriptamat.2007.09.061.

[28] American Welding Society, AWS D17.2 - Specification for Resistance Welding for Aerospace Applications, 2013.

[29] L. Fratini, A. Barcellona, G. Buffa, D. Palmen, Friction stir spot welding of AA6082-T6: Influence of the most relevant process parameters and comparison with classic mechanical fastening techniques, J. Eng. Manuf. 221 (2007) 1111–1118. doi:10.1243/09544054JEM678.

[30] J.Y. Cao, M. Wang, L. Kong, H.X. Zhao, P. Chai, Microstructure, texture and mechanical properties during refill friction stir spot welding of 6061-T6 alloy, Mater. Charact. 128 (2017) 54–62. doi:10.1016/j.matchar.2017.03.023.

[31] J. Shen, S.B.M. Lage, U.F.H. Suhuddin, C. Bolfarini, J.F. Santos, Texture Development and Material Flow Behavior During Refill Friction Stir Spot Welding of AlMgSc, Metall. Mater. Trans. A. 49 (2018) 241–254. doi:10.1007/s11661-017-4381-6.

[32] M. Sajed, Parametric study of two-stage refilled friction stir spot welding, J. Manuf. Process. 24 (2016) 307–317. doi:10.1016/j.jmapro.2016.09.011.

[33] M. Reimann, J. Goebel, J.F. Santos, Microstructure Evolution and Mechanical Properties of Keyhole Repair Welds in AA 2219-T851 Using Refill Friction Stir Spot Welding, J. Mater. Eng. Perform. 27 (2018) 5220–5226. doi:10.1007/s11665-018-3519-z.

[34] H. Badarinarayan, Y. Shi, X. Li, K. Okamoto, Effect of tool geometry on hook formation and static strength of friction stir spot welded aluminum 5754-O sheets, Int. J. Mach. Tools Manuf. 49 (2009) 814–823. doi:10.1016/j.ijmachtools.2009.06.001.

[35] R.C. Brzostek, U.F.H. Suhuddin, J.F. Santos, Fatigue assessment of refill friction stir spot weld in AA 2024 - T3 similar joints, Fatigue Fract. Eng. Mater. Struct. 41 (2018) 1208–1223. doi:10.1111/ffe.12764.

[36] S. Bag, D.V. Kiran, A.A. Syed, A. De, Efficient Estimation of Volumetric Heat Source in Fusion Welding Process Simulation, Weld. World. 56 (2013) 88–97. doi:10.1007/BF03321399.

[37] T.S. Rosendo, T.R. Strohaecker, J.F. Santos, Estudo do Desempenho Mecânico de Solda(S) Ponto Por Fricção (FSpW) da Liga AA6181-T4.

Tese (Doutorado em Engenharia) - Departamento de Metalurgia da Escola de Engenharia da UFRGS, Universidade Federal do Rio Grande do Sul, 2009.

[38] P. Su, A. Gerlich, T.H. North, G.J. Bendzsak, Energy utilisation and generation during friction stir spot welding, Sci. Technol. Weld. Join. 11 (2006) 163–169. doi:10.1179/174329306X84373.

[39] P. Su, A. Gerlich, T.H. North, G.J. Bendzsak, Energy Generation and Stir Zone Dimensions in Friction Stir Spot Welds, SAE Tech. Pap. 01 (2006) 971–980. doi:10.4271/2006-01-0971.

[40] Z. Shen, Y. Ding, O. Gopkalo, B. Diak, A.P. Gerlich, Effects of tool design on the microstructure and mechanical properties of refill friction stir spot welding of dissimilar Al alloys, J. Mater. Process. Technol. 252 (2018) 751–759. doi:10.1016/j.jmatprotec.2017.10.034.

[41] S.T. Amancio, A.P.C. Camillo, L. Bergmann, J.F. Santos, S.E. Kury, N.G. Alcântara, Preliminary Investigation of the Microstructure and Mechanical Behaviour of 2024 Aluminium Alloy Friction Spot Welds, Mater. Trans. 52 (2011) 985–991. doi:10.2320/matertrans.L-MZ201126.

[42] C.C. Castro, A.H. Plaine, N.G. Alcântara, J.F. Santos, Taguchi approach for the optimization of refill friction stir spot welding parameters for AA2198-T8 aluminum alloy, Int. J. Adv. Manuf. Technol. 99 (2018) 1927–1936. doi:10.1007/s00170-018-2609-2.

[43] A.H. Plaine, A.R. Gonzalez, U.F.H. Suhuddin, J.F. Santos, N.G. Alcântara, The optimization of friction spot welding process parameters in AA6181-T4 and Ti6Al4V dissimilar joints, Mater. Des. 83 (2015) 36–41. doi:10.1016/j.matdes.2015.05.082.

[44] J.A. Österreicher, N.P. Papenberg, M. Kumar, D. Ma, S. Schwarz, C.M. Schlögl, Quantitative prediction of the mechanical properties of precipitation-hardened alloys with special application to Al–Mg–Si, Mater. Sci. Eng. A. 703 (2017) 380–385. doi:10.1016/j.msea.2017.07.080.

[45] Y. Birol, DSC analysis of the precipitation reactions in the alloy AA6082 - Effect of sample preparation, J. Therm. Anal. Calorim. 83 (2006) 219–222.

[46] J. Osten, B. Milkereit, C. Schick, O. Kessler, Dissolution and Precipitation Behaviour during Continuous Heating of Al–Mg–Si Alloys in a Wide Range of Heating Rates, Materials (Basel). 8 (2015) 2830–2848. doi:10.3390/ma8052830.

[47] N. Wanderka, N. Lazarev, C.S.T. Chang, J. Banhart, Analysis of clustering in Al-Mg-Si alloy by density spectrum analysis of atom probe data, Ultramicroscopy. 111 (2011) 701–705. doi:10.1016/j.ultramic.2010.11.022.

[48] M. Murayama, K. Hono, Pre-Precipitate clusters and precipitation process in Al-Mg-Si alloys, Acta Mater. 47 (1998) 1537–1548. doi:10.1016/S1359-

6454(99)00033-6.

[49] C.D. Marioara, S.J. Andersen, J. Janses, H.W. Zandbergen, Atomic model for GP-Zones in a 6082 Al-Mg-Si system, Acta Mater. 49 (2001) 321–328. doi:10.1016/S1359-6454(00)00302-5.

[50] M.A. van Huis, J.H. Chen, H.W. Zandbergen, M.H.F. Sluiter, Phase stability and structural relations of nanometer-sized, matrix-embedded precipitate phases in Al-Mg-Si alloys in the late stages of evolution, Acta Mater. 54 (2006) 2945–2955. doi:10.1016/j.actamat.2006.02.034.

[51] G.A. Edwards, K. Stiller, G.L. Dunlop, M.J. Couper, The Precipitation Sequence in Al-Mg-Si Alloys, Acta Mater. 46 (1998) 3893–3904. doi:10.1016/S1359-6454(98)00059-7.

[52] S. Pogatscher, H. Antrekowitsch, H. Leitner, T. Ebner, P.J. Uggowitzer, Mechanisms controlling the artificial aging of Al – Mg – Si Alloys, Acta Mater. 59 (2011) 3352–3363. doi:10.1016/j.actamat.2011.02.010.

[53] J.K. Sunde, C.D. Marioara, A.T.J. Van Helvoort, R. Holmestad, The evolution of precipitate crystal structures in an Al-Mg-Si (-Cu) alloy studied by a combined HAADF-STEM and SPED approach, Mater. Charact. 142 (2018) 458–469. doi:10.1016/j.matchar.2018.05.031.

[54] S.J. Andersen, H.W. Zandbergen, J. Janses, The crystal structure of the beta'' phase in Al-Mg-Si alloys, Acta Mater. 46 (1998) 3283–3298. doi:10.1016/S1359-6454(97)00493-X.

[55] M. Murayama, K. Hono, M. Saga, M. Kikuchi, Atom probe studies on the early stages of precipitation in Al-Mg-Si alloys, Mater. Sci. Eng. A. 250 (1998) 127–132. doi:10.1016/S0921-5093(98)00548-6.

[56] AALCO, Aluminium Alloy Specifications, 2018. www.aalco.co.uk (accessed February 18, 2019).

[57] S. Jadhav, P. Vinayak, S. Rajkumar, Influence of Heat Treatment on Mechanical Properties and Microstructure of EN AW 6082 Aluminum alloy, in: Int. Conf. Mech. Aerosp. Eng., 2017: pp. 184–187.

[58] A. Deschamps, G. Martin, R. Dendievel, H.P. Van Landeghem, Lighter structures for transports : The role of innovation in metallurgy, Comptes Rendus Phys. 18 (2017) 445–452. doi:10.1016/j.crhy.2017.09.006.

[59] G. Yılmazoğlu, E. Doruk, Z. Ayaz, T. Başer, İ. Durgun, The Effect of Heat Treatment Parameters on the Mechanical Properties and Crashworthiness of AA6082 Extruded Profiles, 8th Int. Conf. Exhib. Des. Prod. Mach. DIES/MOLDS. (2015) 257–260.

[60] A.P. Mouritz, chapter 4: Strengthening of metal alloys, in: Introd. to Aerosp. Mater., Woodhead Publishing limited, Cambridge, 2012.

[61] M.S. Weglowski, Friction stir processing – State of the art, Arch. Civ. Mech. Eng. 8 (2017) 114–129. doi:10.1016/j.acme.2017.06.002.

[62] M.N. Avettand-Fènoel, F. Geuser, A. Deschamps, Effect of the ageing on precipitation spatial distribution in stationay shoulder friction stir welded AA2050 alloys, Mater. Charact. 154 (2019) 193–199. doi:10.1016/j.matchar.2019.06.006.

[63] M. Reimann, Keyhole repair in precipitation hardening aluminum alloys using refill friction stir spot welding. Thesis (Engineering Phd) -, Universitat Hamburg, 2018.

[64] R.S. Mishra, Z.Y. Ma, Friction stir welding and processing, Mater. Sci. Eng. R. 50 (2005) 1–78. doi:10.1016/j.mser.2005.07.001.

[65] I. Vysotskiy, S. Malopheyev, S. Rahimi, S. Mironov, R. Kaibyshev, Unusual fatigue behavior of friction-stir welded Al–Mg–Si alloy, Mater. Sci. Eng. A. 760 (2019) 277–286. doi:10.1016/j.msea.2019.06.005.

[66] O. Gopkalo, X. Liu, F. Long, M. Booth, A.P. Gerlich, B.J. Diak, Non-isothermal thermal cycle process model for predicting post-weld hardness in friction stir welding of dissimilar age-hardenable aluminum alloys, Mater. Sci. Eng. A. 754 (2019) 205–215. doi:10.1016/j.msea.2019.03.025.

[67] A.H. Baghdadi, A. Rajabi, N.F.M. Selamat, Z. Sajuri, M.Z. Omar, Effect of post-weld heat treatment on the mechanical behavior and dislocation density of friction stir welded Al6061, Mater. Sci. Eng. A. 754 (2019) 728–734. doi:10.1016/j.msea.2019.03.017.

[68] Y. Huang, Y. Xie, X. Meng, J. Li, Atypical grain coarsening of friction stir welded AA6082-T6: Characterization and modeling, Mater. Sci. Eng. A. 740–741 (2019) 211–217. doi:10.1016/j.msea.2018.10.109.

[69] S. Chen, X. Li, X. Jiang, T. Yuan, Y. Hu, The effect of microstructure on the mechanical properties of friction stir welded 5A06 Al Alloy, Mater. Sci. Eng. A. 735 (2018) 382–393. doi:10.1016/j.msea.2018.08.020.

[70] S. Palanivel, A. Arora, K.J. Doherty, R.S. Mishra, A framework for shear driven dissolution of thermally stable particles during friction stir welding and processing, Mater. Sci. Eng. A. 678 (2016) 308–314. doi:10.1016/j.msea.2016.10.015.

[71] S.S. Malopheyev, I. Vysotskiy, V. Kulitskiy, S. Mironov, Optimization of processing-microstructure-properties relationship in friction-stir welded 6061-T6 aluminum alloy, Mater. Sci. Eng. A. 662 (2016) 136–143. doi:10.1016/j.msea.2016.03.063.

[72] P. Dong, D. Sun, H. Li, Materials Science & Engineering A Natural aging behaviour of friction stir welded 6005A-T6 aluminium alloy, Mater. Sci. Eng. A. 576 (2013) 29–35. doi:10.1016/j.msea.2013.03.077.

[73] A. Simar, Y. Bréchet, B. De Meester, A. Denquin, C. Gallais, T. Pardoen, Integrated modeling of friction stir welding of 6xxx series Al alloys: Process, microstructure and properties, Prog. Mater. Sci. 57 (2012) 95–183. doi:10.1016/j.pmatsci.2011.05.003.

[74] J. Ha, M. Baral, Y.P. Korkolis, Plastic anisotropy and ductile fracture of bake-hardened AA6013 aluminum sheet, Int. J. Solids Struct. 155 (2018) 123–139. doi:10.1016/j.ijsolstr.2018.07.015.

[75] R.A. Akl, D. Mohr, Paint-bake effect on the plasticity and fracture of pre-strained aluminum 6451 sheets, Int. J. Mech. Sci. 124–125 (2017) 68–82. doi:10.1016/j.ijmecsci.2017.01.002.

[76] Y. Weng, Z. Jia, L. Ding, M. Liu, X. Wu, Q. Liu, Combined effect of pre-aging and Ag/Cu addition on the natural aging and bake hardening in Al-Mg-Si alloys, Prog. Nat. Sci. Mater. Int. 28 (2018) 363–370. doi:10.1016/j.pnsc.2018.04.007.

[77] K. Dehghani, Bake hardening of nanograin AA7075 aluminum alloy, Mater. Sci. Eng. A. 530 (2011) 618–623. doi:10.1016/j.msea.2011.10.031.

[78] H. Alihosseini, M.A. Zaeem, K. Dehghani, G. Faraji, Producing high strength aluminum alloy by combination of equal channel angular pressing and bake hardening, Mater. Lett. 140 (2014) 196–199. doi:10.1016/j.matlet.2014.10.163.

[79] Z. Shen, Y. Ding, J. Chen, A.P. Gerlich, Comparison of fatigue behavior in Mg/Mg similar and Mg/steel dissimilar refill friction stir spot welds, Int. J. Fatigue. 92 (2016) 78–86. doi:10.1016/j.ijfatigue.2016.06.033.

[80] P.S. Effertz, V. Infante, L. Quintino, U. Suhuddin, S. Hanke, J.F. Santos, Fatigue life assessment of friction spot welded 7050-T76 aluminium alloy using Weibull distribution, Int. J. Fatigue. 87 (2016) 381–390. doi:10.1016/j.ijfatigue.2016.02.030.

[81] A.H. Plaine, U.F.H. Suhuddin, N.G. Alcântara, J.F. Santos, Fatigue behavior of friction spot welds in lap shear specimens of AA5754 and Ti6Al4V alloys, Int. J. Fatigue. 91 (2016) 149–157. doi:10.1016/j.ijfatigue.2016.06.005.

[82] S.L.C. Ferreira, R.E. Bruns, E.G.P. da Silva, W.N.L. dos Santos, C.M. Quintella, J.M. David, J.B. de Andrade, M.C. Breitkreitz, I.C.S.F. Jardim, B.B. Neto, Statistical designs and response surface techniques for the optimization of chromatographic systems, J. Chromatogr. A. 1158 (2007) 2–14. doi:10.1016/j.chroma.2007.03.051.

[83] H. Tye, Application of statistical “design of experiments” methods in drug discovery, Drug Discov. Today. 9 (2004) 485–491. doi:10.1016/S1359-6446(04)03086-7.

[84] M.A. Bezerra, R.E. Santelli, E.P. Oliveira, L.S. Villar, L.A. Escaleira, Response surface methodology (RSM) as a tool for optimization in analytical chemistry, Talanta. 76 (2008) 965–977. doi:10.1016/j.talanta.2008.05.019.

[85] V. Czitrom, One-Factor-at-a-Time Versus Designed Experiments, Am. Stat. 53 (1999) 126–131.

[86] P.J. Davis, Leonhard Euler’s integral: A Historical profile of the Gamma Function, Natl. Bur. Stand. Washington, D. C. (1959) 849–869.

[87] B. Silva, G. Zepon, B.S. Oliveira, Otimização de parâmetros de processo de soldas híbridas de AA6082-T6 com adesivo estrutural para a indústria automotiva. Monografia (Bacharelado em Engenharia) - Departamento de Engenharia de Materiais, Universidade Federal de São Carlos, 2018.

SUPPLEMENTARY DATA

Table A – Shear optimization data from Box Behnken design experiments.

Sample	RS (rpm)	PD (mm)	FR (mm/s)	t (s)	Shear Strength (N)	Fracture type
BBD1	2200	2.2	4.5	2.0	5301.5	PO
BBD2	1800	1.8	4.0	1.9	4996.6	TW
BBD3	2200	2.2	3.5	2.3	8340.2	PO
BBD4	1800	2.0	4.5	1.9	5738.5	TW
BBD5	2600	2.0	4.5	1.9	7702.5	TW
BBD6	2200	2.0	4.0	2.0	7227.3	TW
BBD7	2200	2.0	4.0	2.0	7428.6	TW
BBD8	2600	1.8	4.0	1.9	5861.0	TW
BBD9	2600	2.0	3.5	2.1	7198.7	TW
BBD10	1800	2.2	4.0	2.1	8579.6	PO
BBD11	2200	1.8	4.5	1.8	5731.8	TW
BBD12	1800	2.0	3.5	2.1	6843.4	TW
BBD13	2200	1.8	3.5	2.0	6013.8	TW
BBD14	2600	2.2	4.0	2.1	8318.2	PO
BBD15	2200	2.0	4.0	2.0	6982.4	TW

Table B - Shear optimization data from complementary experiments expanding window of parameters values studied.

Sample	RS (rpm)	PD (mm)	FR (mm/s)	t (s)	Shear Strength (N)	Fracture type
BBD16	2200	2.1	3.5	2.2	8163.5	TW
BBD17	2200	2.3	3.5	2.3	6911.0	PO
BBD18	2200	2.1	4.0	2.1	7714.9	PO
BBD19	2200	2.3	4.0	2.2	7640.1	PO
BBD20	2200	2.2	3.0	2.5	7478.7	PO
BBD21	2200	2.3	3.0	2.5	7008.5	PO
BBD22	2200	2.1	3.0	2.4	7786.9	PO
BBD23	2200	2.2	4.0	2.1	7818.5	PO
BBD24	2000	2.2	4.0	2.1	8173.0	PO
BBD25	2400	2.2	4.0	2.1	7615.7	PO
BBD26	1700	2.2	3.8	2.2	7447.0	PO
BBD27	1500	2.2	3.8	2.2	6921.0	PO
BBD28	2800	2.2	3.8	2.2	8013.1	PO
BBD29	3000	2.2	3.8	2.2	8218.1	PO
BBD30	1800	2.2	4.0	2.1	7225.5	PO

BBD31	1800	2.2	4.0	2.1	7647.1	PO
BBD32	1800	2.2	4.0	2.1	7686.5	PO
BBD33	2900	2.1	3.9	2.1	8055.2	TW
BBD34	2900	2.1	3.9	2.1	8416.4	PO
BBD35	2900	2.1	3.9	2.1	8350.4	TW
BBD36	2200	2.2	3.5	2.3	7957.2	PO
BBD37	2200	2.2	3.5	2.3	7948.4	PO
BBD38	2600	2.2	4.0	2.1	8057.0	PO
BBD39	2600	2.2	4.0	2.1	7756.2	PO
BBD40	2000	2.2	4.0	2.1	7549.5	PO
BBD41	2000	2.2	4.0	2.1	7718.8	PO
BBD42	3000	2.2	3.8	2.2	7897.6	PO
BBD43	3000	2.2	3.8	2.2	7828.7	PO
BBD44	3000	2.1	4.0	2.1	7860.4	PO
BBD45	3000	2.1	4.0	2.1	7924.8	PO
BBD46	3000	2.1	4.0	2.1	8136.8	TW

Table C - Peel optimization data from Box Behnken design experiments.

Sample	PD (mm)	RS (rpm)	FR (mm/s)	Peel strength (N)	t (s)	Fracture type
BBD1	2.3	2300	3.9	896.1	1.2	PO
BBD2	2.3	2700	3.3	826.2	1.4	PO
BBD3	1.9	3100	3.9	937.5	1.0	TW
BBD4	2.1	2700	3.9	1254.8	1.1	PO
BBD5	2.3	3100	3.9	855.7	1.2	PO
BBD6	1.9	2700	3.3	1084.9	1.2	TW
BBD7	2.1	2700	3.9	1340.9	1.1	PO
BBD8	2.1	2700	3.9	1235.0	1.1	PO
BBD9	1.9	2300	3.9	879.6	1.0	TW
BBD10	2.1	3100	3.3	1246.2	1.3	PO
BBD11	2.3	2700	4.5	836.9	1.0	PO
BBD12	2.1	2300	3.3	1410.7	1.3	PO
BBD13	2.1	3100	4.5	1372.3	0.9	PO
BBD14	2.1	2300	4.5	1329.5	0.9	PO
BBD15	1.9	2700	4.5	1269.8	0.8	PO

Table D - Shear data optimization from OFAT experiments.

Sample	t (s)	RS (rpm)	PD (mm)	FR (mm/s)	Shear Load (N)	Fracture type
OFAT1	1.08	2700	2.1	3.9	8152	PO
	1.08	2700	2.1	3.9	8691	PO
	1.08	2700	2.1	3.9	8739	PO
OFAT2	1.08	2900	2.1	3.9	8471	TW
	1.08	2900	2.1	3.9	8340	TW
	1.08	2900	2.1	3.9	8067	TW
OFAT3	1.08	3100	2.1	3.9	8562	PO
	1.08	3100	2.1	3.9	8496	TW
	1.08	3100	2.1	3.9	8692	TW
OFAT4	0.97	2900	1.9	3.9	6565	TW
	0.97	2900	1.9	3.9	6489	TW
	0.97	2900	1.9	3.9	6560	TW
OFAT5	1.18	2900	2.3	3.9	7862	PO
	1.18	2900	2.3	3.9	8006	PO
	1.18	2900	2.3	3.9	7783	PO
OFAT6	1.24	2900	2.1	3.4	8579	PO
	1.24	2900	2.1	3.4	8081	TW
	1.24	2900	2.1	3.4	8601	TW
OFAT7	0.95	2900	2.1	4.4	8159	TW
	0.95	2900	2.1	4.4	7962	PO
	0.95	2900	2.1	4.4	7947	TW
OFAT8	1.08	2500	2.1	3.9	8518	TW
	1.08	2500	2.1	3.9	7462	TW
	1.08	2500	2.1	3.9	8093	PO
OFAT9	1.4	2900	2.1	3	8061	PO
	1.4	2900	2.1	3	7467	PO
	1.4	2900	2.1	3	7266	PO
OFAT10	1.03	2900	2	3.9	5836	TW
	1.03	2900	2	3.9	5891	TW
	1.03	2900	2	3.9	6705	TW
OFAT11	1.13	2900	2.2	3.9	7789	PO
	1.13	2900	2.2	3.9	7669	PO
	1.13	2900	2.2	3.9	7645	PO

Table E - Peel data optimization from OFAT experiments.

Sample	t (s)	RS (rpm)	PD (mm)	FR (mm/s)	Peel Strength (N)	Fracture type
OFAT1	1.1	2700	2.1	3.9	1340.9	PO
	1.1	2700	2.1	3.9	1235.0	PO
	1.1	2700	2.1	3.9	1254.8	PO
OFAT2	1.1	2300	2.1	3.9	1249.7	PO
	1.1	2300	2.1	3.9	1277.7	PO
	1.1	2300	2.1	3.9	924.9	TW
OFAT3	1.1	3100	2.1	3.9	1332.5	PO
	1.1	3100	2.1	3.9	1398.7	PO
	1.1	3100	2.1	3.9	1331.7	PO
OFAT4	1.0	2700	1.9	3.9	743.1	TW
	1.0	2700	1.9	3.9	705.8	TW
	1.0	2700	1.9	3.9	827.6	TW
OFAT5	1.2	2700	2.3	3.9	934.4	PO
	1.2	2700	2.3	3.9	1000.5	PO
	1.2	2700	2.3	3.9	911.2	PO
OFAT6	1.3	2700	2.1	3.3	1388.9	PO
	1.3	2700	2.1	3.3	1334.9	PO
	1.3	2700	2.1	3.3	1295.8	TW
OFAT7	0.9	2700	2.1	4.5	937.7	TW
	0.9	2700	2.1	4.5	1351.6	PO
	0.9	2700	2.1	4.5	1058.0	TW

Table F - Fatigue data from flat hook condition.

Load Level (%)	Lmax (N)	Lmin (N)	∆L (N)	∆L/2 (N)	R	Cycles	Fracture type
50	4382	438	3944	1972	0.1	2538	TW
50	4382	438	3944	1972	0.1	2729	TW
50	4382	438	3944	1972	0.1	1994	TW
25	2191	219	1972	986	0.1	51950	EB
25	2191	219	1972	986	0.1	58888	EB
25	2191	219	1972	986	0.1	52169	EB
15	1314	131	1183	591.5	0.1	485927	EB
15	1314	131	1183	591.5	0.1	385428	EB
15	1314	131	1183	591.5	0.1	393360	EB
10	876	88	788	394	0.1	1465194	EB
8.75	767	77	690	345	0.1	3780482	EB

7.5	657	66	591	295.5	0.1	5000000	NF
7.5	657	66	591	295.5	0.1	5000000	NF
7.5	657	66	591	295.5	0.1	5000000	NF

Table G - Fatigue data from hook pointing down condition.

Load Level (%)	Lmax (N)	Lmin (N)	ΔL (N)	ΔL/2 (N)	R	Cycles	Fracture type
50	4382	438	3944	1972	0.1	2134	PO1
50	4382	438	3944	1972	0.1	3872	PO1
50	4382	438	3944	1972	0.1	2247	PO1
25	2191	219	1972	986	0.1	47490	EB
25	2191	219	1972	986	0.1	43622	EB
25	2191	219	1972	986	0.1	52368	EB
15	1314	131	1183	591.5	0.1	447506	EB
15	1314	131	1183	591.5	0.1	364022	EB
15	1314	131	1183	591.5	0.1	394482	EB
12.5	1095	110	985	492.5	0.1	970063	EB
12.5	1095	110	985	492.5	0.1	773502	EB
12.5	1095	110	985	492.5	0.1	847190	EB
10	876	88	788	394	0.1	1961552	EB
10	876	88	788	394	0.1	2575689	EB
10	876	88	788	394	0.1	5000000	NF
8.75	767	77	690	345	0.1	2339762	EB
7.5	657	66	591	295.5	0.1	5000000	NF
7.5	657	66	591	295.5	0.1	5000000	NF
7.5	657	66	591	295.5	0.1	5000000	NF

Table H - Fatigue data from hook pointing up condition.

Load Level (%)	Lmax (N)	Lmin (N)	ΔL (N)	ΔL/2 (N)	R	Cycles	Fracture type
50	4382	438	3944	1972	0.1	1137	PO2
50	4382	438	3944	1972	0.1	1533	PO2
50	4382	438	3944	1972	0.1	1364	PO2
25	2191	219	1972	986	0.1	72456	EB
25	2191	219	1972	986	0.1	70722	EB
25	2191	219	1972	986	0.1	70958	EB
15	1314	131	1183	591.5	0.1	450169	EB
15	1314	131	1183	591.5	0.1	355274	EB
15	1314	131	1183	591.5	0.1	523503	EB

10	876	88	788	394	0.1	1397751	EB
8.75	767	77	690	345	0.1	3204380	EB
7.5	657	66	591	295.5	0.1	5000000	NF
7.5	657	66	591	295.5	0.1	4326285	EB
7.5	657	66	591	295.5	0.1	4591961	EB